

EXTREME WAVE IMPINGING AND OVERTOPPING

A Dissertation

by

YONG UK RYU

Submitted to the Office of Graduate Studies of
Texas A&M University
in partial fulfillment of the requirements for the degree of

DOCTOR OF PHILOSOPHY

August 2006

Major Subject: Civil Engineering

EXTREME WAVE IMPINGING AND OVERTOPPING

A Dissertation

by

YONG UK RYU

Submitted to the Office of Graduate Studies of
Texas A&M University
in partial fulfillment of the requirements for the degree of

DOCTOR OF PHILOSOPHY

Approved by:

Chair of Committee, Kuang-An Chang

Committee Members, Billy Edge

Richard Mercier

Achim Stössel

Head of Department, David V. Rosowsky

August 2006

Major Subject: Civil Engineering

ABSTRACT

Extreme Wave Impinging and Overtopping.

(August 2006)

Yong Uk Ryu, B.S., Chonnam National University;

M.S., Texas A&M University

Chair of Advisory Committee: Dr. Kuang-An Chang

This investigates the velocity fields of a plunging breaking wave impinging on a structure through measurements in a two-dimensional wave tank. As the wave breaks and overtops the structure, so-called green water is generated. The flow becomes multi-phased and chaotic as a highly aerated region is formed in the flow in the vicinity of the structure while water runs up onto the structure. In this study, particle image velocimetry (PIV) was employed to measure the velocity field of the water dominant region. For measurements of an aerated region that cannot be measured by PIV, a new measurement method called bubble image velocimetry (BIV) was developed. The principle and setup of the BIV method were introduced and validated. Mean and turbulence properties were obtained through ensemble averaging repeated tests measured by both methods. The dominant and maximum velocity of the breaking wave and associated green water are discussed for the three distinct phases of the impingement-runup-overtopping sequence. The distribution of the green water velocity along the top of the structure has a nonlinear profile and the maximum velocity occurs near the front of the fast moving water. Using the measured data and applying dimensional analysis, a similarity profile for the green

water flow on top of the structure was obtained, and a prediction equation was formulated. The dam breaking solution used for the green water prediction was examined with determining initial water depth based on the experiment conditions. Comparison between measurements, the prediction equation, and the dam breaking flow was made. The prediction equation and the dam break flow with appropriate initial water depth may be used to predict the green water velocity caused by extreme waves in a hurricane. To demonstrate the aeration of the breaking wave and overtopping water, void fraction was also investigated. There is strong aeration in the region of overtopping water front generated by a plunging breaker. Void fraction of overtopping water was measured using a fiber optic reflectometer (FOR). The measured velocity and void fraction were also used to estimate flow rate and water volume of overtopping water.

ACKNOWLEDGMENTS

I would like to express my sincere gratitude to my advisor, Dr. Kuang-An Chang, for his continuous support, guidance, advice, and encouragement during the time I have worked with him.

I would like to thank Dr. Billy L. Edge for his encouragement, advice and concern. I also would like to thank Dr. Richard Mercier for his valuable advice and help during my research. Special thanks are extended to Dr. Achim Stössel for serving as a member of my committee and his advice. I wish to thank the other professors of the Coastal and Ocean Engineering Division in the Civil Engineering Department. I am also thankful to Mr. John Reed for his advice about the experiments and help. Thanks to Prof. Chang Lin at National Chung Tsing University for allowing me to use the results of his research in this dissertation.

I wish to thank my parents and sister and brother-in-law for their love, trust and support from overseas. I would like to express special thanks to my colleagues, Kwang-Hyo Jung, Ho-Joon Lim for their help and friendship. I also would like to thank all my friends in the department for their friendship through the years.

TABLE OF CONTENTS

| CHAPTER | Page |
|---|------|
| I INTRODUCTION | 1 |
| 1.1 Background of interactions of extreme waves and structures | 1 |
| 1.2 Background of air-water flow measurements | 4 |
| 1.3 Objective and scope of the present study | 5 |
| II EXPERIMENTAL SETUP AND TECHNIQUES | 7 |
| 2.1 Experiment setup and conditions | 7 |
| 2.2 Particle image velocimetry technique | 12 |
| 2.3 Bubble image velocimetry technique | 15 |
| 2.4 Fiber optic reflectometer technique | 15 |
| III BUBBLE IMAGE VELOCIMETRY (BIV): AIR-WATER FLOW MEASUREMENT | 19 |
| 3.1 Introduction | 19 |
| 3.2 Principle of BIV | 21 |
| 3.3 Experimental setup | 25 |
| 3.3.1 Setup of PIV system | 25 |
| 3.3.2 Setup of BIV system | 26 |
| 3.4 Process of BIV | 27 |
| 3.5 Validation of BIV | 31 |
| 3.6 Application of BIV measurement for flow fields | 40 |
| 3.7 Conclusion | 44 |
| IV BREAKING WAVE IMPINGING AND OVERTOPPING: MEASUREMENT AND PREDICTION | 45 |
| 4.1 Introduction | 45 |
| 4.2 Experimental setup and techniques | 51 |
| 4.2.1 Wave tank and model structure | 51 |
| 4.2.2 PIV technique | 51 |
| 4.2.3 BIV technique | 52 |
| 4.3 Mean flow field by PIV | 53 |
| 4.4 Mean flow field by BIV: short deck and extended deck | 57 |
| 4.5 Turbulence intensity | 67 |
| 4.6 Vertical run-up | 72 |
| 4.7 Green water velocity distribution and dimensional analysis: cross-sectional velocity | 80 |

| CHAPTER | Page |
|---|------------|
| 4.8 Depth averaged velocity of green water | 88 |
| 4.9 Extreme wave and green water in hurricane | 91 |
| 4.10 Conclusion | 93 |
| V APPLICATION OF DAM-BREAK FLOW FOR GREEN WATER PREDICTION | 95 |
| 5.1 Introduction | 95 |
| 5.2 Vertical distribution of horizontal velocity | 97 |
| 5.3 Dam-break model for green water prediction | 102 |
| 5.4 Determination of initial water depth | 103 |
| 5.5 Comparison of dam-break flow and green water flow | 104 |
| 5.6 Conclusion | 114 |
| VI VOID FRACTION OF OVERTOPPING WATER | 115 |
| 4.1 Introduction | 115 |
| 4.2 Experimental setup and technique | 116 |
| 4.3 Void fraction and time history | 119 |
| 4.4 Vertical distribution of void fraction along the deck | 129 |
| 4.5 Dimensional analysis | 137 |
| 4.6 Flow rate and overtopping water volume | 139 |
| 4.7 Conclusion | 142 |
| VII SUMMARY AND RECOMMENDATIONS FOR FUTURE STUDY | 144 |
| 7.1 Summary | 144 |
| 7.2 Recommendations for future study | 148 |
| REFERENCES | 149 |
| VITA | 156 |

LIST OF FIGURES

| FIGURE | Page |
|--|------|
| 2.1 Sketch of wave tank..... | 8 |
| 2.2 Model structure and fields of view (FOVs)..... | 10 |
| 2.3 Wave elevations measured at (a) 5.1 m ($x = -16.6$ m), and (b) 21.7 m ($x = 0.0$ m) from the wavemaker..... | 12 |
| 2.4 Sketch of PIV technique..... | 13 |
| 2.5 Image recording technique: Double-frame/single-pulsed method. The black dots represent the exposed images of a particle by a pulsing laser light at time t_1 and t_2 | 14 |
| 2.6 FOR apparatus..... | 17 |
| 2.7 FOR signal of a bubble: (a) low sampling rate (10 kHz), (b) high sampling rate (10 MHz)..... | 18 |
| 3.1 BIV apparatus..... | 24 |
| 3.2 PIV measurement of plunging breaking wave impinging on structure..... | 28 |
| 3.3 Sample BIV image of wave impinging on structure..... | 30 |
| 3.4 Close-up of the bubbly flow in Fig. 3.3 and associated velocity vectors obtained using BIV. (a) raw image, (b) inverted image, (c) instantaneous velocity field..... | 30 |
| 3.5 Schematic of the BIV validation experiment..... | 32 |
| 3.6 Bubble plume measurement by BIV: (a) mean velocity field, (b) cross- sectional vertical velocity at $z_b = 45$ cm..... | 33 |

| FIGURE | Page |
|---|------|
| 3.7 Comparison of velocities measured using BIV and FOR. o, BIV instantaneous velocities; ×, FOR instantaneous velocities; solid line, BIV mean velocity; dotted line, FOR mean velocity..... | 34 |
| 3.8 Scheme of superimposition of clear and blurry images using two sets of clear and blurry images: (a) clear images, (b) blurry images, (c) upside down blurry images, (d) superimposed clear and blurry images, and (e) superimposed clear and flipped blurry images..... | 36 |
| 3.9 Image sets and instantaneous flow fields corresponding to Fig. 3.8..... | 37 |
| 3.10 Velocity distribution along the centerline of the bubble plume obtained from: clear images (o), blurry images (+), vertically flipped blurry images (×), superimposed clear and blurry images (□), superimposed clear and flipped blurry images (◇)..... | 39 |
| 3.11 Flow field of plunging breaking wave impinging on structure measured by BIV method..... | 41 |
| 3.12 BIV measurement of breaking wave after impingement (courtesy of H.-J. Lim).. | 42 |
| 3.13 Instantaneous flow pattern and velocity field of aerated hydraulic jump measured by BIV (courtesy of Prof. Lin, National Chung Tsing University)..... | 43 |
| 4.1 Green water incident at the side of the Selkirk Settler. Photograph by Captain G. A. Ianiev (courtesy of Prof. Douglas Faulkner) from Schoenberg and Rainey (2002)..... | 46 |
| 4.2 PIV measurement of breaking waves impinging on structure: (i-iv), spilling breaker with a small air pocket; (a-d), plunging breaker with a large air pocket. The time separation between the consecutive frames is 25 ms..... | 55 |
| 4.3 Maximum cross-sectional horizontal velocities measured by PIV along the x axis. “◇”, t_0 ; “∇”, $t_0 + 0.025$ s; “+”, $t_0 + 0.050$ s; “△”, $t_0 + 0.075$ s..... | 57 |

| FIGURE | Page |
|---|------|
| 4.4 Mean velocity fields obtained by BIV at $t =$ (a) -0.07 s, (b) -0.035 s, (c) 0.000 s, (d) 0.035 s, (e) 0.070 s, (f) 0.105 s, (g) 0.140 s, (h) 0.175 s, (i) 0.210 s, (j) 0.245 s, (k) 0.280 s, and (l) 0.315 s..... | 59 |
| 4.5 Cross-sectional velocity on the model with the short deck at time at $t =$ 0.035 s (o) 0.105 s (\diamond), 0.175 s (\square), 0.245 s (\cdot), and 0.315 s (\times)..... | 62 |
| 4.6 BIV measured mean velocity fields of plunging breaking wave impinging on structure with the extended deck at $t =$ (a) -0.04 s, (b) - 0.02 s, (c) 0.00 s, (d) 0.02 s, (e) 0.04 s, (f) 0.06 s, (g) 0.08 s, (h) 0.10 s, (i) 0.12 s, (j) 0.14 s, (k) 0.16 s, (l) 0.18 s, (m) 0.20 s, (n) 0.22 s, (o) 0.24 s, and (p) 0.26 s..... | 64 |
| 4.7 Turbulent intensity I (m/s) corresponding to Fig. 4.7 at $t =$ (a) -0.04 s, (b) -0.02 s, (c) 0.00 s, (d) 0.02 s, (e) 0.04 s, (f) 0.06 s, (g) 0.08 s, (h) 0.10 s, (i) 0.12 s, (j) 0.14 s, (k) 0.16 s, (l) 0.18 s, (m) 0.20 s, (n) 0.22 s, (o) 0.24 s, and (p) 0.26 s..... | 68 |
| 4.8 Maximum turbulence intensity and relative turbulence level. \square -: I_{max} (m/s), \bullet -: $I_{max} / \langle UU + WW \rangle_{max}^{1/2}$ | 72 |
| 4.9 Measured maximum vertical velocities and locations along the z axis at $t =$ (a) -0.04 s, (b) -0.02 s, (c) 0.00 s, (d) 0.02 s, (e) 0.04 s, (f) 0.06 s, (g) 0.08 s, (h) 0.10 s, and (i) 0.12s..... | 74 |
| 4.10 Maximum vertical velocities along the z axis near impingement at $t =$ (a) -0.058 s, (b) -0.056 s, (c) -0.054 s, (d) -0.052 s, (e) -0.050 s, (f) -0.048 s, (g) -0.046 s, (h)- 0.044 s, (i) -0.042 s, and (j) -0.040 s..... | 78 |
| 4.11 Cross-sectional velocity at time; $t =$ 0.02 s (\bullet), 0.06 s (\blacklozenge), 0.10 s (\blacksquare), 0.14 s (\times), 0.18 s (\blacktriangledown), 0.22 s (\blacktriangle), and 0.26 s ($*$)..... | 80 |

| FIGURE | Page |
|---|------|
| 4.12 Similarity profile obtained using the non-dimensional velocity, time and distance at $t = 0.02(\bullet)$, $0.03(\blacklozenge)$, $0.04(\blacksquare)$, $0.05(*)$, $0.06(\blackstar)$, $0.07(\blackstar)$, $0.08(\blacktriangledown)$, $0.09(\times)$, $0.10(+)$, $0.11(\bullet)$, $0.12(\blacktriangle)$, $0.13(\blacktriangleleft)$, $0.14(*)$, and $0.15(\blacktriangleright)$ s. Solid line is the fitting curve using least square regression..... | 84 |
| 4.13 Maximum horizontal velocity U_M against time t . Solid line: linear fit using Data at $t \leq 0.15$ s | 85 |
| 4.14 Locations of wave front and maximum horizontal velocity (U_M). “o”, wave front; “ \blacklozenge ”, U_M ; solid line, curve fitting of wave front..... | 86 |
| 4.15 Distribution of depth averaged green water velocity at $t = 0.02$ s (\bullet), 0.04 s (\blacklozenge), 0.06 s (\times), 0.08 s ($+$), 0.10 s (\blacksquare), 0.12 s ($*$), and 0.14 s (\blacktriangledown)..... | 89 |
| 4.16 Maximum depth averaged velocity at a time..... | 90 |
| 4.17 Similarity profile of non-dimensional depth average velocity from $t = 0.02$ to 0.15 s. Solid line is a fitting curve..... | 91 |
| 4.18 Dominant velocities at different phases..... | 94 |
| 5.1 Distributions of horizontal velocity of green water at $t =$ (a) 0.00 s, (b) 0.02 s, (c) 0.04 s, (d) 0.06 s, (e) 0.08 s, (f) 0.10 s, (g) 0.12 s, (h) 0.14 s, (i) 0.16 s, (j) 0.18 s, (k) 0.20 s, (l) 0.22 s, (m) 0.24 s, (n) 0.26 s, and (o) 0.28 s..... | 98 |
| 5.2 Comparisons of cross-sectional horizontal velocity U_c along the deck among the experimental data (velocity measured using BIV and shown in Fig. 4.12), the prediction equation (Eq. (4.8)), and the analytical solution of dam break flow (Ritter’s solution in Eq. (5.3)) at $t =$ (a) 0.02 s, (b) 0.04 s, (c) 0.06 s, (d) 0.08 s, (e) 0.10 s, (f) 0.12 s, (g) 0.14 s, (h) 0.16 s, (i) 0.18 s, (j) 0.20 s, (k) 0.22 s, and (l) 0.24 s. Solid line, Ritter’s solution with $h_0 = 6.0$ cm (obtained using Eq. (5.4)); dashed line, Ritter’s solution with $h_0 = 14.0$ cm (obtained using Eq. (5.7)); dashed-dotted line, prediction equation..... | 105 |

| FIGURE | Page |
|--|------|
| 5.3 Time history of horizontal velocity of green water at $x =$ (a) 5.7 mm, (b) 40.8 mm, (c) 75.9 mm, (d) 111.1 mm, (e) 146.2 mm, (f) 181.3 mm, (g) 216.5 mm, (h) 251.6 mm, (i) 286.7 mm, (j) 321.8 mm, (k) 356.9 mm, and (l) 378.0 mm. “o”, BIV measurements; solid line, Ritter’s solution with $h_0 = 6.0$ cm (obtained using Eq. (5.4)); dashed line, Ritter’s solution with $h_0 = 14.0$ cm (obtained using Eq. (5.7)); dashed-dotted line, prediction model (Eq. (4.8)). | 111 |
| 6.1 (a) FOR probe; (b) setup of FOR in the experiments. | 118 |
| 6.2 Measurement points using FOR. | 119 |
| 6.3 Time series of the void fractions at $x =$ (a) 0 mm, (b) 50 mm, (c) 100 mm, (d) 150 mm, (e) 200 mm, (f) 250 mm, and (g) 300 mm. Measurements at 10 vertical locations were measured and shown in the legend in (a) and (b). | 121 |
| 6.4 Time series of the void fractions at vertical locations. $z_d =$ (a) 10 mm, (b) 20 mm, (c) 30 mm, (d) 40 mm, (e) 50 mm, (f) 60 mm, (g) 70 mm, (h) 80 mm, (i) 90 mm, and (j) 100 mm. | 124 |
| 6.5 Vertical distributions of void fractions and horizontal velocities of green water along the deck at $t =$ (a) 0.00 s, (b) 0.02 s, (c) 0.04 s, (d) 0.06 s, (e) 0.08 s, (f) 0.10 s, (g) 0.12 s, (h) 0.14 s, (i) 0.16 s, (j) 0.18 s, (k) 0.20 s, (l) 0.22 s, (m) 0.24 s, (n) 0.26 s, and (o) 0.28 s. -o-, void fraction; -x-, velocity. | 130 |
| 6.6 Vertical distribution of time averaged void fraction. | 135 |
| 6.7 Distribution of time averaged void fraction in three regions. (a) $x = 0$ mm (\circ) and 50 mm (\diamond); (b) $x = 100$ mm (\square) and 150 mm (∇); (c) $x = 200$ mm (\circ), 250 mm (Δ), and 300 (\triangleleft) mm. | 136 |
| 6.8 Distribution of depth averaged void fraction; $t = 0.02$ s (\bullet), 0.05 s (\times), 0.08 s (\diamond), 0.11 s ($+$), 0.14 s (\blacksquare), 0.17 s (\ast) 0.20 s (\blacktriangledown), 0.23 s (\star), 0.26 s (\blacktriangle), 0.29 s (\star), and 0.32 s (\blacktriangleleft). | 137 |

| FIGURE | Page |
|--|------|
| 6.9 Similarity plot of void fraction and regression. Filled symbols, data taken from $t = 0.02$ s to 0.24 s; solid line, regression Eq. (6.3)..... | 138 |
| 6.10 Comparison of void fraction between measurements and regression equation at $t = 0.02$ s (\circ), 0.08 s (\times), 0.14 s (\diamond), 0.20 s (+), 0.26 s (\square), 0.29 s (\ast). Dotted lines, regression equation..... | 139 |
| 6.11 Flow rate at downstream locations..... | 140 |
| 6.12 Comparison of water volume. Temporal integration of flow rate, \circ ; direct measurement using collection tank, thick dashed line (mean) and thin solid line (standard deviation)..... | 142 |

LIST OF TABLES

| TABLE | Page |
|-------------------------------------|------|
| 2.1 FOVs and setup conditions | 10 |

CHAPTER I

INTRODUCTION

1.1 Background of interactions of extreme waves and structures

Extreme waves such as breaking waves or waves with large wave heights on structures are of primary concern in the area of coastal and ocean engineering. Tremendous pressures and loads by the impact of extreme waves on sea walls or offshore structures have been considered important subjects for both points of view of local fracture and stability of the structures. Moreover, since extreme waves have large wave heights and momentum, the waves approaching to or impacting a structure generate overtopping water. Besides the impact issue of extreme waves, associated overtopping water is also of importance in the design of structures. In coastal areas, overtopping water over maritime structures matters mainly because of inundating water over structures. Although most maritime structures are supposed to protect properties behind the structures, overtopping water affects flows such as waves inside a harbor or causes damage to road and erosion on ground behind a seawall. Meanwhile, offshore engineers have had interest in the behavior of overtopping water on top of a structure. Because offshore structures have facilities and equipment installed on the deck, it is important to know flow pattern of overtopping water on the deck for proper design. Since overtopping loads occur when an incoming wave significantly exceeds the free

This dissertation follows the style and format of *Journal of Waterway, Port, Coastal and Ocean Engineering*.

board and water rushes onto the deck, thus, any increase in the frequency of occurrence and severity of hurricanes implies that structures in the ocean are at higher risk of exposure to extreme waves and green water loads.

Typically large breaking waves are used to represent the extreme waves. Since breaking waves impinging on a structure and the overtopping water on the structure generate significant loads on the structure, it is of importance to understand the breaking waves and associated overtopping water. The impinging patterns of breaking waves have been classified into four categories by many researchers (e.g., Oumeraci et al., 1993, 1995; Hattori et al., 1994; Hull and Müller, 2002). Their studies found that the impact loads are strongly influenced by the shape of breaking wave as it impinges on a wall. Although there are many studies investigating the relation between wave impacts on a vertical wall and the breaking shape, the flow pattern after the impingement and overtopping green water have not been well understood. On the other hand, there have been other numerical approaches focusing on the forces of the waves on structures and simple flow field kinematics using the potential flow theory for the “engineering use” for prediction and the physical insight of the flow field either based on the Reynolds averaged Navier-Stokes equations (RANS) or large eddy simulation (LES) (e.g., Lin and Liu, 1998a, 1998b; Watanabe and Saeki, 1999; Christensen and Deigaard, 2001)

Green water, which is overtopping water on the deck, has been investigated experimentally and numerically. Through an experimental model test, Buchner (1995a) suggested the relation between green water occurrence and loading and ocean conditions and the resemblance of green water to a dam break flow and later investigated

the effect of green water with different bow shapes (Buchner, 1996). Hamoudi and Varyani (1998) performed experiments with various wave heights to investigate the probability of green water occurrence by examining the number of deck wetness. They found that there is no direct relation between the velocity of waves and the velocity of green water on the deck. Among the numerical studies, Maruo and Song (1994) studied the effect of the wave steepness on green water in the bow region using a boundary element method while Nielsen and Mayer (2004) used a Navier-Stokes solver with a volume-of-fluid scheme to model the green water loads on a vessel. Because it has been reported that a dam breaking flow is similar to green water, there have been many studies that applied the dam break theory to green water studies taking advantage of simplification of the problem (Fekken et al., 1999; Shoenberg and Rainey, 2002; Yilmaz et al., 2003). The dam break flow used for the green water prediction is a class problem that has been investigated by numerous researchers. Among solutions for various cases, an analytical simplest solution for a dry frictionless flat bed, Ritter's solution, (Lauber and Hager, 1997; Vischer and Hager, 1998; Zoppou and Roberts, 2003) has been used for green water predictions (Buchner, 1995a, b; Shoenberg and Rainey, 2002). Even though many green water studies use the dam break flow for velocity estimation, validation on the relation between the dam break flow and green water flow has not yet carefully proved.

Very few non-intrusive quantitative velocity measurements of breaking waves impinging on structures exist even if the measurement on breaking waves itself has been of great interest to numerous researchers. For the velocity measurements of breaking

waves, various measurement techniques, including laser Doppler velocimetry (LDV) and particle image velocimetry (PIV), have been employed (e.g., Greated and Emarat, 2000; Ting and Kirby, 1994, 1995; Perlin et al., 1996). Even if PIV can be perhaps considered the most robust and state-of-the-art technique, as a wave breaks and entrains air bubbles, the technique is then restricted to a fluid dominant region outside an aerated region.

1.2 Background of air-water flow measurements

Breaking waves representing extreme waves and associated green water have highly aerated flow fields by wave breaking and subsequent air entrapment. Thus, in order to investigate a full field by breaking waves, measurements of velocities at air-water flow fields are necessary.

Among studies using a non-intrusive method, despite some works that measured an aerated region (Jansen, 1986; Govender et al. 2002), most measurements of breaking wave flow fields and generated turbulence were succeeded outside aerated regions (Chang and Liu, 1999, 2000; Melville et al., 2002). Even though the measurements of the successful studies are promising, no detailed description on the technique itself was provided. The measurement of gas-liquid flows has been investigated in various areas which have typically lower bubble void fraction and smaller bubble size than a breaking wave. Even though the PIV technique and tracking each bubble in the recorded images taken by applying the “shadowgraphy” method have been used to measure bubble velocity (Hassan et al., 1998; Nishino et al., 2000; Lindken and Merzkirch, 2001), the

methods may not be applicable because the breaking wave usually generates high aeration.

1.3 Objective and scope of the present study

The objective of the present study is to investigate the velocity field of breaking waves as extreme waves in the vicinity of a structure. Since the velocity field is highly aerated and non-intrusive instruments capable of measuring the flow field of air-water mixture does not exist, a new technique, called bubble image velocimetry (BIV) is developed for experimental approach in measuring aerated regions. The velocity fields of the breaking waves and overtopping green water measured with both PIV and BIV are presented. Through the measurement data and dimensional analysis, a prediction equation for green water velocity is established and compared with a solution of the dam break flow used for the prediction and the measurements. In addition, the aeration of the fields is examined by the study of void fractions to complete the study of flow field by the breaking waves.

In this dissertation, the experimental methods used through the present study are presented in Chapter II. In Chapter III, a new measurement method, BIV, is described in terms of the principal and setup of the method. The BIV method is validated by comparing a simple experiment with fiber optic reflectometer (FOR) that is capable of measuring velocity of bubbles. Velocity fields measured using BIV are demonstrated for the flow fields of a plunging breaker, overtopping water due to extreme wave, and a hydraulic jump.

In Chapter IV, breaking waves and subsequent overtopping green water in the vicinity of a structure are studied by analyzing measurements obtained by PIV and BIV. Velocity fields are demonstrated by detailed velocity measurements in front of a structure by PIV and on top of it by the newly developed BIV method. Mean and turbulence properties obtained by phase average with the measured data are discussed. A prediction equation of green water velocity distribution based on the measured velocity fields using dimensional analysis is developed and tested. With the measurements, possible kinematics of extreme wave and overtopping water during a hurricane was predicted. In Chapter V, a traditionally widely used dam break solution was examined with determining initial water depth. Comparisons among the measured green water velocity, the prediction model, and the traditionally widely used linear dam break solution are also made. Vertical profiles of horizontal velocities are presented to know the behavior of the overtopping water on top of the structure. In Chapter VI, void fraction measured by FOR is presented in order to clarify aeration of the flow. The void fraction is examined by phase averaging and time averaging. Depth average is employed to have a representing property of a cross-section. Flow rate and wave volume of the overtopping water are estimated using the void fraction and corresponding velocity. Finally, Chapter VII summarizes the present study and suggests recommendations for future works.

CHAPTER II

EXPERIMENTAL SETUP AND TECHNIQUES

2.1 Experiment setup and conditions

The experiments were performed in a glass-walled wave tank located at the Department of Civil Engineering, Texas A&M University. The wave tank is 36 m long, 0.9 m wide and 1.5 m high. The water depth was kept constant at $d = 0.80$ m throughout the experiments. The wavemaker is of dry back flap type. The flap is driven by a synchronous servo-motor controlled by a computer and hydrostatically balanced using an automatic near constant force and a pneumatic control system. A 1:5.5 sloping beach with a layer of horsehair is at the other end of the tank to absorb the wave energy and reduce reflection. A double-wired resistant-type wave gauge was used to measure the free surface elevation. The signal from the wave gauge was converted to voltage and sent to a data acquisition board housed in a computer.

A rectangular model structure was located 21.7 m away from the wavemaker. The structure has a height of 0.31 m, a length of 0.15 m without an extended deck and 0.37 m with a 0.22 m long extended deck, and spans the width of the wave tank. The draft of the model structure is 0.20 m and so the freeboard is 0.11 m. The dimensions of the model structure were chosen to be representative, in a two-dimensional sense, of a tension-leg platform (TLP) with a scale ratio of 1:168 while the extension deck is to mimic the deck of a FPSO. The model structure was mounted on aluminum frames that were rigidly fixed to the bottom of the tank and suspended from the top of the tank

in order to minimize vibration induced by a breaking wave impinging on the model.

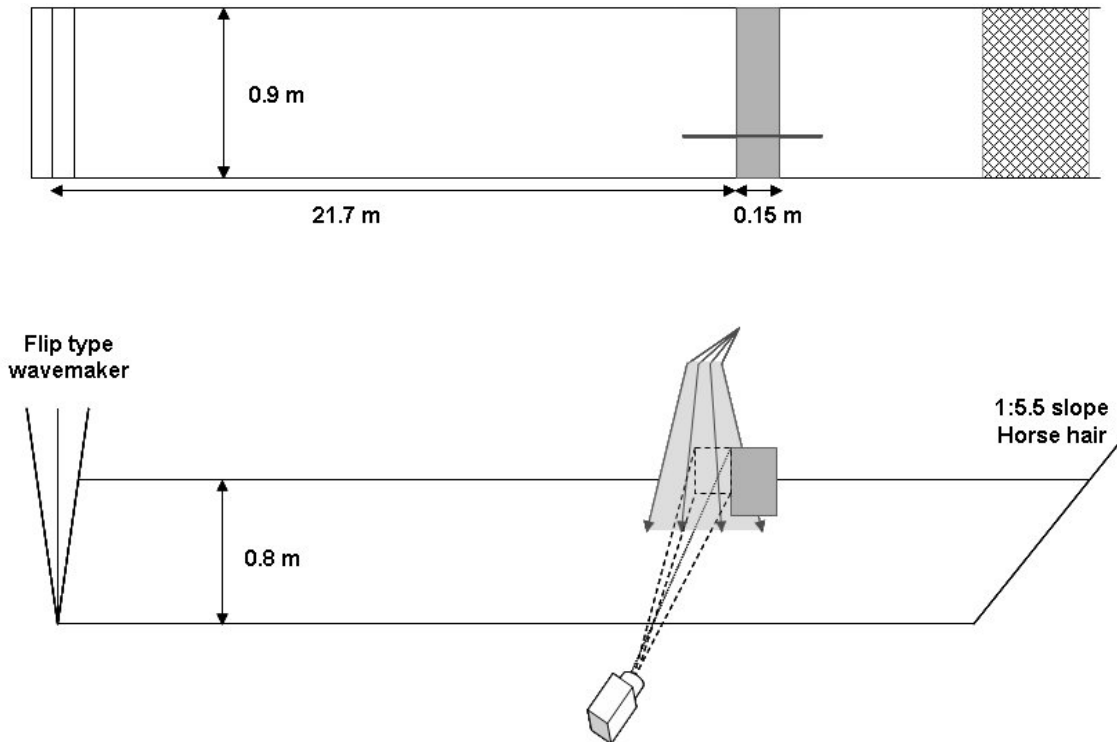


Fig. 2.1. Sketch of wave tank.

The velocity field was measured using two non-intrusive image-based techniques: particle image velocimetry (PIV) and bubble image velocimetry (BIV). The PIV technique was used for the measurement of the single-phase region while the BIV technique which was developed in the present study was for the aerated region and splashing green water. The details of the both methods will be discussed in next sub chapters. Fig. 2.1 shows the side view and top view of the wave flume and the

model structure with the PIV system.

The detailed sketch of the model structure is shown in Fig. 2.2 with the coordinate system and the fields of view (FOV) used for the PIV and BIV measurements. Note that the origin $(x, z) = (0, 0)$ is at the intersection of the structure front wall and the still water level. Velocity measurements were performed with three different FOVs. First, the PIV technique was used to measure the flow field in front of the model structure in FOV 1. The focus of FOV 1 was on the instant when the breaking wave impinges on the structure. FOV 2 was for the BIV measurements in the vicinity of the structure that covers the front and the top of the structure. Since the waves have broken in the region, the flow is bubbly and the region is aerated. In order to investigate the green water effect without the end-of-the-deck problem (water falls off the short deck immediately after rushing up to the deck), a longer deck of 0.22 m in length was later added to the original model structure. This is for the easier analysis (so the length of the deck is no longer a variable), and for later comparisons with the dam-breaking model widely used for green water prediction. With the extended deck, the total length of the deck of the structure becomes 0.37 m. Even though the deck length is more than doubled, it is still much shorter than the wavelength of the breaking waves used in the study. To measure the flow fields on the extended deck using BIV, the large FOV 3 was used. The setup condition is shown in table 2.1. All the control and data acquisition signals for operating the wavemaker, triggering the PIV and BIV systems, and measuring the free surface profiles were synchronized.

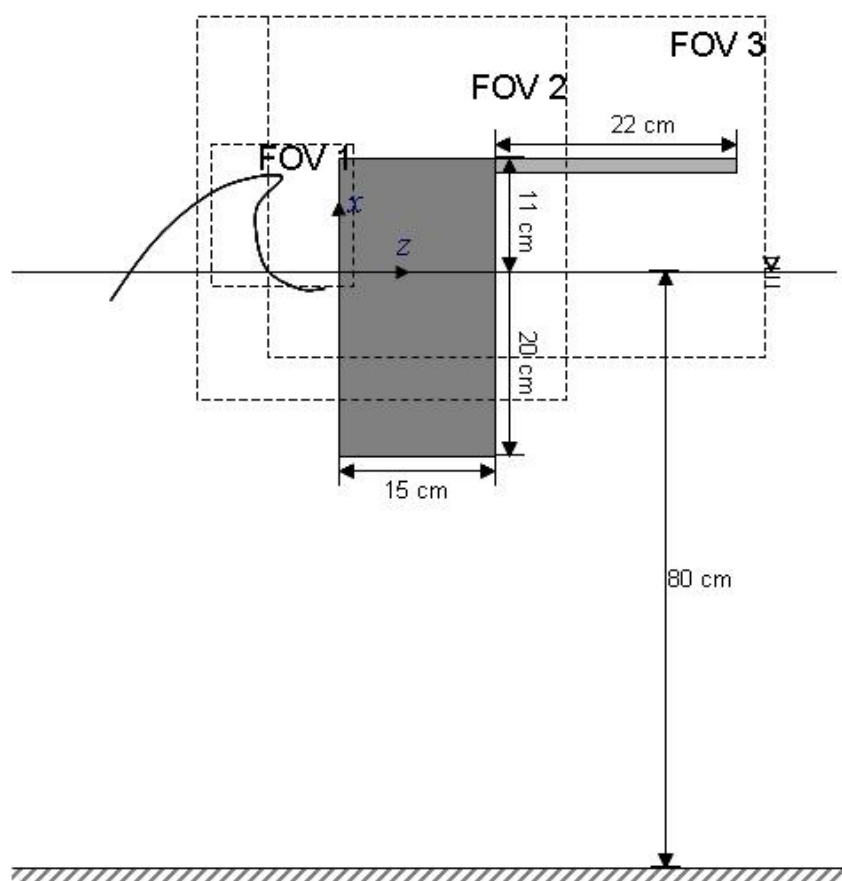


Fig. 2.2. Model structure and fields of view (FOVs)

Table 2.1. FOVs and setup conditions

| FOV | Condition | Method | FOV size (mm ²) | Spatial resolution (mm ²) |
|-------|--------------------------|--------|-----------------------------|---------------------------------------|
| FOV 1 | Model | PIV | 150×120 | 1.8×1.8 |
| FOV 2 | Model | BIV | 378×378 | 5.5×5.5 |
| FOV 3 | Model with extended deck | BIV | 410×275 | 7.0×7.0 |

In this study, the breaking wave impinging on the model structure is a plunging breaker generated using a wave focusing method. The wave train consists of waves with a range of frequencies from 0.7 Hz to 1.3 Hz at a constant water depth of $d = 80$ cm. The plunging breaker breaks at a desired location right in front of the model structure. The generated breaking wave is highly repeatable and the tests were repeated 20 times to obtain the mean and turbulence quantities from ensemble averaging. The free surface elevation was measured using two wave gauges located at 5.1 m and 21.7 m from the wavemaker (i.e., $x = -16.6$ m and $x = 0.0$ m in front of the structure) to measure the incoming waves and the water elevation at the frontal edge of the structure, respectively. The measured wave profiles are shown in Fig. 2.3. In Fig. 2.3 (a), peak frequency obtained by the spectral analysis, wavelength corresponding to the peak frequency, wave height, and peak frequency related phase speed (C) of the breaking wave in the deep water are 0.77 Hz, 2.54 m, 17.1 cm, and 1.95 m/s, respectively. The wave period was defined as from the peak frequency which was obtained by the spectral analysis of the wave amplitude. The phase velocity is a peak frequency related phase velocity and was calculated using the dispersion relationship of the linear wave theory from the peak frequency. Because of the wave superposition, Fig. 2.3 (b) shows that the height of the wave became about 24 cm right at the frontal edge of the structure.

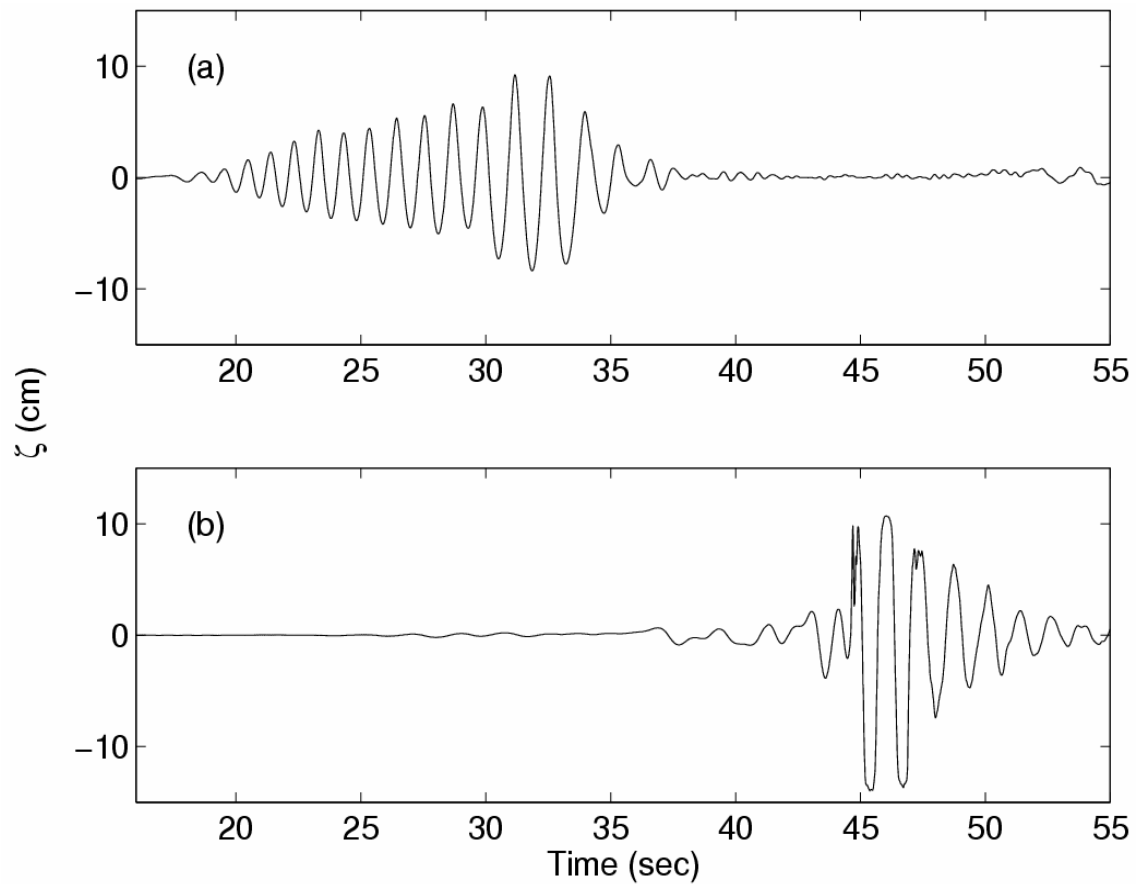


Fig. 2.3. Wave elevations measured at (a) 5.1 m ($x = -16.6$ m), and (b) 21.7 m ($x = 0.0$ m) from the wavemaker.

2.2 Particle image velocimetry technique

The PIV technique in the present study was first used to measure the velocity field. The PIV technique is a non-intrusive, indirect, and whole field method. The tested flow had no intrusive probes in it but was seeded with neutrally buoyant tiny particles as tracers.

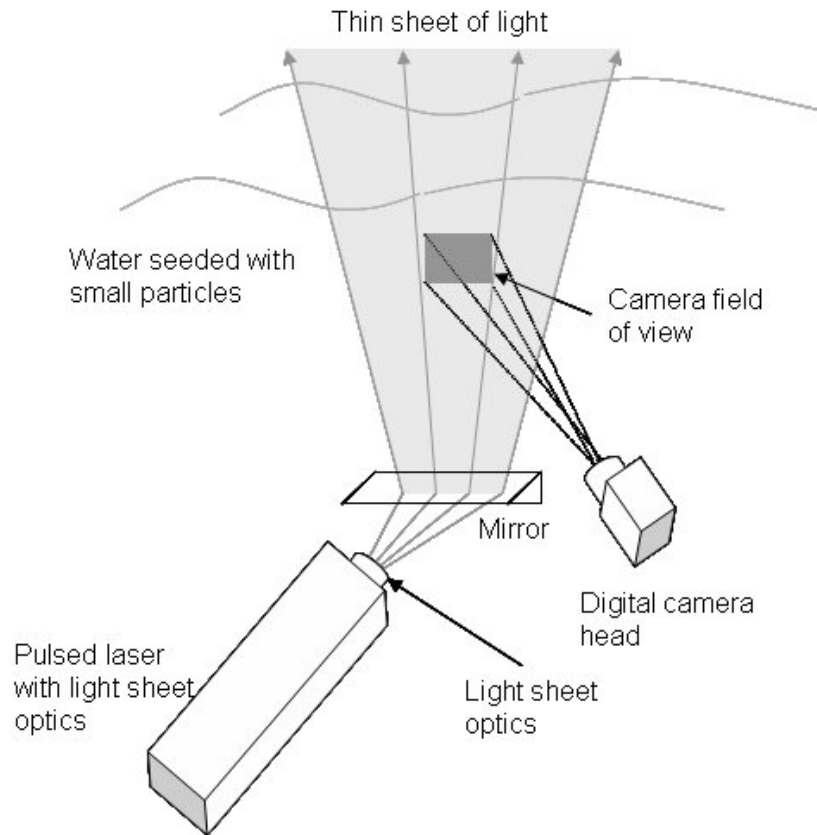


Fig. 2.4. Sketch of PIV technique.

The sketch of the PIV technique is shown in Fig. 2.4. The basic principle of the PIV technique is that the tiny seeding particles in the fluid are illuminated by a thin sheet of pulsing laser light twice within a short time interval with images captured using a camera. As a result, there is one image for each particle on a single frame and two consecutive frames are used to trace the particle motion. Fig. 2.5 shows the double-frame/single-pulsed method for the image recording.

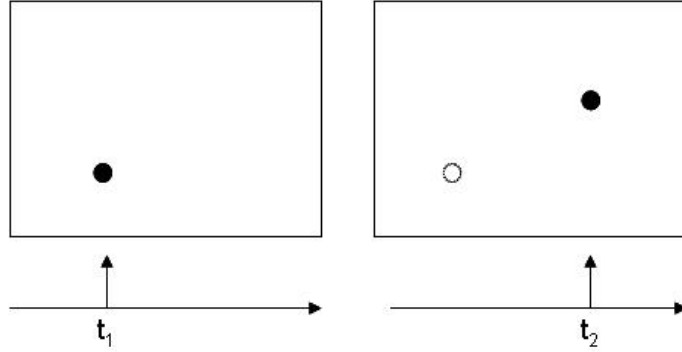


Fig. 2.5. Image recording technique: Double-frame/single-pulsed method. The black dots represent the exposed images of a particle by a pulsing laser light at time t_1 and t_2 .

After the images containing particles are acquired, cross correlation is employed to obtain the displacement of particles over the short time separation, Δt . Small areas (called subwindow or interrogation area) in the images are used to find the particle displacement in the area. The cross correlation can be written as:

$$R(\mathbf{s}) = \int_{\text{subwindow}} f(\mathbf{x})g(\mathbf{x}+\mathbf{s})d\mathbf{x} \quad (2.1)$$

in which R , the 2D function, is the result from the correlation, f and g are the 2D mathematical representation of the two images (call an image pair), and \mathbf{x} and \mathbf{s} are the position vector and the displacement vector, respectively. With the finding the maximum value in the 2D function R and curve fitting technique for subpixel accuracy, the *mean* particle displacement $(\Delta x, \Delta z)$ over the small area that occurs at the highest correlation can be obtained. The velocity can be subsequently calculated as $u = \Delta x / \Delta t$, $w = \Delta z / \Delta t$. In general, Fast Fourier Transform (FFT) is used to speed up the processing for correlation computation. The details of the PIV techniques can be found

in Raffel et al. (2001).

2.3 Bubble image velocimetry technique

In the present study, the bubble image velocimetry (BIV) technique was developed and used to obtain the velocity field in the highly aerated region. The technique correlates the bubble images and “texture” in the images created by the bubbles and the air-water interfaces. The BIV method uses the shadowgraphy technique for image recording and the cross-correlation for displacement calculation of bubble structures in recorded images. Since images are obtained by the shadowgraphy technique and bubble structures in the images play a role as tracers, neither laser light sheet nor seeding particles are needed for the BIV technique unlike the traditional PIV technique. The BIV method will be introduced in detail in Chapter III.

2.4 Fiber optic reflectometer technique

The fiber optic reflectometer (FOR) technique introduced by Chang et al. (2003) was employed to measure void fraction of green water and velocities of bubbles for validation of the BIV method. The technique is capable of measuring the velocity as well as the fraction ratio of all three phases of the flow at a given point if the liquid or gas flow is seeded with small neutrally buoyant particles.

The FOR technique is based on the coherent mixing of scattered signal with Fresnel reflection signal from the tip of an optical fiber. An optical signal derived from a diode laser driven by a constant current is launched into a single-mode optical fiber

and transmitted, through a fiber coupler, to the signal fiber inserted into a test fluid. The diode laser used is a multi-longitudinal mode device that has a low coherence length of about 200 μm . The coherently mixed signal propagates back to the signal fiber through the fiber coupler, and the returned signal from the signal fiber is detected by a detector. The signal is subsequently acquired by a data acquisition board installed on a computer. By analyzing the signal, the velocity in the direction parallel to the fiber and void fraction ratio of each phase can be obtained. For a fraction ratio study, a measured quantity of interest is reflected optical power due to Fresnel reflection off a fiber–fluid interface at the fiber tip while a measured quantity of interest for a velocity measurement is coherent beat signal between Fresnel reflection off the fiber–fluid interface and scattered signal off gas bubbles, solid particles, or liquid droplets. The setup of the FOR system shown in Chang et al. (2003) is sketched in Fig. 2.6.

For the fraction ratio study, measured quantities are the reflected optical power due to Fresnel reflections off the fiber–fluid interface at the fiber tip. Due to the change in refractive index, the phase of the flow at the measurement point (the fiber tip) can be easily identified, allowing the measurement of the fraction ratio of each phase. For the velocity measurement, the measured quantity is the coherent beat signal between the Fresnel reflection off the fiber–fluid interface and the scattered signal off the gas bubbles, solid particles, or liquid droplets and the period of oscillation of the signal is used to calculate velocity. Fig. 2.7 shows a raw bubble signal with a low sampling rate (10 kHz) and the rising front of high sampling rate (10 MHz). Since the only intrusion to the fluid is the tiny fiber probe (a dimension of 125 μm in diameter), the disturbance to

most fluid flows is negligible, therefore, the technique is nearly non-intrusive. The details of the FOR method can be found in Chang et al. (2003).

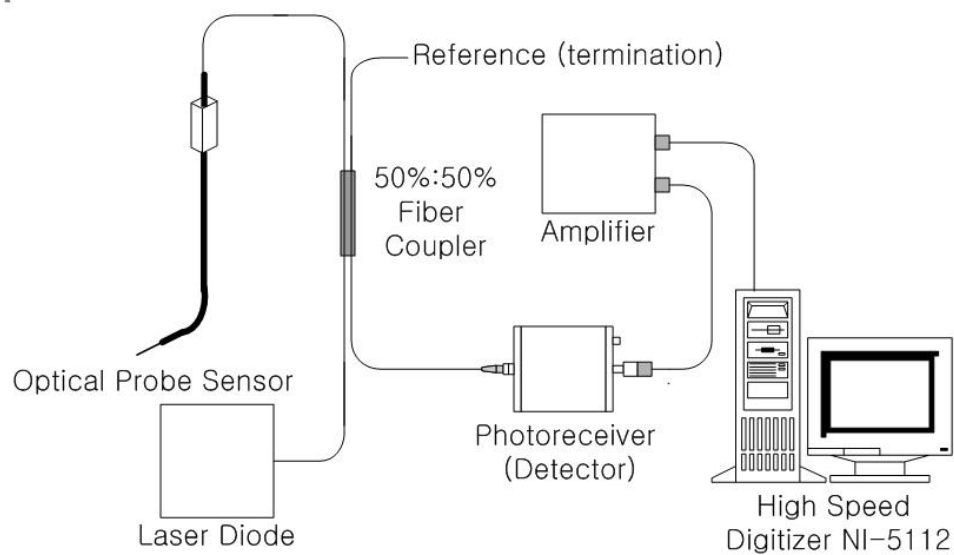


Fig. 2.6. FOR apparatus.

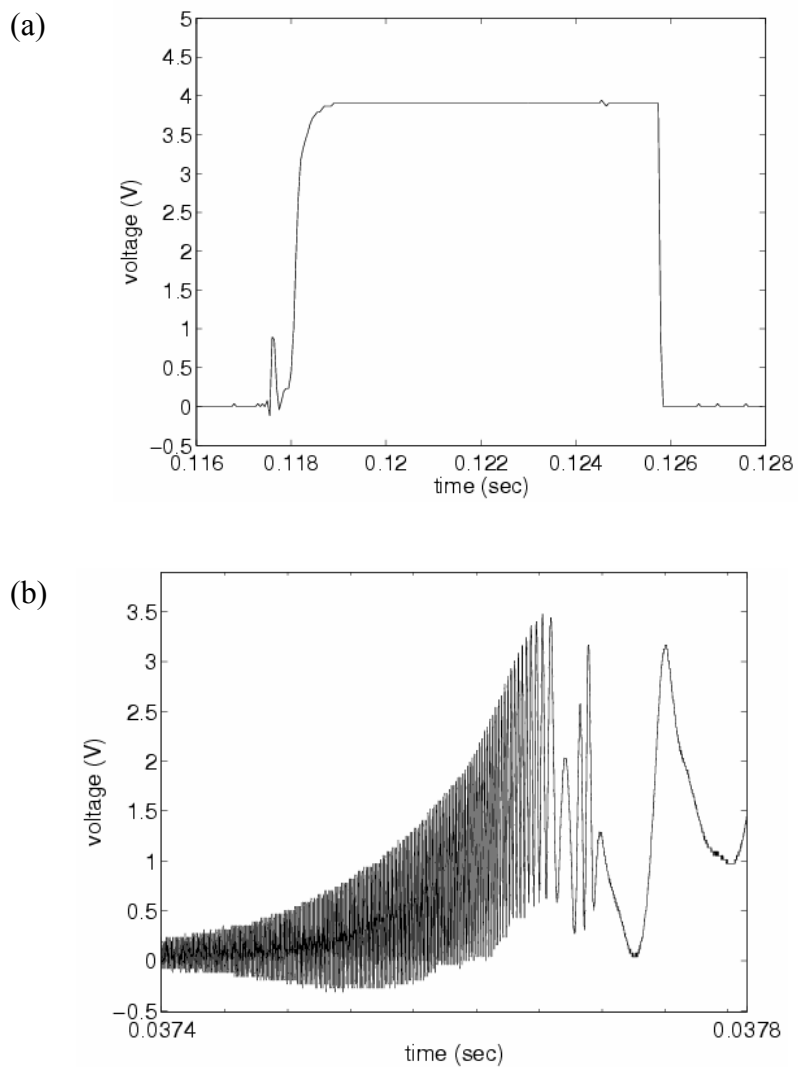


Fig. 2.7. FOR signal of a bubble: (a) low sampling rate (10 kHz), (b) high sampling rate (10 MHz).

CHAPTER III

BUBBLE IMAGE VELOCIMETRY (BIV): AIR-WATER FLOW MEASUREMENT

3.1 Introduction

When breaking waves, especially, plunging breakers impinge on free water surface or a structure, air bubbles are entrained and air-water mixture flows occur. Recently, flow field by breaking waves have been measured mostly by optic based measurements such as LDV, PIV because of their strength in measurements other than old methods. Despite the increase of the strength of the methods, whole flow fields of breaking waves have not been measured due to difficulty in measurements of aerated region. There have been studies measuring velocities using double tips of probes capable of detecting bubbles. Even if the methods can measure void fraction and estimated velocities of bubbles using the correlation between two probes, because the methods use intrusive probes, they can influence flow fields. Moreover, methods with probes are point measurements so that an instantaneous flow field cannot be obtained.

There have been a few studies measuring velocity field of air-water flow by breaking waves. In early works, Jansen (1986) measured particle trajectories in the aerated region of breaking waves using fluorescent tracers and ultraviolet light, but the measurements suffered from poor spatial resolution. More comprehensive measurements were obtained by Govender et al. (2002), who used a technique similar to PIV based on the digital image acquisition and cross-correlation algorithms with the use

of a laser light sheet to illuminate the aerated region. Bubble structures in the images were used for correlation between consecutive images for velocity determination. Even though the saturation of laser light sheet by aerated region is of importance in the measurement technique, no detailed description to deal with the point was provided. Non-intrusive measurement techniques, including laser Doppler velocimetry (LDV) and particle image velocimetry (PIV), have been employed for the velocity measurements of the wave breaking process in both surf zone and deep water (e.g., Greated and Emarat, 2000; Ting and Kirby, 1994, 1995; Perlin et al., 1996; Chang and Liu, 1999, 2000; Melville et al., 2002). Despite some success on the measurements of the breaking wave flow field and generated turbulence outside the aerated region (Chang and Liu, 1999, 2000; Melville et al., 2002), the advances in the understanding of the flow structure inside the highly aerated region have rarely been reported.

In addition to the direct measurement of bubbly flow under breaking waves, the measurement of gas-liquid flows has been investigated in various areas. Typically the bubble void fraction and the bubble size are much lower and smaller than that in a breaking wave. For such flows the scattering of laser light due to bubbles is much less and thus more controllable. The PIV technique have been successfully used to measure bubble velocity by correlating bubbles or tracking each bubble in the recorded images that were taken by applying the “shadowgraphy” method (Hassan et al., 1998; Nishino et al., 2000; Lindken and Merzkirch, 2001). The method uses a light source behind the bubbles therefore the bubbles appear in the images as their shadows. Again, the density and size of bubbles have to be within a certain limit so the shadows are separated

and identifiable. Typically the two methods above are used in low void fraction flow with small bubbles, and may not be applicable in breaking wave measurements.

This present study presents a new non-intrusive velocity measurement method, named bubble image velocimetry (BIV). The BIV technique is similar to PIV except the first one directly correlates the bubble images and does not require a laser light sheet for illumination. The principle of the BIV method is described in detail and the explanation about the setup of the method is followed. The velocity field measured by using both the traditional PIV technique with a laser light sheet and the new BIV method is compared and discussed. The BIV method will be validated through comparing with the result using fiber optic reflectometer (FOR) (Chang et al., 2003) from bubble plume experiments. In addition, the effect by blurry images on velocity calculation will be tested by the image superimposition of blurry and clear images. The sequential velocity field of a breaking wave and consequent overtopping water in the vicinity of a structure is demonstrated. As other applications, velocity field of a plunging breaker, a sloshing flow is presented.

3.2 Principle of BIV

The BIV technique was used to obtain the velocity field in an aerated region. The technique correlates the bubble images and “texture” in the images created by the bubbles and the air-water interfaces. No small seeding particles used in the traditional PIV technique are needed. The idea of the BIV method came from combining the shadowgraphy technique that illuminates the fluid from behind to reveal the flow pattern,

and the PIV technique that correlates the consecutive images to determine the velocity. Since the velocity is calculated through cross-correlating the images obtained by the shadowgraphy technique with the bubble structure in the images as tracers, the BIV technique requires only two light projectors to illuminate the air bubbles in the aerated region. Unlike the traditional PIV technique, no laser light sheet is needed.

The illumination of the flow is the modification of the traditional shadowgraphy method with lights being placed at both sides of the wave tank. One light placed at the back side of the tank was used to illuminate the flow from behind (the high speed camera was located at the other side). A thin sheet of translucent white plastic glass was attached on the back-side glass wall of the tank. This way the light bulb will illuminate the flow more uniformly without the use of a costly large high intensity light emitting diode (LED) plate typically used in the shadowgraphy technique. However, for the region with a high concentration of bubbles the captured images will be filled with shadows and appear to be all dark in that region. The images do not provide the needed differences in intensity to reveal the bubble structure or bubble “texture” for later correlation. To resolve this problem, a light was placed on the other side of tank (at the same side with the high-speed camera but with an angle) in order to produce the desired intensity differences in the images. The light illuminating behind the tank was located with an angle of 0° (normal to the FOV) while the other at the other side had an angle of about 60° . Subsequently, images captured using the modified shadowgraphy technique were inverted so the high intensity (bright) represents the bubbles. The flow velocity was calculated by cross-correlating the flow texture from the inverted consecutive

images.

Since the BIV technique does not use a light sheet to illuminate a specific plane of interest like the traditional PIV method, it is necessary to know where the measured bubbles are in the cross-tank direction (i.e. the y direction). The problem is solved by limiting the depth of field (DOF) in the experiment, achieved by carefully setting up the camera. The DOF is defined as a distance within which objects captured by the camera are well focused and appear to be sharp. The camera focal point and the DOF can be considered as the light sheet plane and light sheet thickness, respectively, in the PIV technique. This way the FOV of the captured images can be defined. Assuming that a lens focuses on a point at a distance L from the forward nodal point of the lens (which is sufficiently close to the distance between the lens front and the point), the DOF can be calculated using the formulae below. Following Ray (2002), the formulae for the nearest limit, R , and the farthest limit, S , of the DOF can be expressed as $R = Lf^2 / (f^2 + NLC)$ and $S = Lf^2 / (f^2 - NLC)$, in which f is the focal length of the camera focal lens, C the value for the circle of confusion that depends on the property of the camera, and N the f-number of the camera aperture. The DOF is $D = S - R$.

Objects located in front of and behind the DOF will appear to be blurring without a clear texture in the captured image and therefore have little effect on the later correlation process for velocity determination. On the other hand, objects located within the DOF will be sharp in the image with a featured pattern due to the flow. This means that the obtained velocity from cross-correlating the captured images is indeed mainly contributed from the image of fluid within the DOF. The uncertainty on the

position of the images in the cross tank direction is therefore one-half of the thickness of the DOF from the center of the DOF. As a result, the error due to the thickness of DOF in the obtained velocity can be estimated approximately as $\varepsilon = D/2L$. If the depth of view D is thin and the distance between the camera and the focal plane L is long, the error can be minimized. Fig. 3.1 shows the setup of BIV.

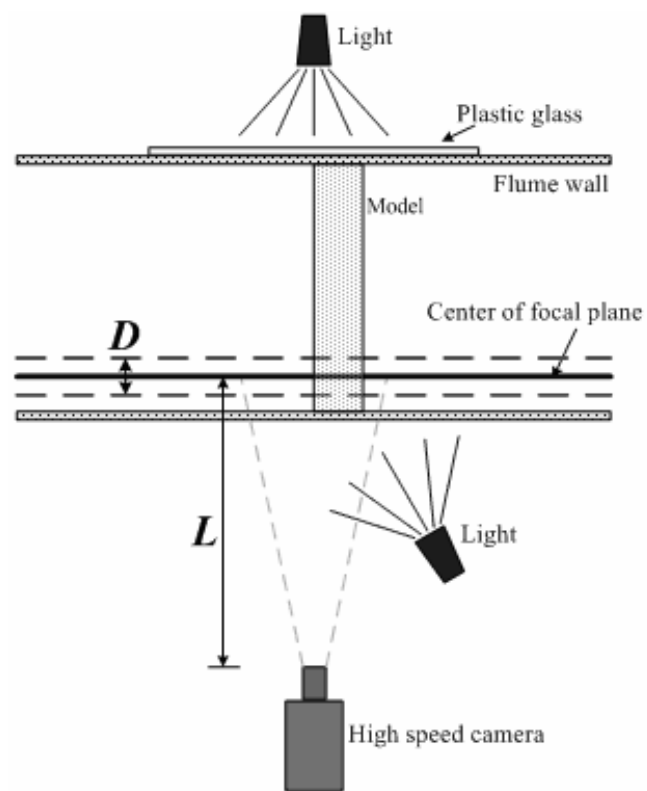


Fig. 3.1. BIV apparatus.

3.3 Experimental setup

The experiments were performed in a glass-walled wave tank 36 m long, 0.9 m wide and 1.5 m high (See Chapter II). The wavemaker is of dry-back flap type installed at one end of the wave tank and a 1:5.5 sloping beach with a layer of horsehair is at the other end of the tank to absorb the wave energy and reduce reflection. A rectangular model structure with a length of 0.15 m, a height of 0.31 m and a width the same as that of the tank was installed in the wave tank. A plunging breaking wave was generated using a wave focusing method. See Chapter II for details. A velocity field was measured by both the PIV and BIV methods. All the control signals, including the signals controlling the wavemaker and triggering the PIV/BIV system, and measured data were synchronized.

3.3.1 Setup of PIV system

The PIV technique in the present study was first used to measure the velocity field near the front wall of the model structure. The light source of the PIV system is a dual-head frequency-doubled Spectra-Physics Nd:YAG laser that has a 532 nm wavelength, 400 mJ maximum output energy, 6 ns pulse duration, and 10 Hz repetition rate for each head. A set of optics consisting of cylindrical and spherical lenses was used to generate the light sheet. The image recording device is a CCD camera from LaVision Inc. that has an 8 frames per second (fps) maximum framing rate, a resolution of 1024×1280 pixels, and a 12-bit dynamic range. The seeding particles, Vestosint

2157, have a mean diameter of $56 \mu\text{m}$ and a specific weight of 1.02. The FOV for the PIV measurements is from $x = -14 \text{ cm}$ and to $x = 0.7 \text{ cm}$ and from $z = 1 \text{ cm}$ to $z = 13 \text{ cm}$ with $x = 0$ being the leading edge of the structure and $z = 0$ being the calm water level as shown in Fig. 2.2 (denoted as FOV1). The time interval between two successive laser pulses is 0.6 ms. The frame rate was set at 7.27 Hz during all experiments. The measurements were repeated 11 times with a small delay between each so continuous velocity fields with a time interval of 0.025 sec were obtained. The interrogation area for velocity determination was 32×32 pixels with a 50 % overlap. A commercial software from LaVision was used for the velocity computation.

3.3.2 Setup of BIV system

In the BIV system, in the present study, regular 600 W light bulbs with reflecting mounts were used for a light source to illuminate the flow. The images were captured by a Phantom high speed camera mounted with a Nikon 105 mm micro focal lens. The camera has a resolution of 512×512 pixels, an 8-bit dynamic range, and a maximum framing rate of 1000 fps. The aperture of the camera was set with the f-number (N) equal to 1.8. In the present study, $L = 4.0 \text{ m}$, $f = 105 \text{ mm}$, $N = 1.8$, and $C = 0.03 \text{ mm}$. The calculated R is about 3.92 m and S is about 4.07 m therefore the corresponding DOF in the present study is $D = 0.15 \text{ m}$. The error due to the thickness of the DOF in this study is estimated as 2%.

The FOV for the BIV measurement is $37.8 \text{ cm} \times 37.8 \text{ cm}$ and centered at $x = 5.2 \text{ cm}$ and $z = -5.3 \text{ cm}$ as shown in Fig. 2.2 (denoted as FOV 2). The time interval

between the recorded images was 1.75 ms that is equal to the time separation between the consecutive frames captured by the high speed camera. The images were processed using the LaVision PIV software and the velocity field was calculated using an adaptive multi-pass algorithm with an initial interrogation window size of 32×32 pixels and a final window size of 16×16 pixels with a 50% overlap. A median filter was subsequently applied to eliminate the spurious vectors in the calculated velocity map. The mean velocity was calculated from ensemble averaging 10 instantaneous velocity fields from repeated runs with the same test condition.

3.4 Process of BIV

The velocity measurement in the vicinity of the model structure was first carried out using the PIV technique. For the spilling type of breaking waves impinging on the structure, the air pocket between the wave front face and the structure is relatively small therefore majority of the region in front the leading edge of the structure is not highly aerated and suitable for PIV. However, even for the cases with only a small air pocket, green water above the structure due to overtopping is highly aerated and not ideal for PIV. If the impinging wave is of plunging type, a large air pocket in front of the structure will form and cause severe light scattering and result in saturated and not useful images for PIV correlation. The problem continues to the green water on top of the structure. Fig. 3.2 shows the PIV measurement of the plunging breaking wave taken at FOV1 shown in Fig. 2.2. Clearly there exists a large region where no velocity vectors were obtained due to the large amount and size of air bubbles. The similar problem

was also observed in Chang and Liu (1999, 2000).

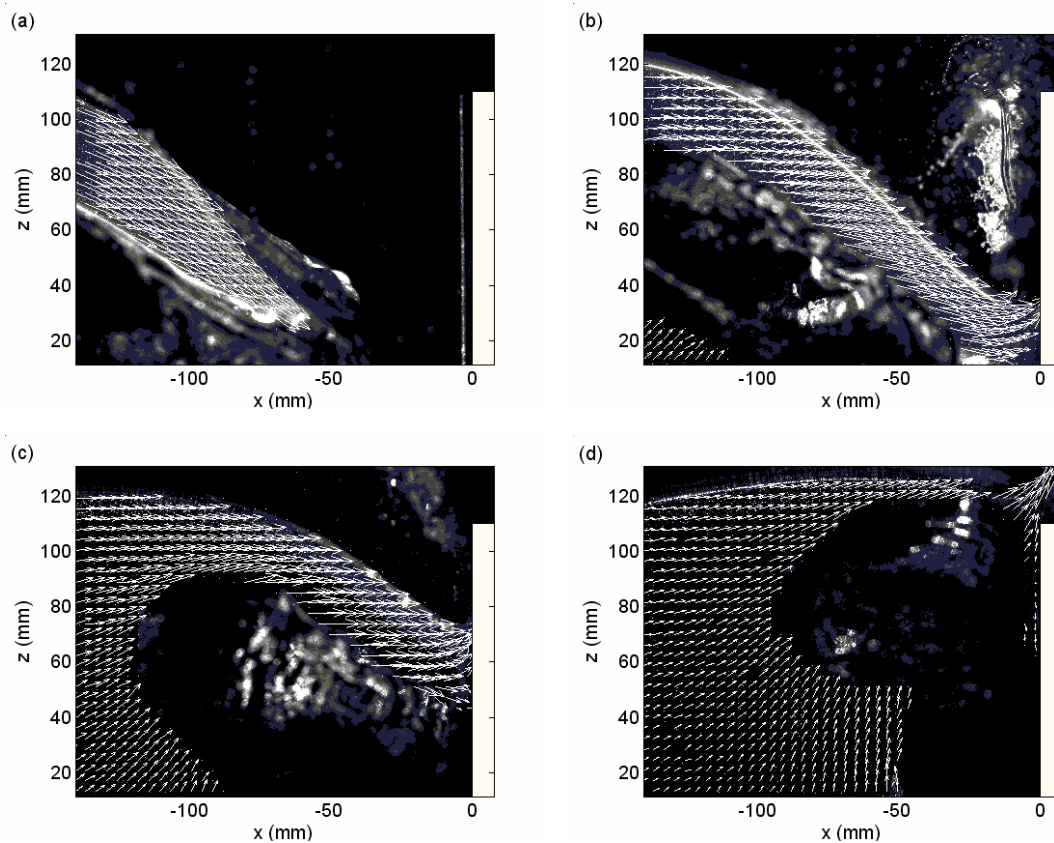


Fig. 3.2. PIV measurement of plunging breaking wave impinging on structure.

The BIV technique uses the bubbles as tracers and correlates the bubble texture in the aerated region. This means that the BIV technique works in the region where the PIV technique does not work. Fig. 3.3 shows a sample of inverted BIV images

captured for the present study. The flow pattern of the bubble in front of the structure and the splashing jet above the structure are clearly identified in the image. Displacement estimation by the image correlation is obtained from high intensity in an image. Since objects of interest in the original image (not inverted) are air bubbles in dark color, it needs to be inverted in terms of color. Fig. 3.4 (a) shows the image and texture in the aerated region that is a close-up of Fig. 3.3 (see the marked area in the figure) without image color inversion. Since the air bubbles appeared to be dark, the image was inverted, as shown in Fig. 3.4 (b), before performing correlation for velocity determination. Fig. 3.4 (c) shows the obtained BIV velocity vectors through cross-correlating the inverted images. As a result, it is shown that as long as there exist a certain amount of air bubbles or air-water interfaces that form a distinct flow pattern or texture in the images, velocities can be obtained by cross correlating the images.

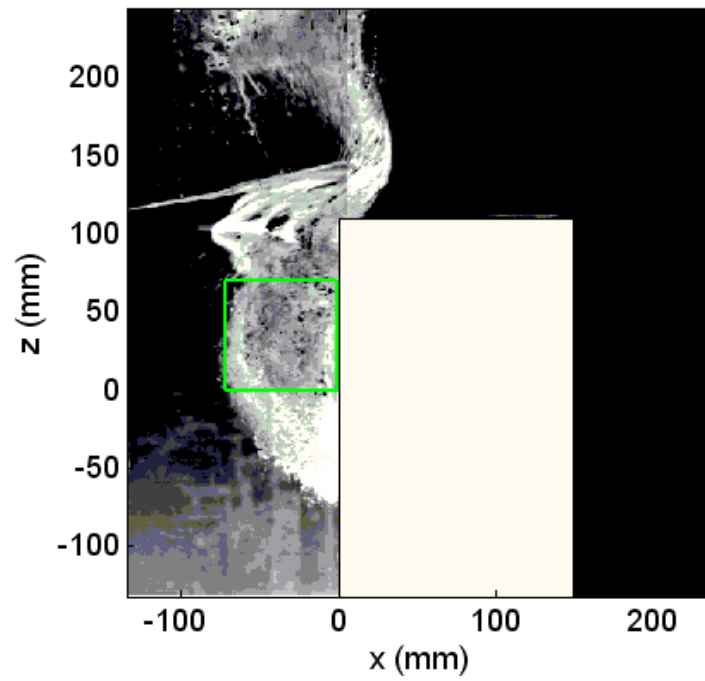


Fig. 3.3. Sample BIV image of wave impinging on structure.

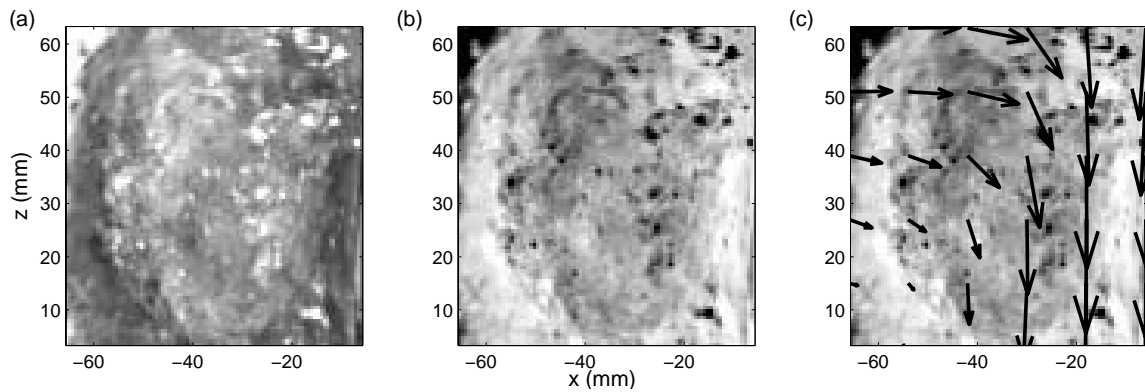


Fig. 3.4. Close-up of the bubbly flow in Fig. 3.3 and associated velocity vectors obtained using BIV: (a) raw image, (b) inverted image, (c) instantaneous velocity field.

3.5 Validation of BIV

The validation of BIV was performed in two ways: first to compare the velocity measured using the BIV technique with that measured using the fiber optic reflectometer (FOR) technique; second to check the effect of the blurry images out of the DOF in the BIV velocity measurement. A bubble plume in a water tank was used in the validation.

A two-phase quasi-steady bubbly flow in a vertical narrow tank was measured using both the BIV technique and the FOR technique. The objective of this experiment is to validate the BIV method by comparing the results obtained from these two methods. The FOR technique is capable of measuring the velocity time history of both water (seeded with small particles) and air bubbles at a given point in a multi-phase flow. Details of FOR are given by Chang et al. (2003).

The vertical narrow tank used in the validation has a length of 0.4 m, a width of 0.4 m and a height of 0.8 m. Water was filled to a depth of 0.7 m in the tank. An air diffuser generating air bubbles was located at the bottom of the tank. Bubble plume was formed in the tank with a diameter approximately 0.11 m at the measurement section. The BIV method was used to measure the velocity of the bubble plume with a FOV of 12.6 cm \times 12.6 cm. Subsequently, the FOR technique was employed to measure the velocity at $x_b = 0$ and $z_b = 45$ cm, located in the region of the BIV FOV with $x_b = 0$ and $z_b = 0$ being the center of the air diffuser. The experiment setup and is sketched in Fig. 3.5.

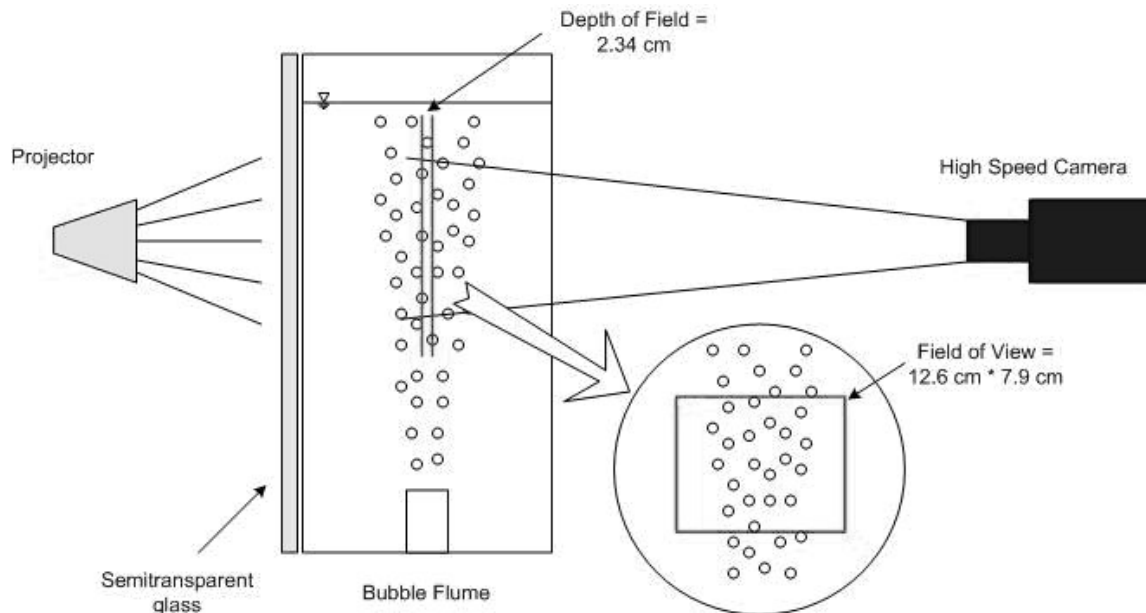
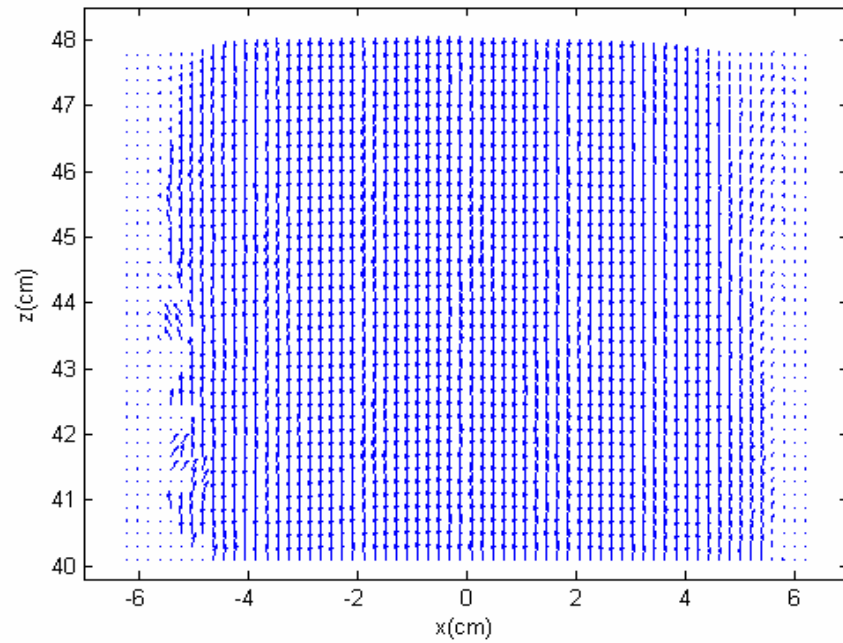
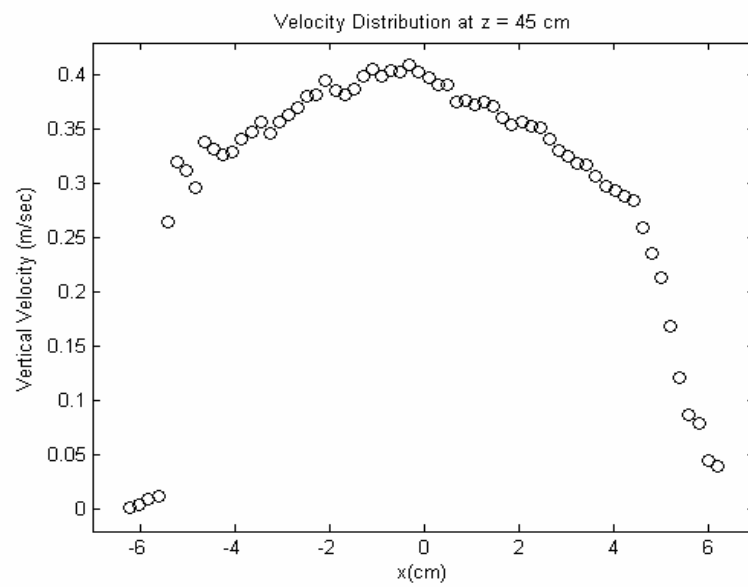


Fig. 3.5. Schematic of the BIV validation experiment.

Fig. 3.6 shows the mean velocity field of the bubble plume measured by the BIV method. The mean velocities were obtained by ensemble average using 20 instantaneous velocities. Fig. 3.6 (b) is the distribution of the cross-sectional vertical velocity at the level of $z_b = 45$ cm, the same as that of the FOR probe. The mean velocity distribution measured in the present study is not identical to the known cross sectional mean velocity profile because the number of instantaneous velocities used for averaging is not big enough. Fig. 3.7 shows the measured bubble velocities using both the BIV and FOR methods at the point where the FOR probe was located. The void fraction is 4 % with the average size of the bubble equal to 3 mm at the FOR measurement point, obtained by FOR. The mean velocities were obtained using 20 and 10 instantaneous velocities in the BIV and the FOR measurements, respectively.



(a)



(b)

Fig. 3.6. Bubble plume measurement by BIV: (a) mean velocity field, (b) cross-sectional vertical velocity at $z_b = 45 \text{ cm}$.

The comparison between the mean velocities shows very good agreement with a small discrepancy about 1% (approximately 4 mm/s). The scattering of the instantaneous velocities may be due to the turbulent nature of the flow.

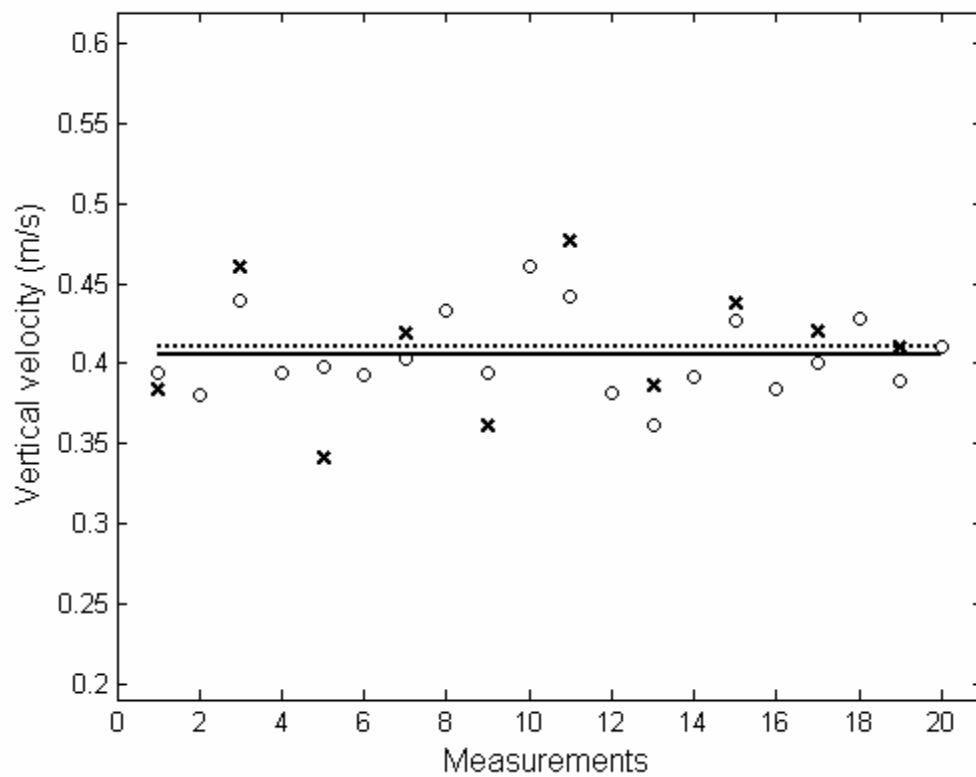


Fig. 3.7. Comparison of velocities measured using BIV and FOR. o, BIV instantaneous velocities; x, FOR instantaneous velocities; solid line, BIV mean velocity; dotted line, FOR mean velocity.

In theory the blurring images contributed from the bubbles outside the DOF are expected to have insignificant influence in the correlation for velocity determination because the intensity of the bubbles is much weaker (and spreads much wider) than that of the well-focused bubbles inside the DOF. Since the BIV measurements are in general performed in highly aerated bubbly flows, the captured images are indeed the sharp images inside the DOF superimposed with the blurry images outside the DOF. In order to investigate the blurry image effect to the BIV accuracy, the velocity obtained from the well-focused clear bubble images was compared with that obtained from artificially superimposed out-of-focus blurry bubble images. The process to examine the blurry image effect is presented in Fig. 3.8. Two sets of images were taken from similar flow fields but with different bubble velocities due to different bubble sizes. One set focused at the center of the bubble plume so the bubble images are sharp and clear while another set focused 15 cm behind the center of the plume therefore the bubble images are blurry and out of focus. Figs. 3.8 (a) and (b) represent the former and the latter set, respectively. Clear and blurry images were then artificially added in two ways. Firstly, the blurry images were added to the clear images directly shown in Fig. 3.8 (d). Secondly, the blurry images were vertically flipped (Fig. 3.8 (c)) and then added to the clear images (Fig. 3.8 (e)). Fig. 3.9 shows five sets of images corresponding to the scheme of Fig. 3.8 and the instantaneous velocity fields.

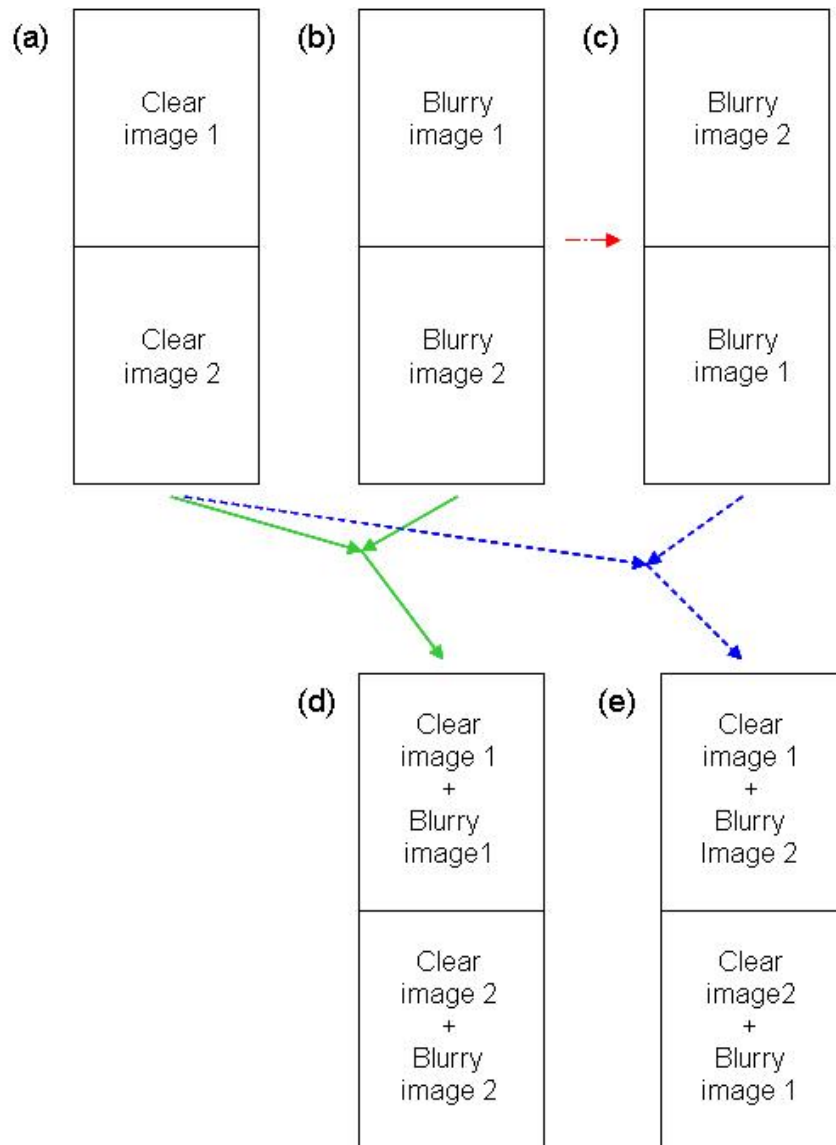


Fig. 3.8. Scheme of superimposition of clear and blurry images using two sets of clear and blurry images: (a) clear images, (b) blurry images, (c) upside down blurry images, (d) superimposed clear and blurry images, and (e) superimposed clear and flipped blurry images.

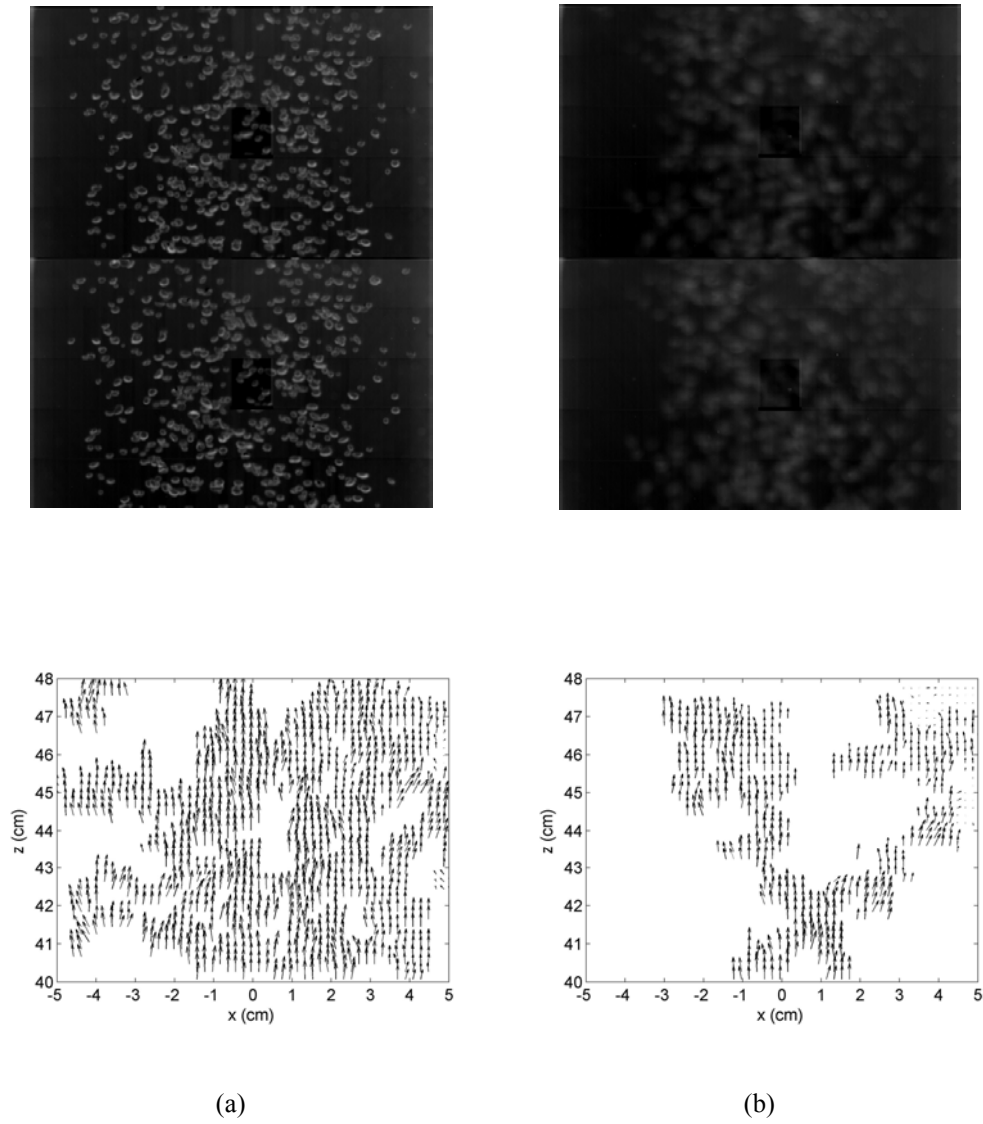
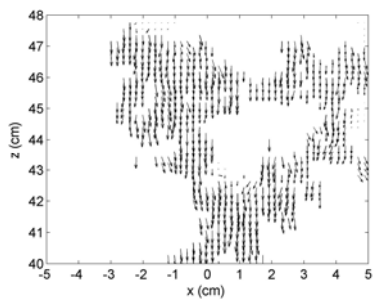
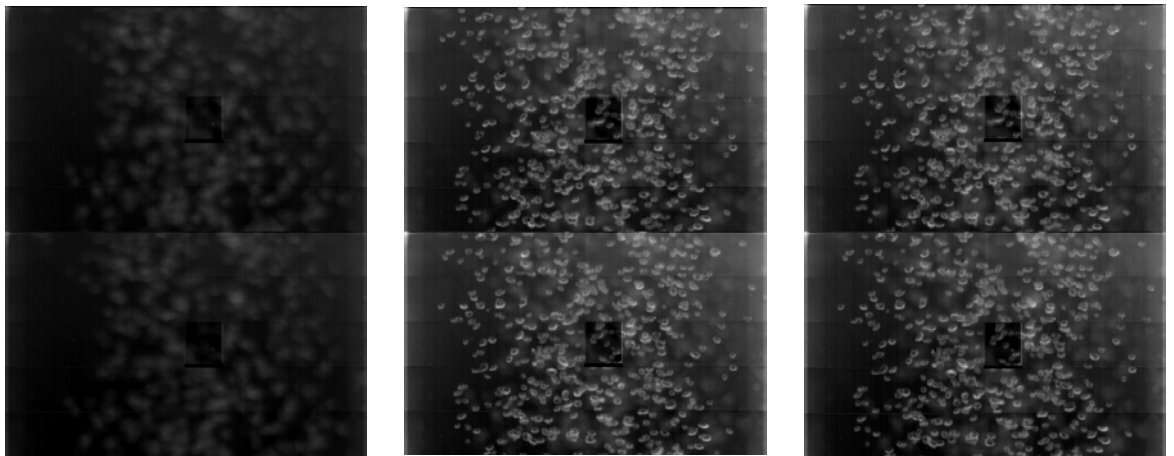
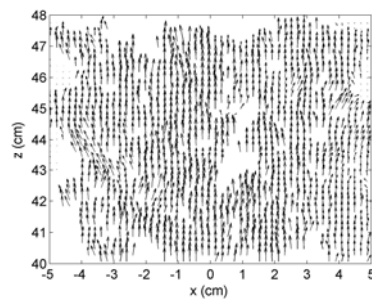


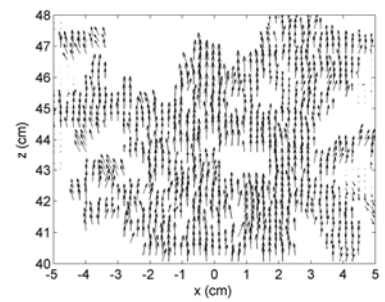
Fig. 3.9. Image sets and instantaneous flow fields corresponding to Fig. 3.8.



(c)



(d)



(e)

Fig. 3.9: (continued)

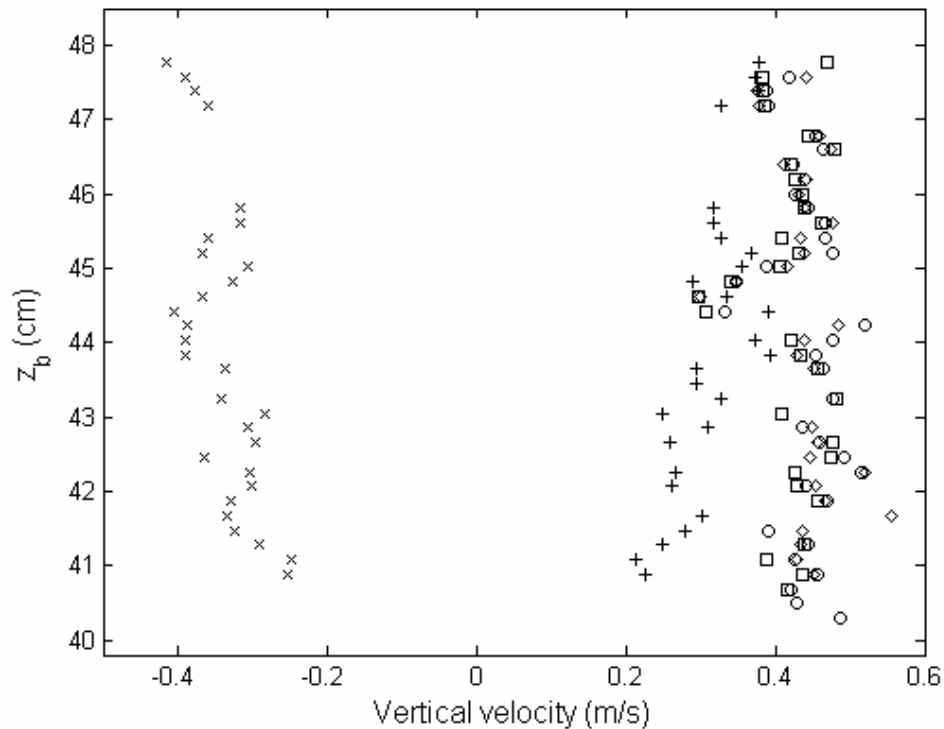


Fig. 3.10. Velocity distribution along the centerline of the bubble plume obtained from: clear images (o), blurry images (+), vertically flipped blurry images (\times), superimposed clear and blurry images (\square), superimposed clear and flipped blurry images (\diamond).

Fig. 3.10 shows the instantaneous vertical velocity distribution obtained along the centerline of the bubble plume from the clear images (Fig. 3.9 (a)), blurry images (Fig. 3.9 (b)), vertically flipped blurry images (Fig. 3.9 (c)), superposition of the clear images and blurry images (Fig. 3.9 (d)), and superposition of the clear images and the vertically flipped blurry images (Fig. 3.9 (e)). The Figure shows that both the

velocities obtained from the clear-blurry superimposed images are very close to that from the clear images. Therefore the blurry and out of focus bubble images have little effect on the accuracy of the BIV velocity measurements.

3.6 Application of BIV measurement for flow fields

Fig. 3.11 shows the velocity field of a plunging breaker impinging and overtopping in the vicinity of a structure under the same experimental condition as that in Fig. 3.2 but measured using the BIV technique. The field of view is shown in Fig. 2.2 and denoted as FOV 2. The entire sequence of velocity field during the impinging and green water processes is demonstrated in the figure. Note that the velocity field is the mean velocity obtained from ensemble averaging 10 repeated instantaneous BIV velocity measurements while the images were picked from one of 10 instantaneous image sets. In the figure, there are conspicuous patterns of the breaking wave impinging and overtopping in the vicinity of a structure as it processes. The momentum of the breaking wave is horizontal-dominant when impinging as shown in Fig. 3.11 (a). After the impingement, the vertically upward run-up occurs while a vortex structure is shown in front of the front wall (Fig. 3.11 (b)). The vertically upward run-up changes to horizontal dominant overtopping water on top of the structure and the vortex structure moves downward along the front wall. The patterns of the breaking wave process near the structure are shown clearly by the velocity fields measured by the BIV method.

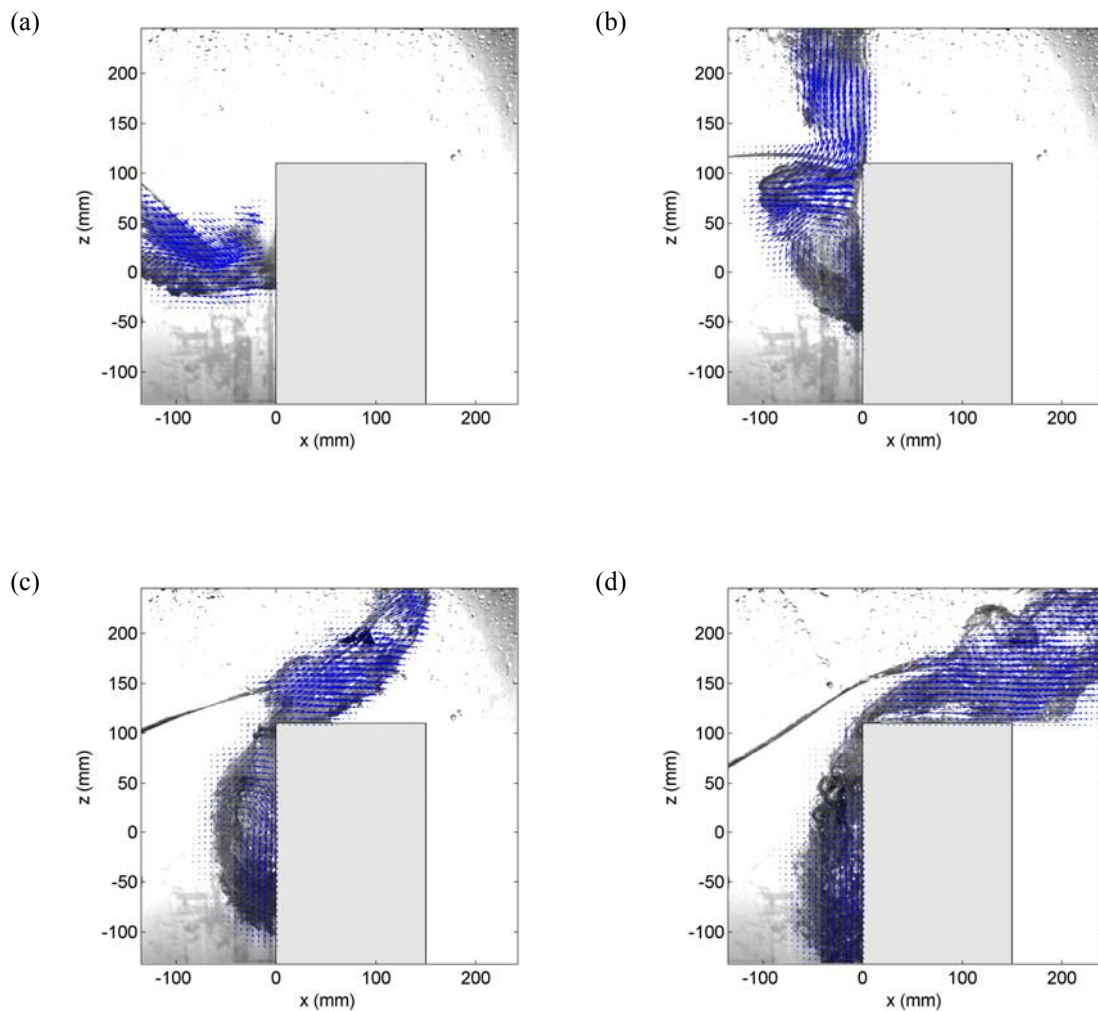


Fig. 3.11. Flow field of plunging breaking wave impinging on structure measured by BIV method.

In addition to the interaction between the breaking wave and structure, there were BIV measurements successful in measuring air-water mixture flows. Fig. 3.12 shows the flow field of a plunging breaker after impinging on free surface measured by the BIV method. The measurements were performed by Ho-Joon Lim at Texas A&M

University. The velocity fields in the aerated region of the plunging breaker after impinging is measured by the BIV technique successfully as shown in two consecutive velocity maps of the figure. Note that the velocity fields have instantaneous images for a background of the velocity maps.

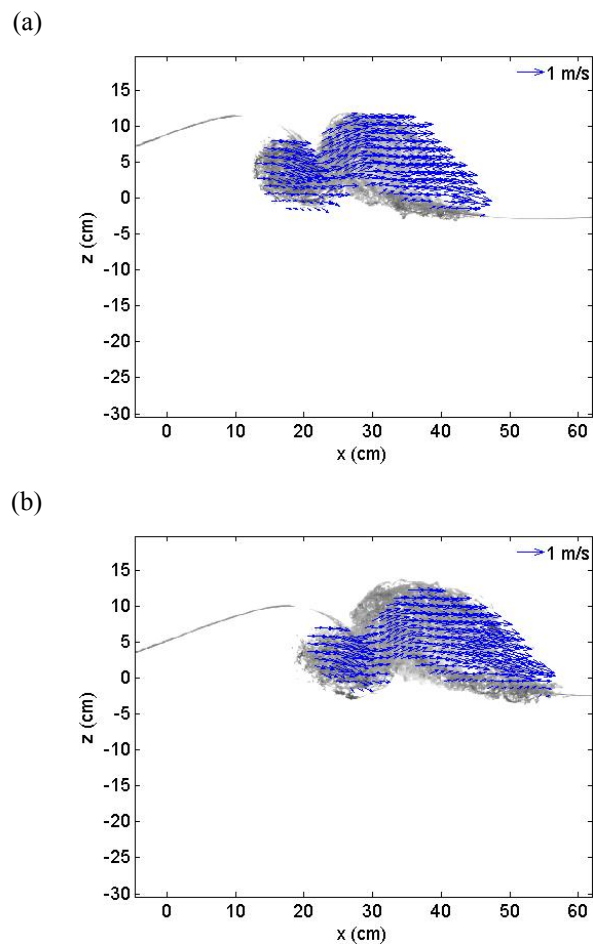


Fig. 3.12. BIV measurement of breaking wave after impingement (courtesy of H.-J. Lim).

Lin et al. (2006) also measured the aerated region of a hydraulic jump using the BIV method. A hydraulic jump is one of well-known air-water mixtures. Fig. 3.13

(a) shows the instantaneous image of an aerated hydraulic jump and Fig. 3.13 (b) shows a corresponding velocity field measured by BIV. Note that the figure is shown in this dissertation by courtesy of Prof. Lin. Vortex structures and very turbulent flows in the aerated region of the hydraulic jump are well-demonstrated by the velocity fields obtained by BIV. They also compared the BIV results with PIV measurements for non aerated region occurring below the aerated region. From the comparison of good agreements, it is shown that fluid velocity follows bubble velocity in an aerated region for a case with relatively large inertia momentum like a hydraulic jump.

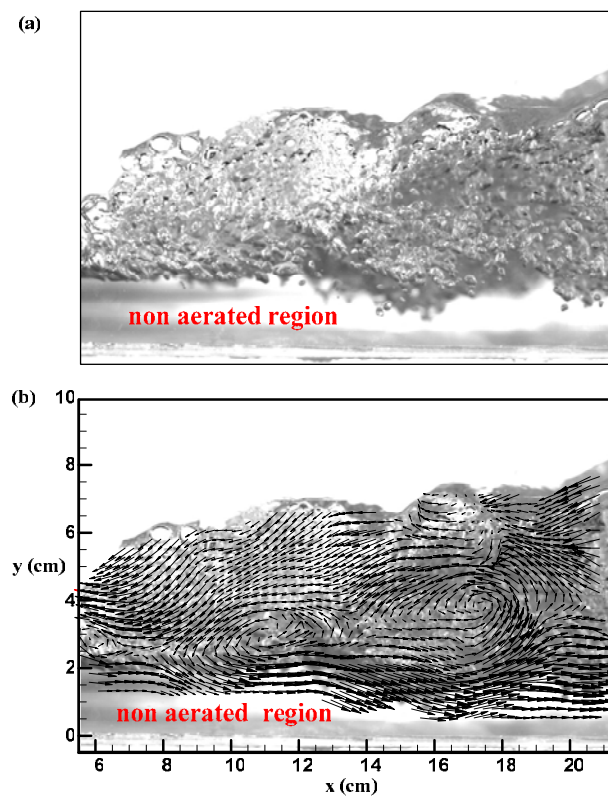


Fig. 3.13. Instantaneous flow pattern and velocity field of aerated hydraulic jump measured by BIV (courtesy of Prof. Lin, National Chung Tsing University).

3.7 Conclusion

In the present chapter, a newly developed measurement technique, bubble image velocimetry (BIV), was presented as a method capable of measuring velocity fields of air-water mixture. While the PIV technique was only capable of obtaining velocity fields outside an aerated region, the BIV technique successfully measured the velocity field in an aerated region of air-water flow. The BIV technique is indeed a modified PIV technique with images captured based on a modified shadowgraphy technique. The technique does not require the use of a laser thus has a much lower cost and easier to setup. The BIV technique was validated by comparing the velocity measured using the FOR method. The BIV technique measures velocity mainly in the multiphase region where the PIV technique does not work well or does not work at all. The technique therefore can be considered as a complimentary technique for PIV in the study of high void fraction multiphase flows such as breaking waves and hydraulic jumps.

CHAPTER IV

BREAKING WAVE IMPINGING AND OVERTOPPING: MEASUREMENT AND PREDICTION

4.1 Introduction

The interaction between the extreme waves and floating structures is of primary concern in the design of costal and offshore structures. In the past extreme waves have caused significant damages to offshore structures due to the tremendous forces created by wave impingement (Oumeraci et al., 1993; Hattori et al., 1994; Zhang et al., 1996). Green water loads by associated overtopping wave on offshore platform occur when an incoming wave significantly exceeds the free board and water runs on the deck (e.g., Buchner, 1995; Hamoudi and Varyani, 1998; Schoenberg and Rainey, 2002). Frequently, green water washes out and damages equipment on the deck and in some cases causes injury or death to persons working on the deck. Green water also could affect the stability of offshore structures. One recent example is the green water damage caused by Hurricane Ivan in the Gulf of Mexico in 2004 that damaged several offshore platforms. Since the occurrence of hurricanes with higher intensity winds becomes frequent, structures in the ocean and coast may be subjected to severe green water. Fig. 4.1 shows a green water incident on the Selkirk Settler in mid Atlantic in 1987.



Fig. 4.1. Green water incident at the side of the Selkirk Settler. Photograph by Captain G. A. Ianiev (courtesy of Prof. Douglas Faulkner) from Schoenberg and Rainey (2002).

Vertical walls of both maritime and offshore structures can suffer from large wave forces if subjected to direct impacts by extreme waves. Due to the complex of wave shape and breaking shape and the disposition of air-water mixture of breaking waves, impact pressures are very difficult to predict. A number of studies have focused on the experimental measurement of wave impact pressures for both offshore and maritime structures and some for shallow water condition investigated the relation between the shape of wave and the effect of this shape on the impact pressure magnitude and distribution. Although there were studies relating impact pressures to breaker shape, experimental techniques used in the studies were limited in recording the very

fast events near impacting. The experimental study to identify the role of breaker shape on wave impact pressures was conducted by Oumeraci et al. (1993, 1995) with combining measurements of wave impact pressures with visual records of the wave shape to identify. He found four different categories of breakers depending on the characteristics of impact loads by the type of wave breaking and by the kinematics of the breaker. Hattori et al. (1994) used a higher speed video camera for similar experiments combined with six pressure transducers. This study focused on the effect of entrapped air between breaking waves and a wall and it was found that the case with smallest entrapped air bubble has the highest impact pressures. Oumeraci et al. (1995) measured the particle velocities in three different breaking waves categorized by entrapped air pocket size using particle image velocimetry in order to develop a relationship between velocity, mass and pressures for prediction purposes. Although there have been efforts to measure kinematics of breaking waves impacting on a wall such as Oumeraci et al. (1995), limits like low measurement rate of techniques or air-water mixture nature of breaking waves have been obstacles to kinematics measurements. Hull and Müller (2002) also performed similar experiments in order to refine previous studies and find the effect of deep water wave height on breaker type and impact pressures. They found that locations where a maximum impact pressure are different depending on breaker shape and there is no clear relation between offshore condition and resulting breaker shape or impact pressures. On the other hand, there have been other numerical approaches mainly focusing on the forces of the waves on structures and simple flow field kinematics. Most of these studies were based on the potential flow

theory therefore the nature of the multiphase highly turbulent flow in the problem is not realistically simulated. The results were therefore at most for the “engineering use” for prediction of global wave forces rather than looking into the physical insight of the phenomenon with a resolved accuracy in velocity, pressure, and force distributions. Recently, more advanced approaches, either based on the Reynolds averaged Navier-Stokes equations (RANS) or large eddy simulation (LES), that feature turbulent models and provide much more physical insight have started to be used in the study (e.g., Lin and Liu, 1998a, 1998b; Watanabe and Saeki, 1999; Christenson and Deigaard, 2001). However, only limited success has been achieved due to the lack of comprehensive treatments on the splashing water over the free surface and the high void fraction bubbly flow, and lack of experimental data to validate the calculations and the numerical models.

Green water damage to floating structures results from high pressures and loads that occur when wave crests inundate the structure far above the waterline in areas not designed to withstand such pressures. Green water damage is often associated with use of floating structures in operations or locales for which they were not initially designed. Modification of existing floating structures to prevent green water damage is often difficult to achieve, and prevention is generally approached through localized reinforcements or barriers added to the structure and/or modified operating procedures. The green water problem has been investigated experimentally and numerically. Among the experimental studies, Buchner (1995a, b) presented experimental investigations based on model tests with a floating production storage and offloading (FPSO) unit. From various tests, he suggested that the green water occurrence and

loading are strongly dependent on conditions of the ocean such as wave period, wave height and current velocity. In the studies, he showed the resemblance of green water to a dam break flow and commented that the application would be limited due to the shallow water assumption. Buchner (1996) later investigated the effect of green water with different bow shapes. Hamoudi and Varyani (1998) investigated the probability of green water occurrence for various Froude numbers and wave heights experimentally. The study examined the number of deck wetness through laboratory tests to compute the probability of occurrence and compared it with the experimental works of other researchers. They also found that there is no direct relation between the velocity of waves and the velocity of green water on the deck.

Among the numerical studies, Maruo and Song (1994) studied the effect of the wave steepness on green water in the bow region using a boundary element method. They simulated the case with a high speed vessel two-dimensionally. Nielsen and Mayer (2004) used a Navier-Stokes solver with a volume-of-fluid scheme to model the green water loads on a vessel with and without motions in both 2D and 3D. The model shows good agreement in 2D comparison between the water level on deck and experimental data in Buchner's (1995a) study. In their extended study to 3D, they found that the 3D effect is insignificant.

Since very few non-intrusive quantitative velocity measurements of breaking waves impinging on structures exist, we thus review the measurement of breaking waves instead. The measurement on breaking waves itself has been of great interest to numerous researchers. Various measurement techniques, including laser Doppler

velocimetry (LDV) and particle image velocimetry (PIV), have been employed for the velocity measurements of the wave breaking process in both surf zone and deep water (e.g., Greated and Emarat, 2000; Ting and Kirby, 1994, 1995; Perlin et al., 1996; Chang and Liu, 1999, 2000; Melville et al., 2002). As a wave breaks and entrains air bubbles, the technique is then restricted to the region outside the aerated area, in general under the trough level or away from the breaking point and there have been few studies measuring the aerated region of breaking waves. Even though the PIV technique have been successfully used to measure bubble velocity by correlating bubbles or tracking each bubble in the recorded images that were taken by applying the “shadowgraphy” method (Hassan et al., 1998; Nishino et al., 2000; Lindken and Merzkirch, 2001), the two methods above are used in low void fraction flow with small bubbles, and may not be applicable in breaking wave measurements.

In this chapter, this study presents an experimental study on the kinematics of plunging waves impinging and overtopping a model structure both with and without an extended deck. The velocity field in front of the structure before wave impingement was obtained using PIV while the velocity field in the aerated region in the vicinity of the structure was measured using BIV. From repeated experiments, the mean and turbulence properties were extracted from the instantaneous velocity measurements. Based on the measured data, an empirical equation for the green water velocity profile was developed by applying dimensional analysis. Comparisons among the measured green water velocity, the prediction model are made. Finally, the equation was used to predict the maximum green water velocity on an offshore platform during Hurricane

Ivan based on field data provided in Wang et al. (2005).

4.2 Experimental setup and techniques

4.2.1 Wave tank and model structure

The experiments were performed in a glass-walled wave tank which is 36 m long, 0.9 m wide and 1.5 m high with water depth of $d = 0.80$ m throughout the experiments and a rectangular model was located 21.7 m away from the wave tank. The rest of the setup about the wave tank and model is detailed in Chapter II. A wave used through the present study was a plunging breaker. The plunging breaker was generated by the wave focusing method since the wave condition was of deep water. The generation of the breaking wave was explained in detail in Chapter II. The wave elevation was measured at two locations, which were 5 m from the wavemaker and right in front of the structure using resistance type piercing gages. The free surface elevations are shown in Fig. 2.3.

4.2.2 PIV technique

The PIV technique in the present study was used to measure the velocity field near the front wall of the model structure focusing on measurements of impingement of the plunging breaker. Because the overturning jet of a plunging breaker is of importance among the flow fields of breaking waves, a laser light sheet was placed to illuminate particles inside the overturning jet when impinging. In this study, the laser

light sheet came from the frontal top obliquely. The condition of the PIV system was explained in Chapter II and the same condition was used in this study.

4.2.3 BIV technique

The BIV method was used to measure the whole velocity field in front of and on top of the structure. In order to cover the whole field in the vicinity of the structure, two different FOVs were used depending on the length of the deck. In the experiments, regular 600 W light bulbs with reflecting mounts as light source were used to illuminate the flow. The images were captured by two Phantom high speed cameras mounted with a Nikon 105 mm micro focal lens. One of the cameras used for the measurements of the model without the extended deck (FOV 2 in Fig. 2.2) has a resolution of 512×512 pixels, an 8-bit dynamic range, and a maximum framing rate of 1000 fps. The other one, borrowed from National Chung Hsing University in Taiwan, is a newer version of the first camera. This newer one has a resolution of 1024×1024 pixels, the same dynamic range, and a maximum framing rate of 1200 fps, and was used for the model test with the extended deck (FOV 3). In this study, the resolution used for the newer camera was set at 1024×768 pixels and the camera is capable of measuring up to 1680 fps with that resolution. The aperture of the focal lens mounted on both cameras was set at f/1.8. Because the conditions of the both cases are almost same, errors due to the thickness of depth of field (DOF) of both cases was near 2%.

The FOV of the BIV measurement for the model without the extended deck is 37.8 cm × 37.8 cm and centered at $x = 5.2$ cm and $z = -5.3$ cm as shown in Fig. 2.2

(denoted as FOV 2). The first high speed camera (the older version) was used to capture the images. The time interval between the consecutive recorded images was 1.75 ms that is equal to the time separation between the consecutive frames captured by the camera. The images were processed using the LaVision PIV software and the velocity field was calculated using an adaptive multi-pass algorithm with an initial interrogation window size of 32×32 pixels and a final window size of 16×16 pixels with a 50% overlap between the adjacent windows. In addition, FOV 3 for the model with the extended deck is $41.0 \text{ cm} \times 27.5 \text{ cm}$. The images were captured using the newer version camera with a framing rate set at 1000 fps, i.e., a time interval of 1 ms between images. Velocities were obtained using the same software and the same algorithm but with an initial interrogation window size of 64×64 pixels and a final window size of 32×32 pixels with a 50% overlap. A median filter was subsequently applied to eliminate the spurious vectors in the calculated velocity maps. The mean velocity was calculated from ensemble averaging 10 instantaneous velocity fields for the measurements of FOV 2 and 20 for FOV 3 from repeated runs with the same test condition.

4.3 Mean flow field by PIV

The velocity measurement in the vicinity of the model structure was first carried out using the PIV technique. If a spilling type of breaking wave impinges on the structure, the air pocket between the wave front face and the structure is relatively small. In such a condition the majority of the region in front the leading edge of the structure is

not highly aerated and is suitable for PIV. The measurement taken at FOV 1 (shown in Fig. 2.2) is shown in Fig. 4.2 (i) to 4.2 (iv). However, even for the cases with only a small air pocket, green water on the deck of the structure due to overtopping is highly aerated and not ideal for PIV. If the impinging wave is of plunging type, a large air pocket in front of the structure will form immediately and cause severe laser light scattering and result in saturated and not useful images for PIV correlation in the image processing. The problem continues, if not gets worse, to green water on top of the structure. Figs. 4.2 (a) to 4.2 (d) show the PIV measurement of the plunging breaking wave. Clearly there exists a large region where no velocity vectors were obtained due to the large amount and size of air bubbles. A similar problem was also observed in Chang and Liu (1999, 2000). One interesting thing worth pointing out is that the maximum horizontal velocity in Fig. 4.2 reached 1.5 times the phase speed of the wave, C . This result is consistent with that reported in Chang and Liu (1998). Fig. 4.3 shows the cross sectional horizontal velocities along the x axis corresponding to Figs. 4.2 (a) to 4.2 (d). Cross sectional velocity, denoted as U_C , is the maximum horizontal velocity of a vertical column at a location along the deck. As shown in Fig. 4.3, the largest magnitude around $1.5C$ persisted for a certain period of time, corresponding to the instant in Figs. 4.2 (b) to 4.2 (d).

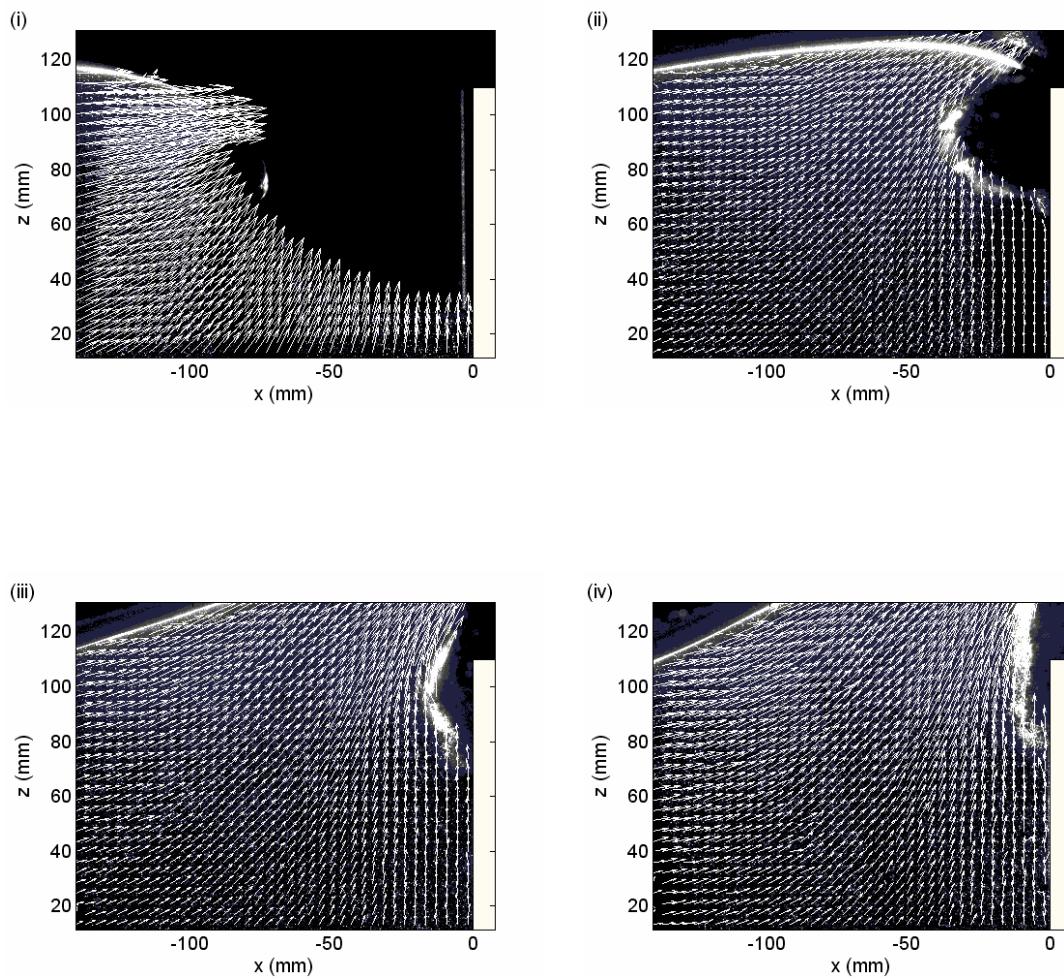


Fig. 4.2. PIV measurement of breaking waves impinging on structure: (i-iv), spilling breaker with a small air pocket; (a-d), plunging breaker with a large air pocket. The time separation between the consecutive frames is 25 ms.

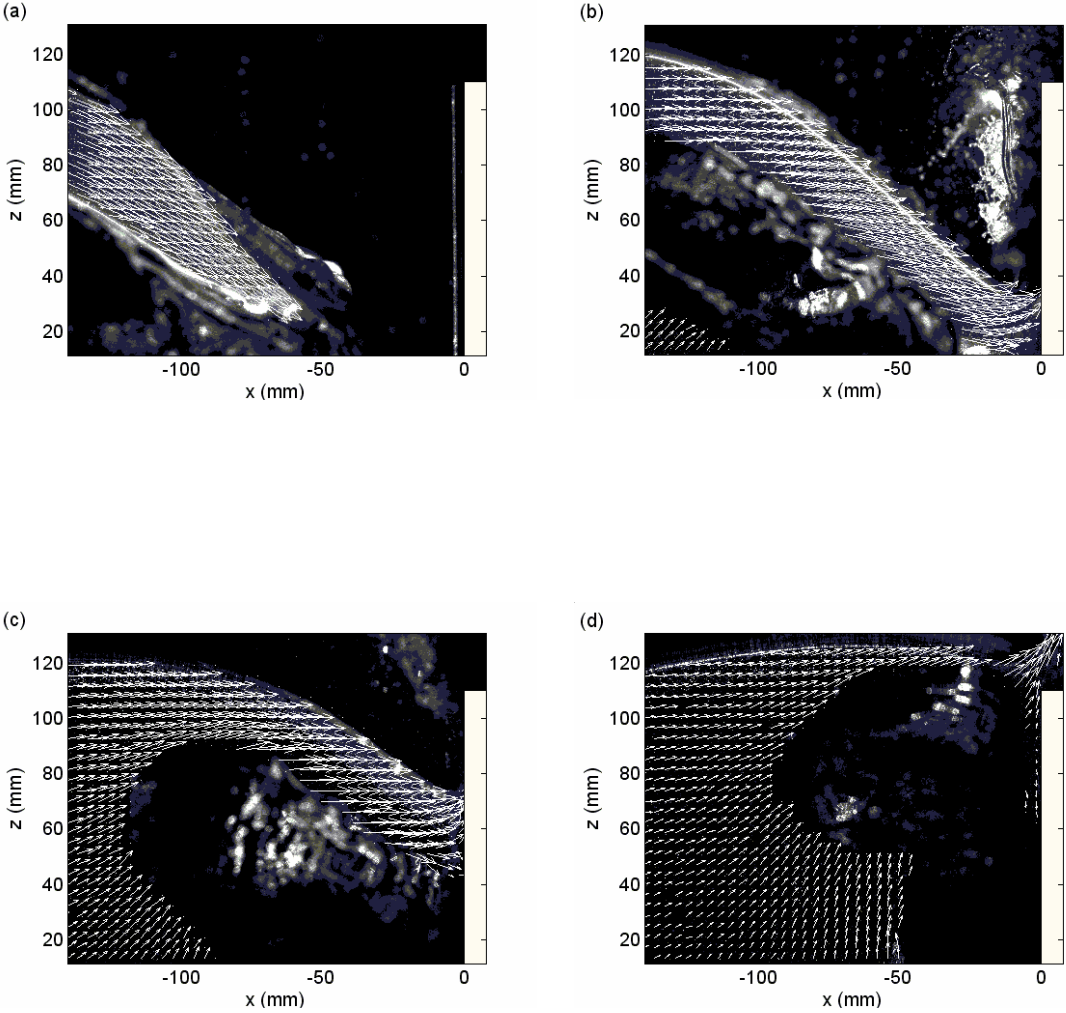


Fig. 4.2 (continued)

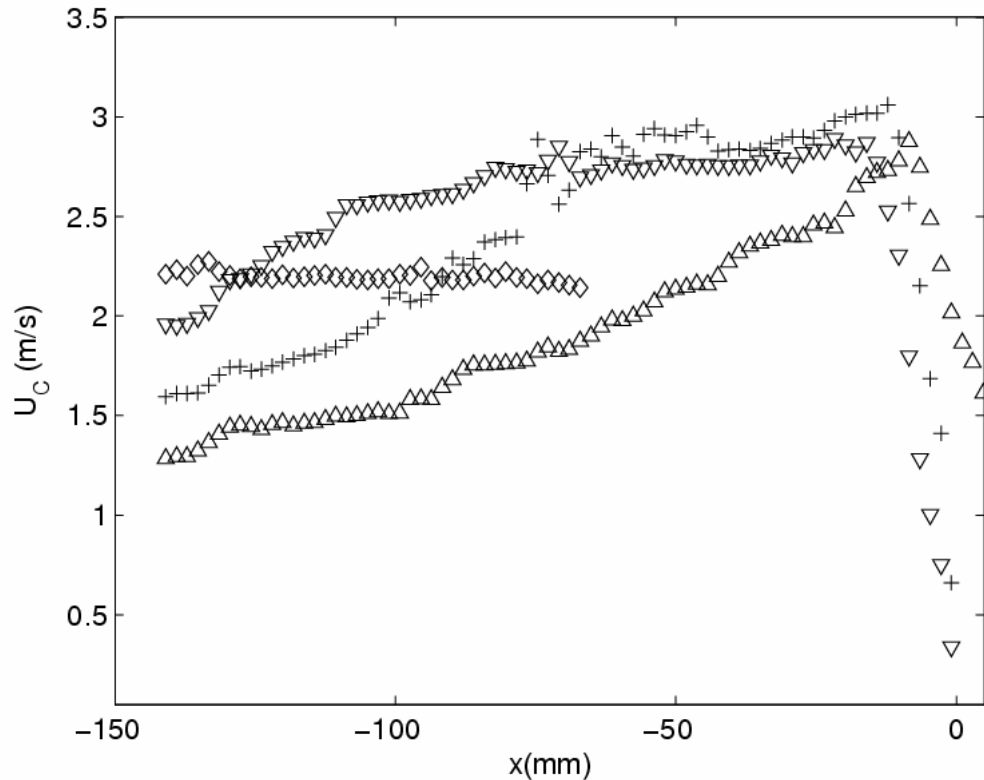


Fig. 4.3. Maximum cross-sectional horizontal velocities measured by PIV along the x axis. “◇”, t_0 ; “▽”, $t_0 + 0.025$ s; “+”, $t_0 + 0.050$ s; “△”, $t_0 + 0.075$ s.

4.4 Mean flow field by BIV: short deck and extended deck

Fig. 4.4 shows the velocity fields measured using the BIV method. The length of the deck is 0.15 m long without the 0.22 m long extension section added (see Fig. 2.2). The tested wave is the same as one used for the PIV measurements. The field of view is shown in Fig. 2.2 and denoted as FOV 2. The entire sequence of velocity field during the impinging and green water processes is demonstrated in the figure. The mean velocity, turbulence intensity, and turbulent kinetic energy were obtained by

phase-averaging the measured instantaneous velocities at each phase, i.e.,

$$\langle u_k \rangle = \frac{1}{N} \sum_{l=1}^N u_k^{(l)} = U_k \quad (4.1)$$

where the symbol $\langle \rangle$ represents phase average, $u_k^{(l)}$ the k -component velocity obtained from the l^{th} instantaneous velocity measurement, N the total number of instantaneous velocities at that phase, and U_k the phase-averaged mean velocity. Note that the velocity field is the mean velocity obtained from ensemble averaging 10 repeated instantaneous velocity measurements ($N = 10$) while the images were picked from one of the 10 realizations (i.e., the images are instantaneous). Since the wave breaking process is highly turbulent, the instantaneous images do not match the mean velocities perfectly in some instants. Note that $t = 0$ in the figure represents the instant when the free surface of the wave was crossing the leading edge of the structure and overtopping the structure. All the 10 sets of the instantaneous velocity fields were matched at this moment so that errors in the ensemble average due to mismatch of the cases are minimized, if not eliminated. In addition, this determination of $t = 0$ is for the future comparisons with the dam break flow that has been widely applied to describe the green water effect without careful validation. Thus, the moments before $t = 0$ are denoted as negative time.

Fig. 4.4 (a) shows the moment right after the overturning jet touched its front water surface and before it touched the front wall of the structure. The jet velocity is moving downstream and mainly downward. After a short duration of 35 ms in Fig. 4.4 (b), the overturning wave impinged the structure frontal wall and splashed upward. At

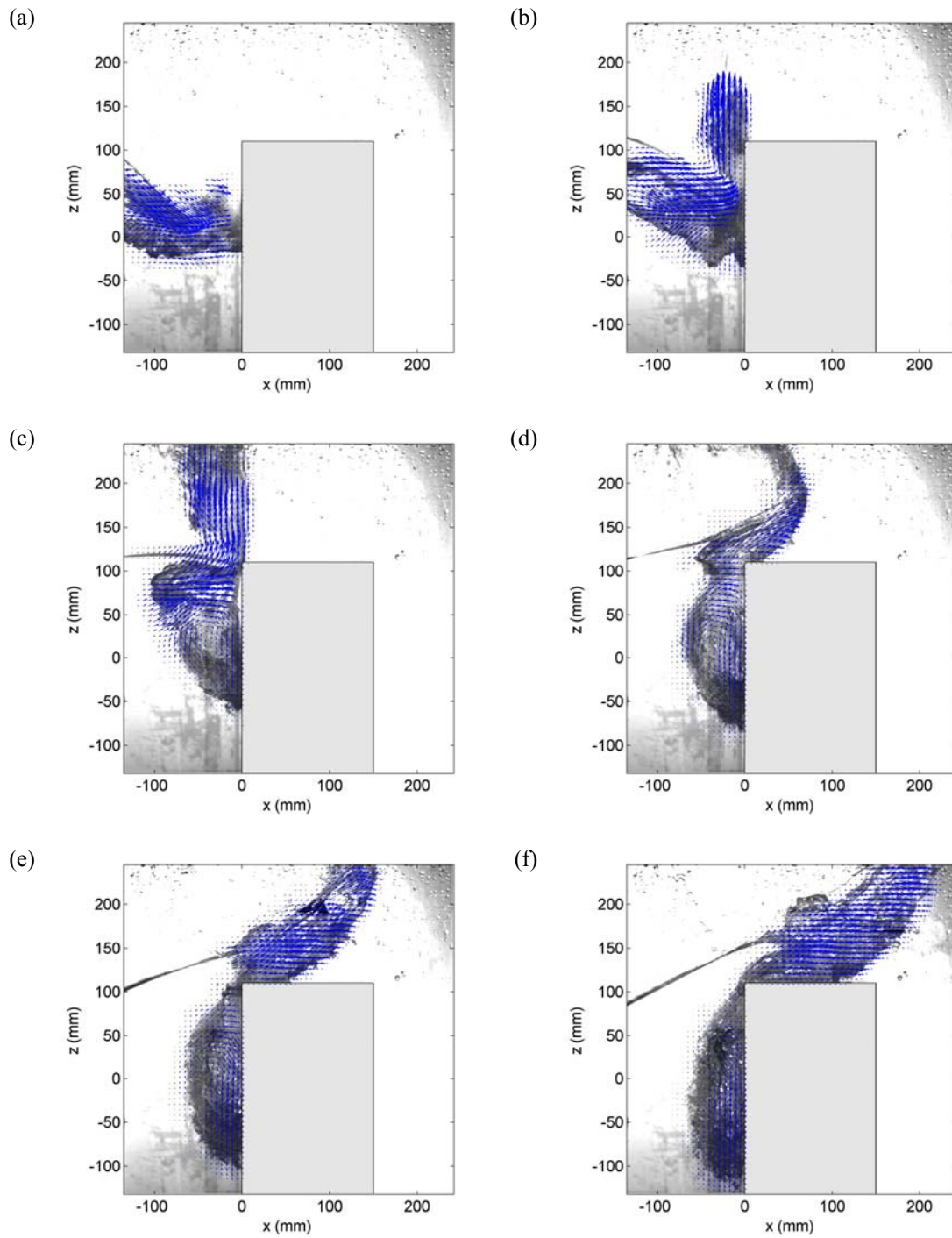


Fig. 4.4. Mean velocity fields obtained by BIV at $t =$ (a) -0.07 s, (b) -0.035 s, (c) 0.000 s, (d) 0.035 s, (e) 0.070 s, (f) 0.105 s, (g) 0.140 s, (h) 0.175 s, (i) 0.210 s, (j) 0.245 s, (k) 0.280 s, and (l) 0.315 s.

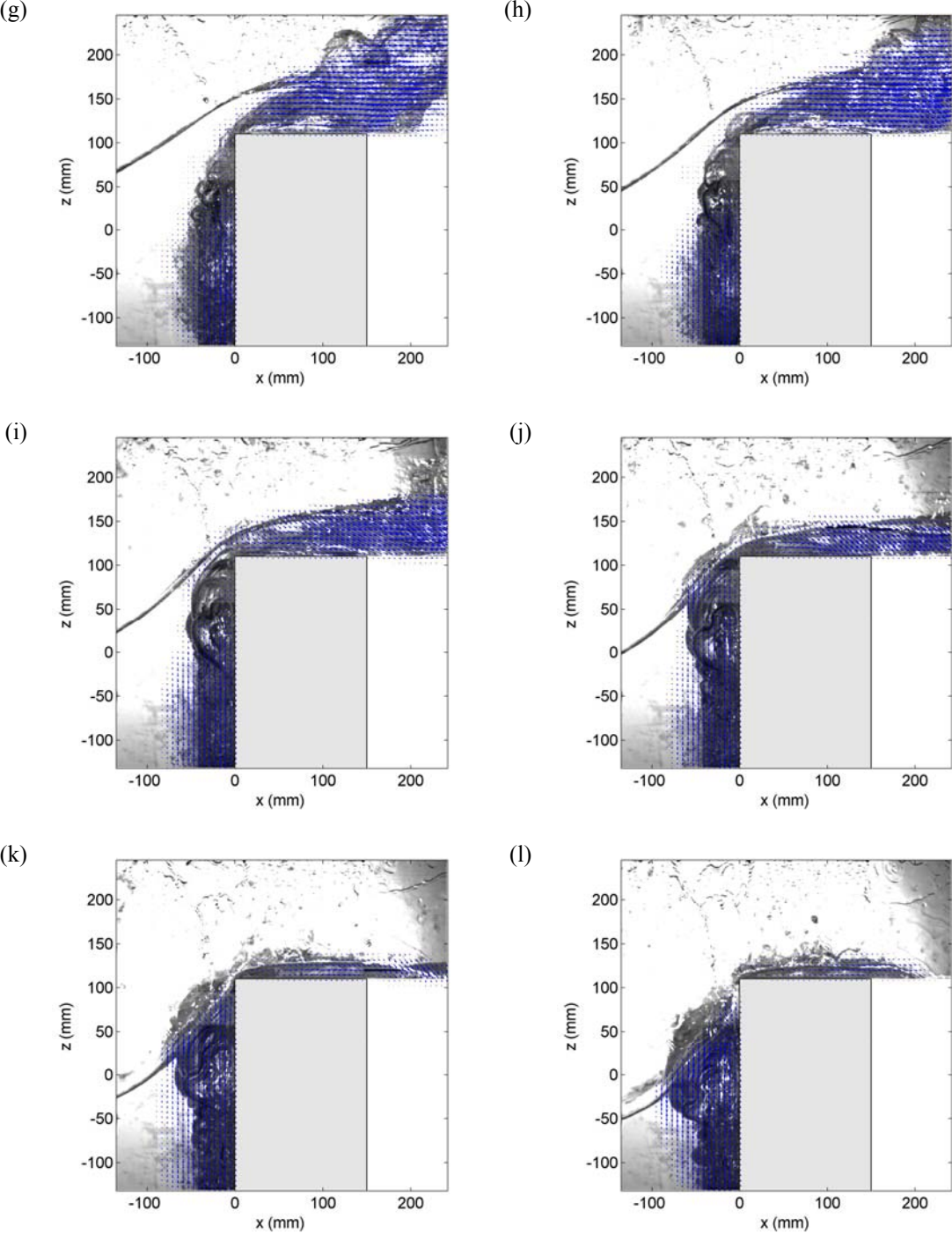


Fig. 4.4. (continued)

this moment a large part of wave was still moving horizontally towards the structure while the splashing jet was moving vertically upward. The process continued through Fig. 4.4 (c) until the wave momentum pushed the wave front to move forward onto the deck, as shown in Fig. 4.4 (d). At the same time right in front of the structure, when the wave momentum pushed part of the water to move upward, it also pushed part of the water to move downward and created a large vortex at around $z = 0$, started in Fig. 4.4 (c). The upward water did not touch the deck surface until the instant in Fig. 4.4 (e). The horizontal velocity on the deck was small initially until the water started to touch the deck. In Figs. 4.4 (f - g) the green water lost its vertical momentum and the velocity became completely horizontal. This motion could create a large horizontal force exerting on any objects located on the deck due to the large horizontal momentum of water. Since the deck is not long (and this is typically the case for an offshore platform), the green water on top of the deck passed the deck and moved downward back to the “ocean” quickly at the rear edge of the deck. The velocity of green water continued to move downstream but started to change to downward direction as seen in Figs. 4.4 (h - i). After that the green water quickly recessed and lost its momentum with the velocity being significantly reduced, as seen in Figs. 4.4 (j - l).

Fig. 4.5 shows the profiles of cross sectional maximum horizontal velocity, U_C , of the green water with its velocity fields shown in Fig. 4.4. The plot starts at $t = 0.035$ s because the horizontal momentum of the green water becomes dominant after this instant, as shown in Fig. 4.4 (d). Fig. 4.5 displays the profile of U_C at five different instants with a time separation of 70 ms. The velocity along the deck has a non-linear

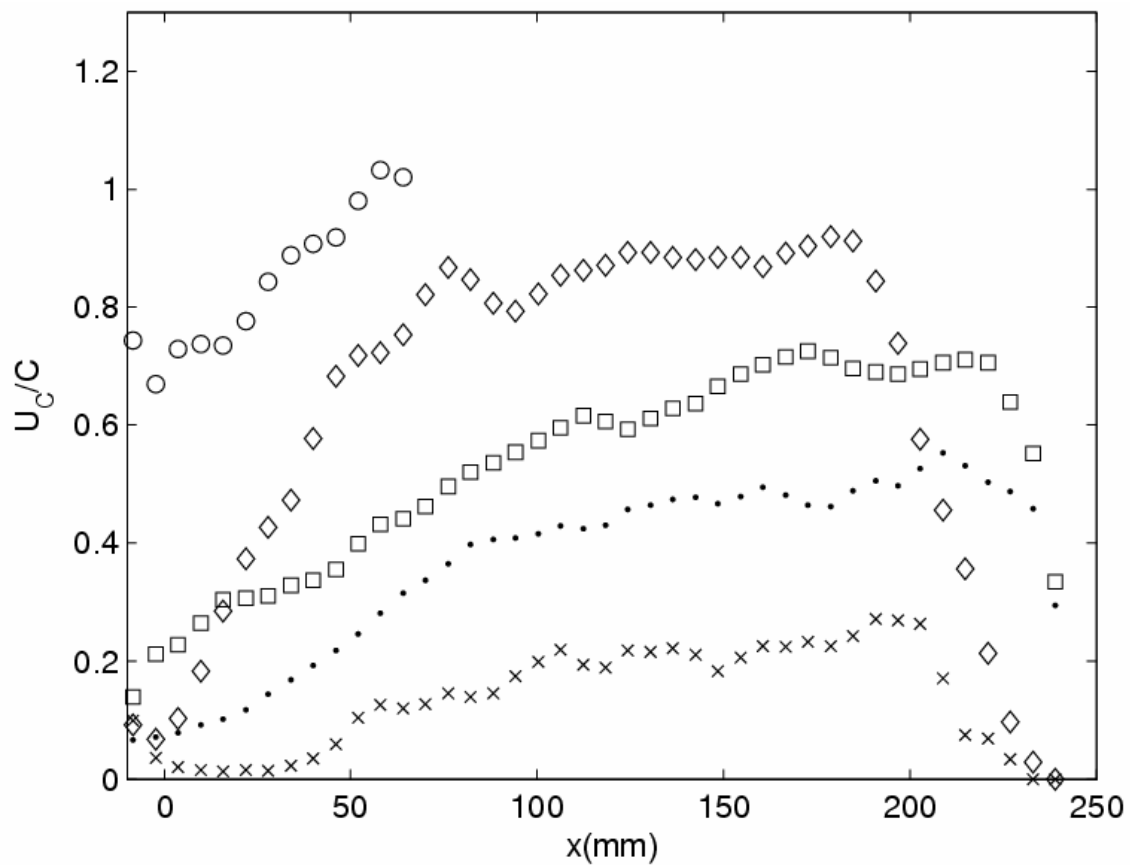


Fig. 4.5. Cross-sectional velocity on the model with the short deck at time at $t = 0.035 \text{ s}$ (o), 0.105 s (\diamond), 0.175 s (\square), 0.245 s (\cdot), and 0.315 s (\times).

behavior, different from the linear solution of a dam break flow (will be discussed later). Interestingly, the location where the maximum cross-sectional velocities occurred are not at the front of the green water (but close) except at $t = 0.035 \text{ s}$. One possible reason for such a trend is that the green water moved downward at the end of the deck and the

momentum becomes vertical as shown in the velocity field in Fig. 4.4. Note that $t = 0.035$ s is the instant before the green water reached the end of the deck. The maximum magnitude of U_C was about $1.05C$, indicating the maximum water speed of green water on the deck is approximately the phase speed or slightly higher than the phase speed. Since the green water passed the deck very fast (within 10 ms), it is very difficult to find a full flow pattern of the green water with the model structure. Thus, it may be necessary to conduct tests using a structure with a longer deck in order to better understand the behavior of green water.

Fig. 4.6 shows the velocity field of the same breaking wave as in Fig. 4.2 impinging on the structure with the extended deck. Again, the BIV technique was used in the measurement and the newer high speed camera was employed in the image acquisition. The field of view is shown in Fig. 2.2 and denoted as FOV 3. Fig. 4.6 is the mean velocity field obtained from ensemble averaging 20 instantaneous measurements. The case with the extended deck shows the similar velocity pattern as in the previous case without the extended deck until the moment when the wave is on the top of the deck. This means the velocities are very similar between long deck and short deck cases before reaching the instant corresponding to Fig. 4.4 (h). The instant of Fig. 4.4 (h) corresponds to that between Figs. 4.6 (k) and 4.6 (l). Note that the time separation between the adjacent frames in Fig. 4.6 is 20 ms while that in Fig. 4.4 is 35 ms. Since the deck is long in this case, green water on top of the deck initially moved

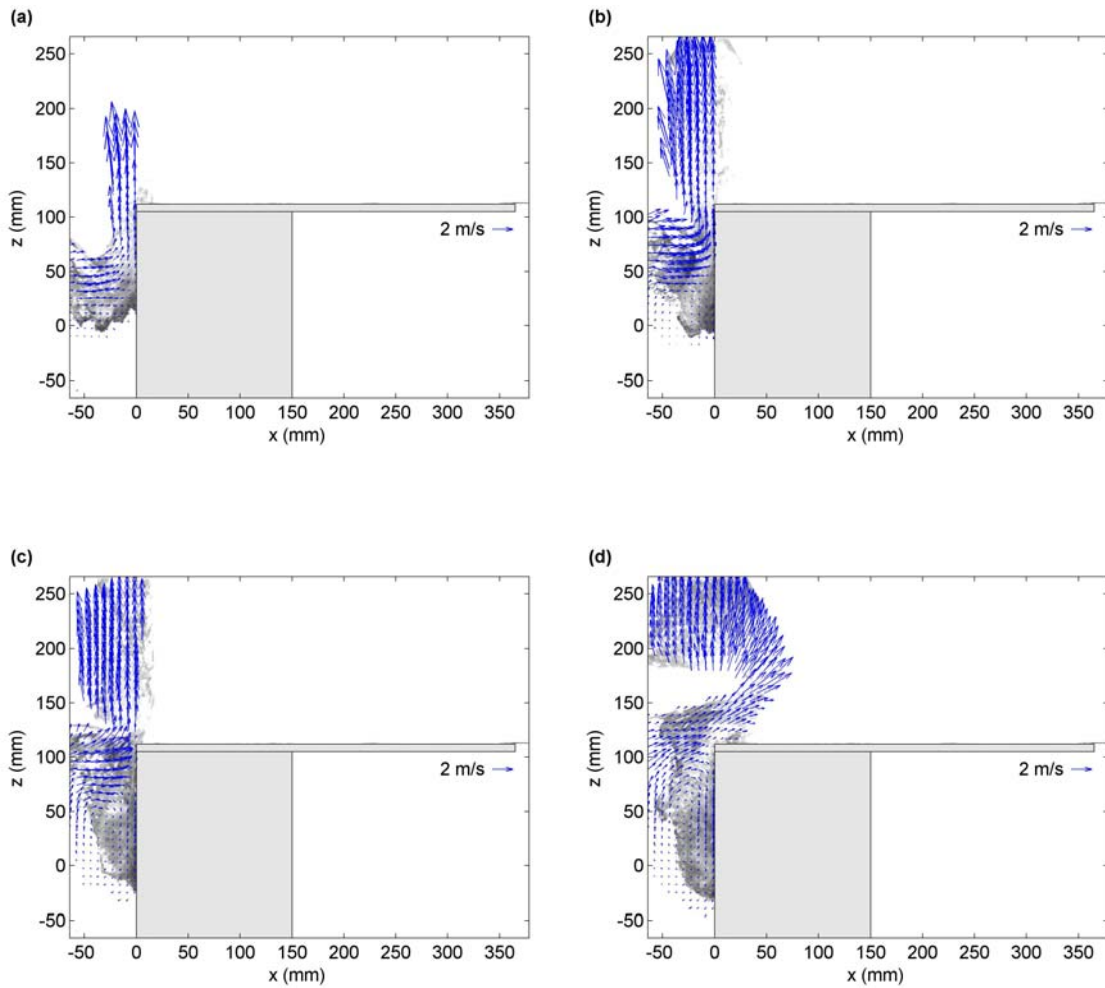


Fig. 4.6. BIV measured mean velocity fields of plunging breaking wave impinging on structure with the extended deck at $t =$ (a) -0.04 s, (b) - 0.02 s, (c) 0.00 s, (d) 0.02 s, (e) 0.04 s, (f) 0.06 s, (g) 0.08 s, (h) 0.10 s, (i) 0.12 s, (j) 0.14 s, (k) 0.16 s, (l) 0.18 s, (m) 0.20 s, (n) 0.22 s, (o) 0.24 s, and (p) 0.26 s.

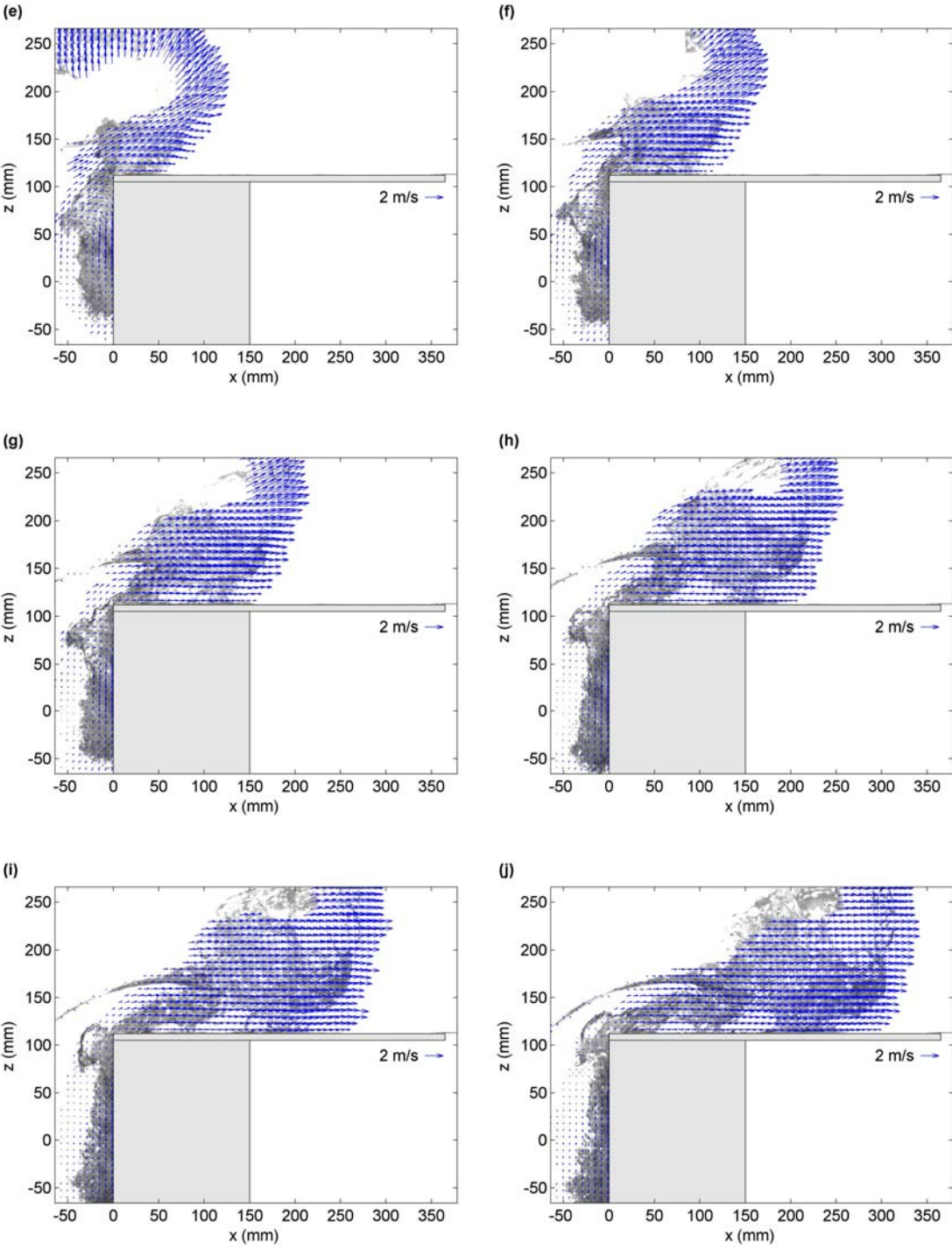


Fig. 4.6 (continued)

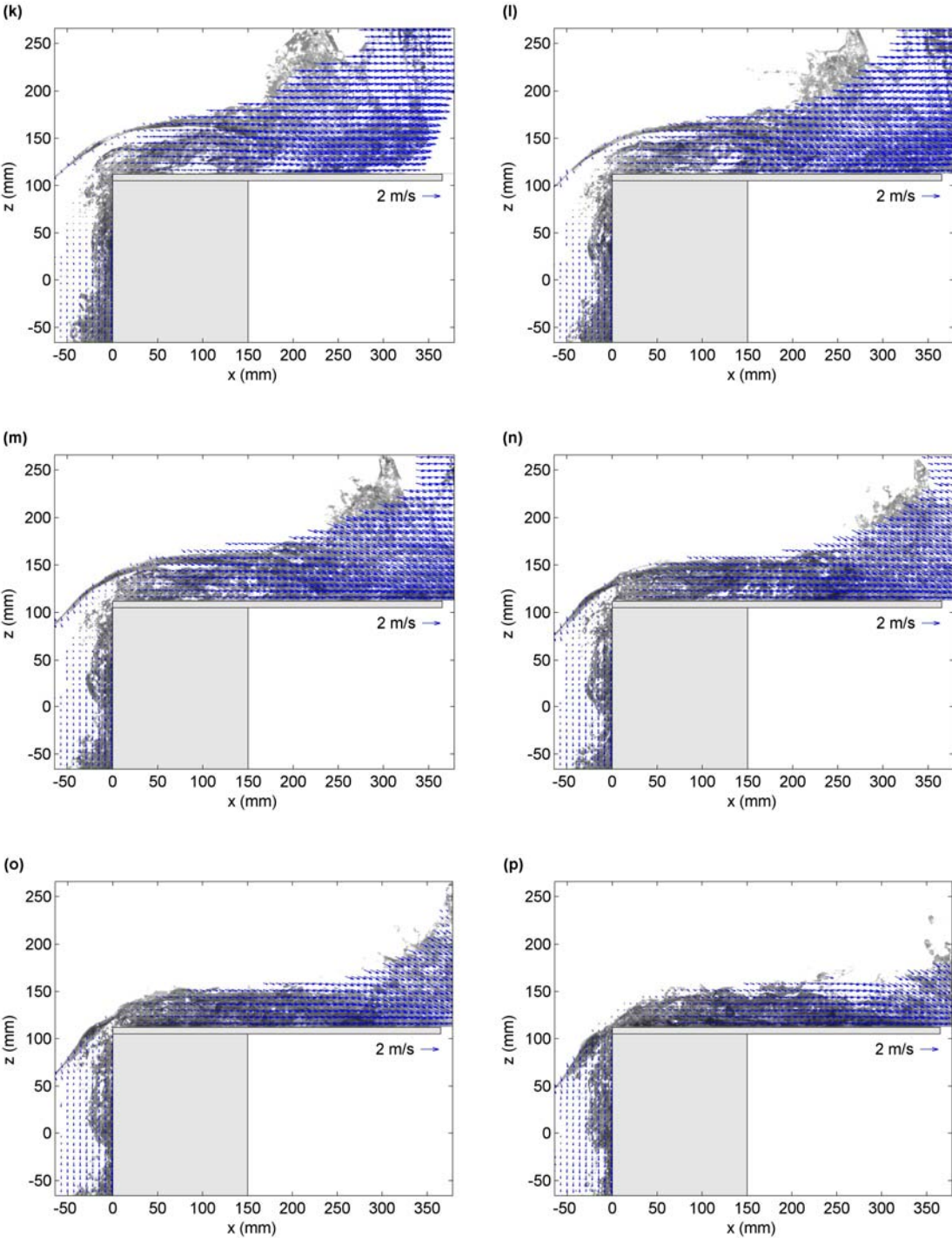


Fig. 4.6 (continued)

downstream horizontally. After the moment in Fig. 4.6 (k), the front of green water passed the end of the deck but continued to have dominant horizontal momentum, as shown in Figs. 4.6 (l – m). Subsequently in Figs. 4.6 (n - p), the green water continued to move along the deck but started to move downward and back to the “ocean” at the rear edge of the deck. After the moment in Fig. 4.6 (p), the green water recessed and lost its momentum, and showed a flow pattern similar to that in the case without the extended deck in Figs. 4.4 (j - l). The pattern of the velocity fields between the short and long deck cases looks very similar except that green water on the long deck stayed a longer period on the deck and the water on the deck moves with a dominant horizontal momentum.

4.5 Turbulence intensity

Fig. 4.7 shows the turbulence intensity, I , corresponding to the flow field in Fig. 4.6. The solid gray line indicates the mean free surface (by averaging the 20 instantaneous images). The instantaneous velocity can be decomposed into the mean quantity and turbulent fluctuations as

$$u_i = U_i + u_i' \quad (4.2)$$

where U_i is a mean velocity and u_i' the turbulent fluctuations. Since only two velocity components were measured, the turbulent intensity is defined as

$$I = \langle u' u' + w' w' \rangle^{1/2} \quad (4.3)$$

where u' and w' are the velocity fluctuations in the x and z directions, respectively. Every frame in Fig. 4.7 has the maximum turbulence intensity, I_{max} , indicated in the

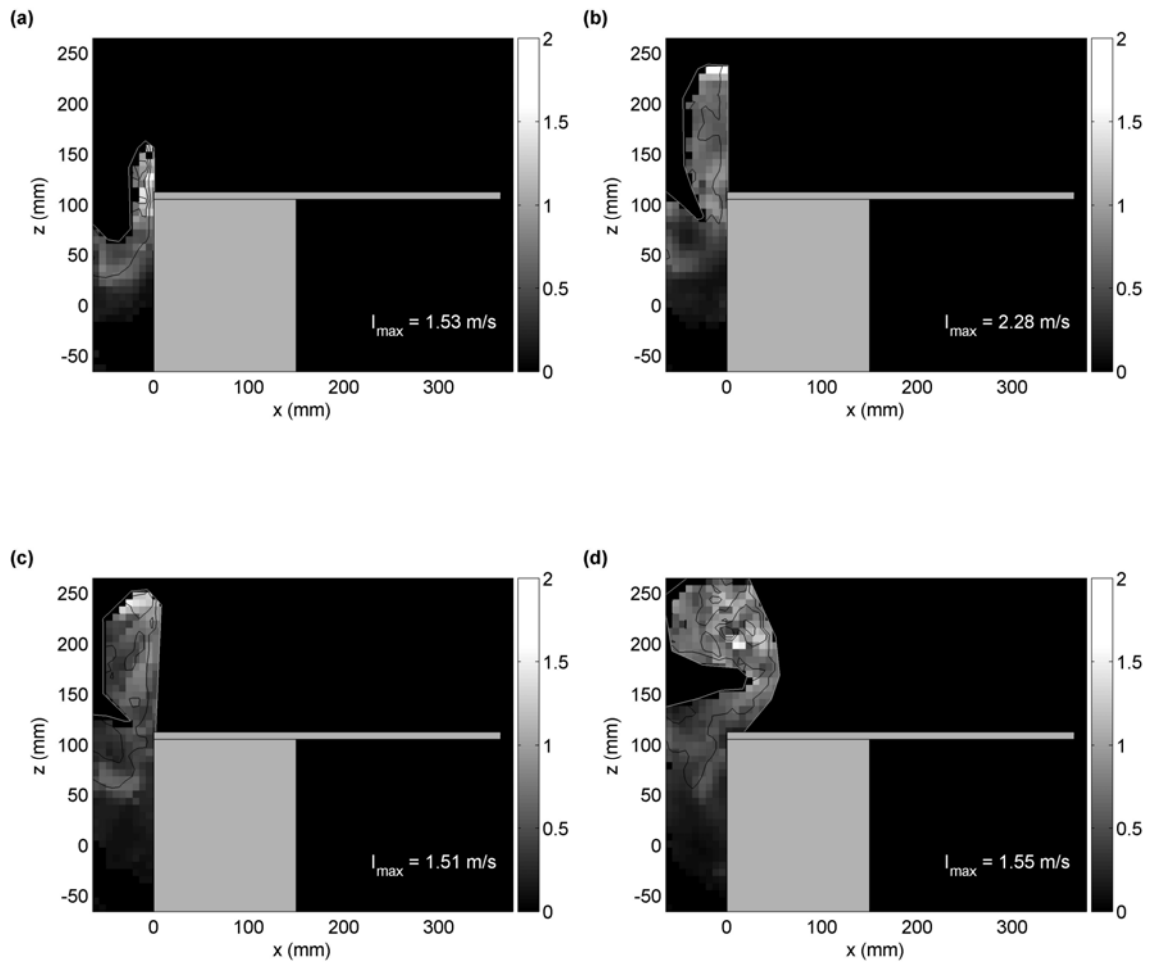


Fig. 4.7: Turbulent intensity I (m/s) corresponding to Fig. 4.6. $t =$ (a) -0.04 s, (b) -0.02 s, (c) 0.00 s, (d) 0.02 s, (e) 0.04 s, (f) 0.06 s, (g) 0.08 s, (h) 0.10 s, (i) 0.12 s, (j) 0.14 s, (k) 0.16 s, (l) 0.18 s, (m) 0.20 s, (n) 0.22 s, (o) 0.24 s, and (p) 0.26 s.

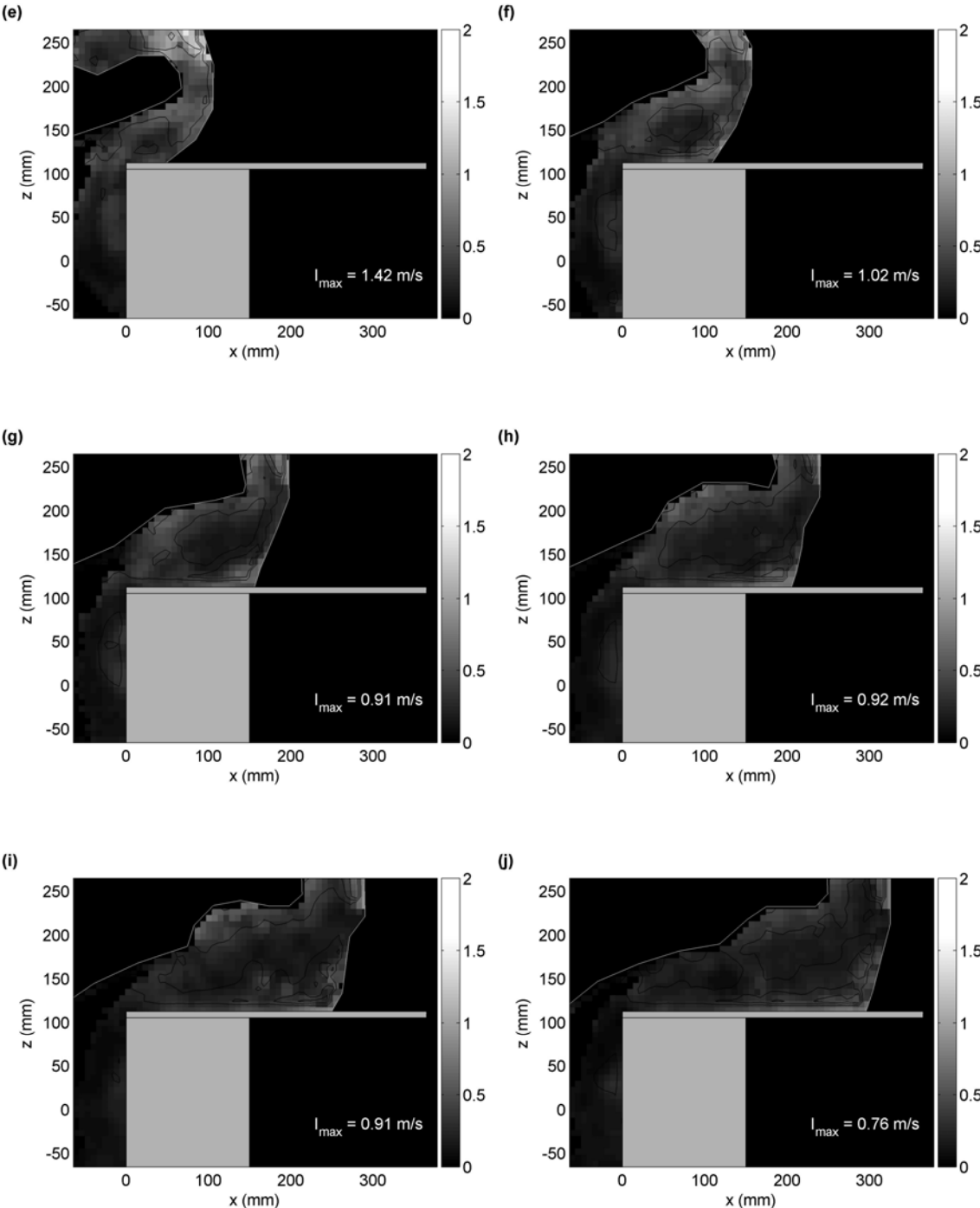


Fig. 4.7 (continued)

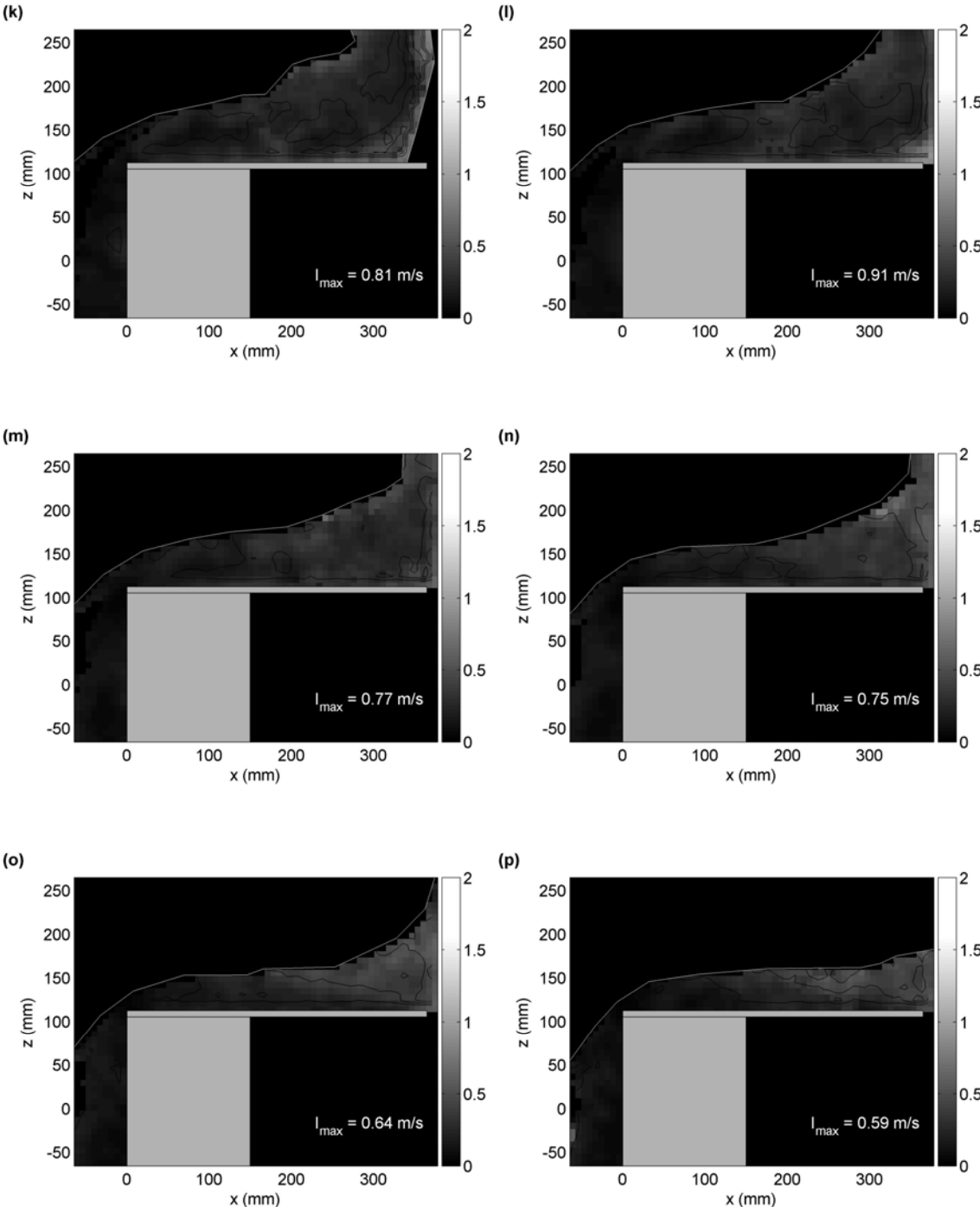


Fig. 4.7 (continued)

panel. The largest I_{max} occurred at $t = -0.02$ sec in Fig. 4.7 (b) and the largest relative values of I_{max} (normalized by the maximum velocity in that panel) occurred during the period in Figs. 4.7 (a-d). During this short period when the splashing water moving upward after hitting the structure, the maximum vertical velocities reached more than 5.0 m/s in the measurements, or more than $2.5C$ (to be discussed later). By examining Figs. 4.6 and 4.7, we found that the region with high turbulence intensity is near the front of the moving green water and coincident with the region with a high mean velocity.

Fig. 4.8 shows the time history of I_{max} and the relative turbulence level obtained by normalizing with the maximum mean velocity, $\langle UU+WW \rangle_{max}^{1/2}$ at the same instant. The relative turbulence levels are somewhat uniform and between 40% and 50 % over entire measurement period except at the very beginning stages. A smaller relative turbulent level was resulted in near $t = -0.02$ s and $t = 0$ s due to the large mean velocity, even though the maximum turbulence intensity occurred at the same moments of about $t = -0.02$ s in Fig. 4.7 (b).

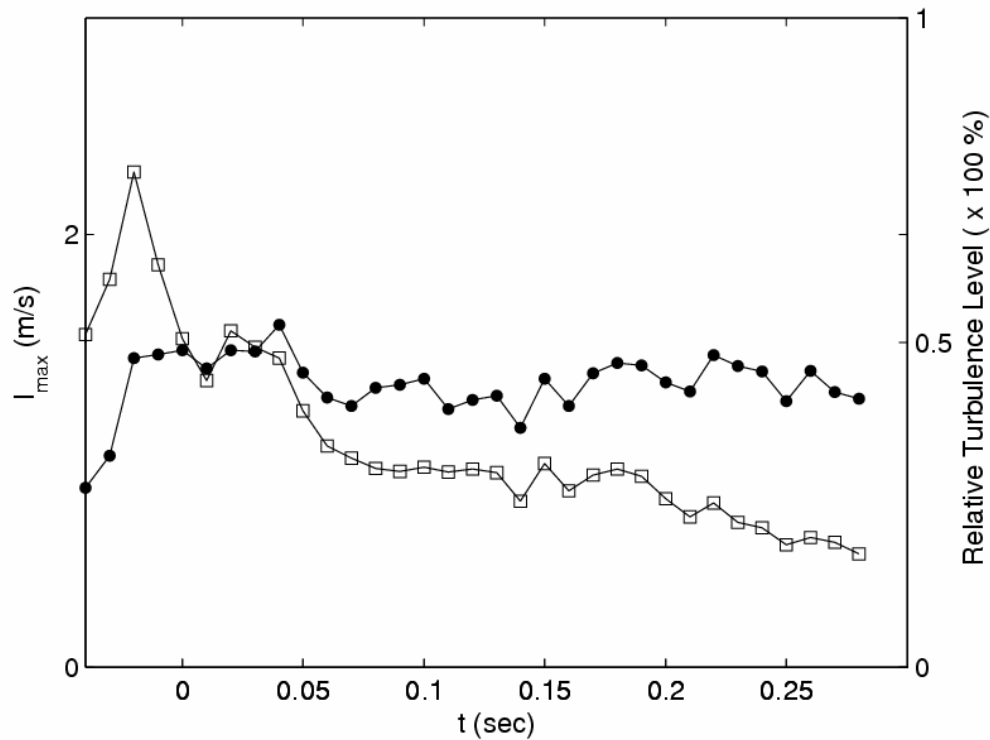


Fig. 4.8. Maximum turbulence intensity and relative turbulence level. \square : I_{max} (m/s),
 \bullet : $I_{max} / \langle UU + WW \rangle_{max}^{1/2}$.

4.6 Vertical run-up

The distributions of the maximum vertical velocities and the locations where the velocity occur are presented in Fig. 4.9. Splashing water occurred when a large wave slams on the front wall of the structure and moves upward, creating significant vertical momentum. Since offshore structures such as TLP and SPAR have deck and deck facilities installed above the floating column and intruding outward from the column, it may be important to estimate the vertical momentum of splashing water impacting

vertically normal to the deck. Similarly to the concept of cross-sectional horizontal velocity, maximum vertical velocity at every level is plotted. Note that the deck is at $z = 110$ mm in the figure. The measured maximum vertical velocity is surprisingly large. It reached 5.65 m/s, occurred at $t = -0.04$ s (corresponding to Fig. 4.6 (a)). That is the instant after the wave impinged on the structure and moved upward but not yet reached the top of the deck and developed a visible horizontal velocity. This maximum vertical velocity is about $2.90C$, and comparing with the maximum horizontal velocity of $1.13C$, is about 2.6 times the maximum horizontal velocity occurred over entire green water process. This velocity could develop into a huge vertical load to a structure if the deck or a portion of the structure stretches out from the vertical front wall.

The magnitude of the largest vertical velocity was reduced from the moment shown in Fig. 4.6 (a), which is found by examining velocities in subsequent velocity fields. Even though after Fig. 4.6 (b) the front of the upward splashing water is out of the FOV, we expect the maximum vertical velocity to continue to drop due to gravity and the development of the horizontal momentum. Since we did not measure the entire flow field covering the vertically splashing water due to the limit of the FOV, the maximum velocity at a given moment would not be possible to obtain. However, what we are interested is the maximum velocity near the elevation of the deck because this is more related to the stability of the deck and its structure. As shown in the consecutive plots in Fig. 4.9, the maximum vertical velocities occurred in front of the deck at $x < 0$ before the moment of $t = 0.00$ s (corresponding to Fig. 4.9 (c)). After the instant of $t = 0.00$ s, the location of the maximum vertical velocity move onto the deck.

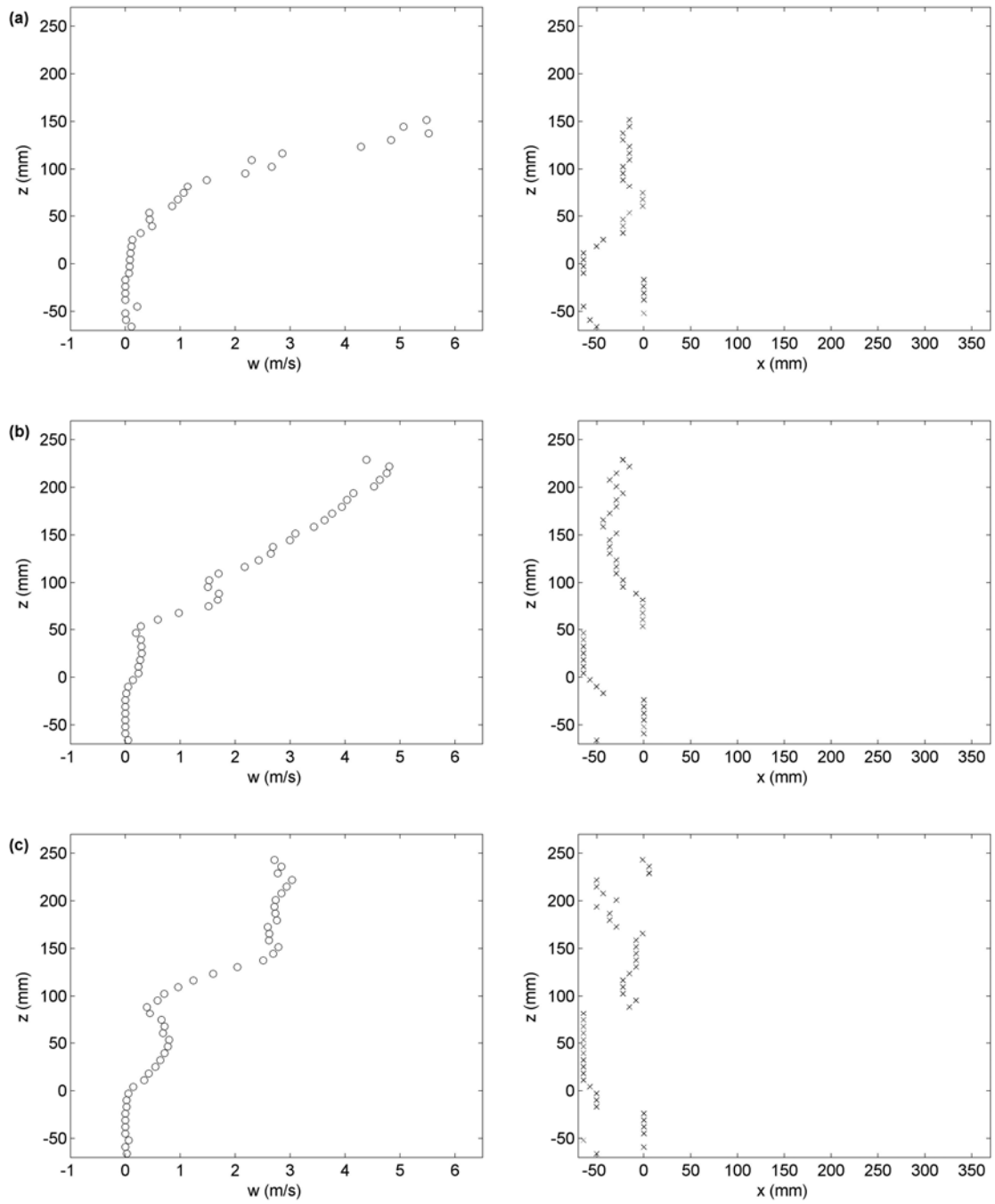


Fig. 4.9. Measured maximum vertical velocities and locations along the z axis at $t =$ (a) - 0.04 s, (b) -0.02 s, (c) 0.00 s, (d) 0.02 s, (e) 0.04 s, (f) 0.06 s, (g) 0.08 s, (h) 0.10 s, and (i) 0.12s.

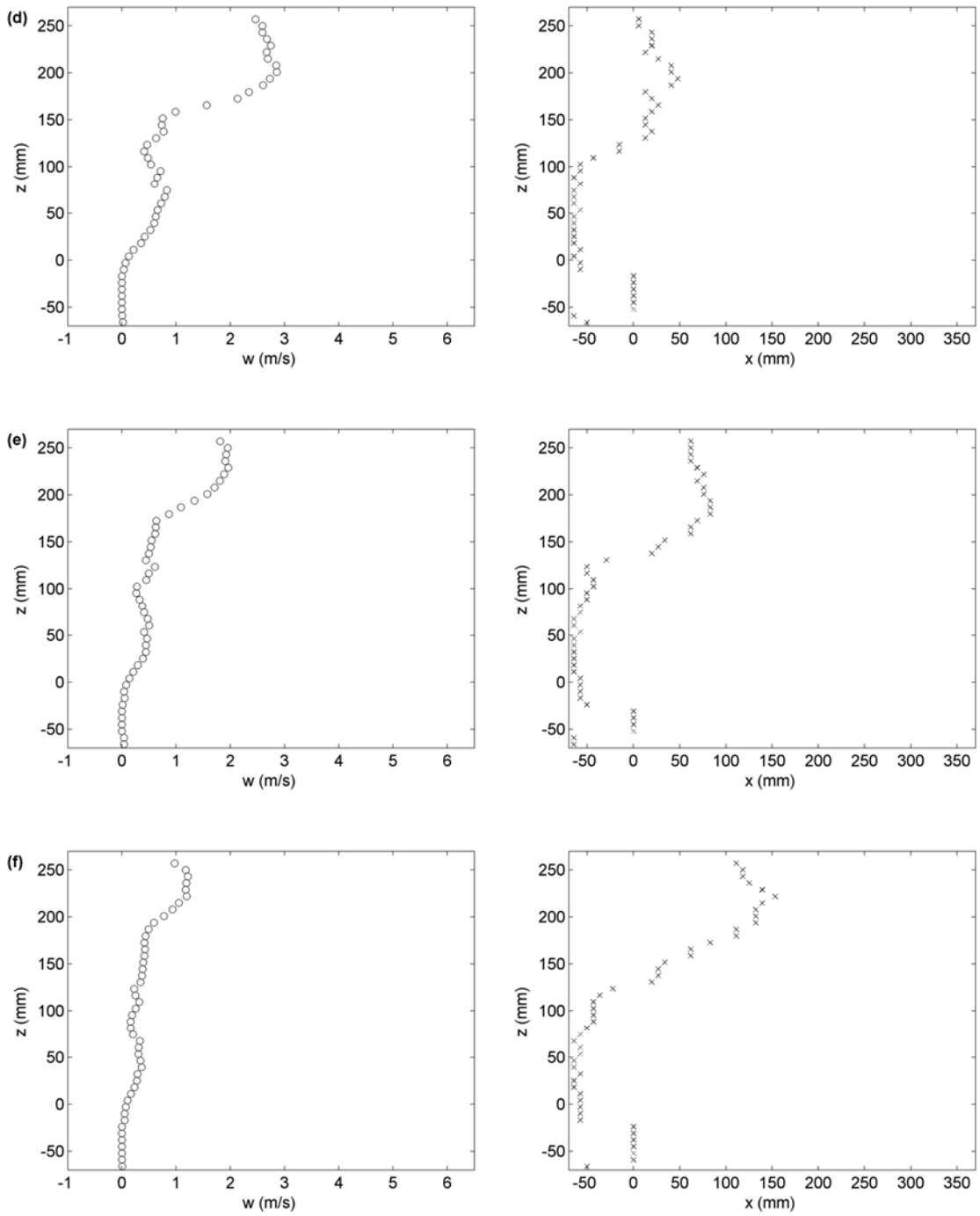


Fig. 4.9 (continued)

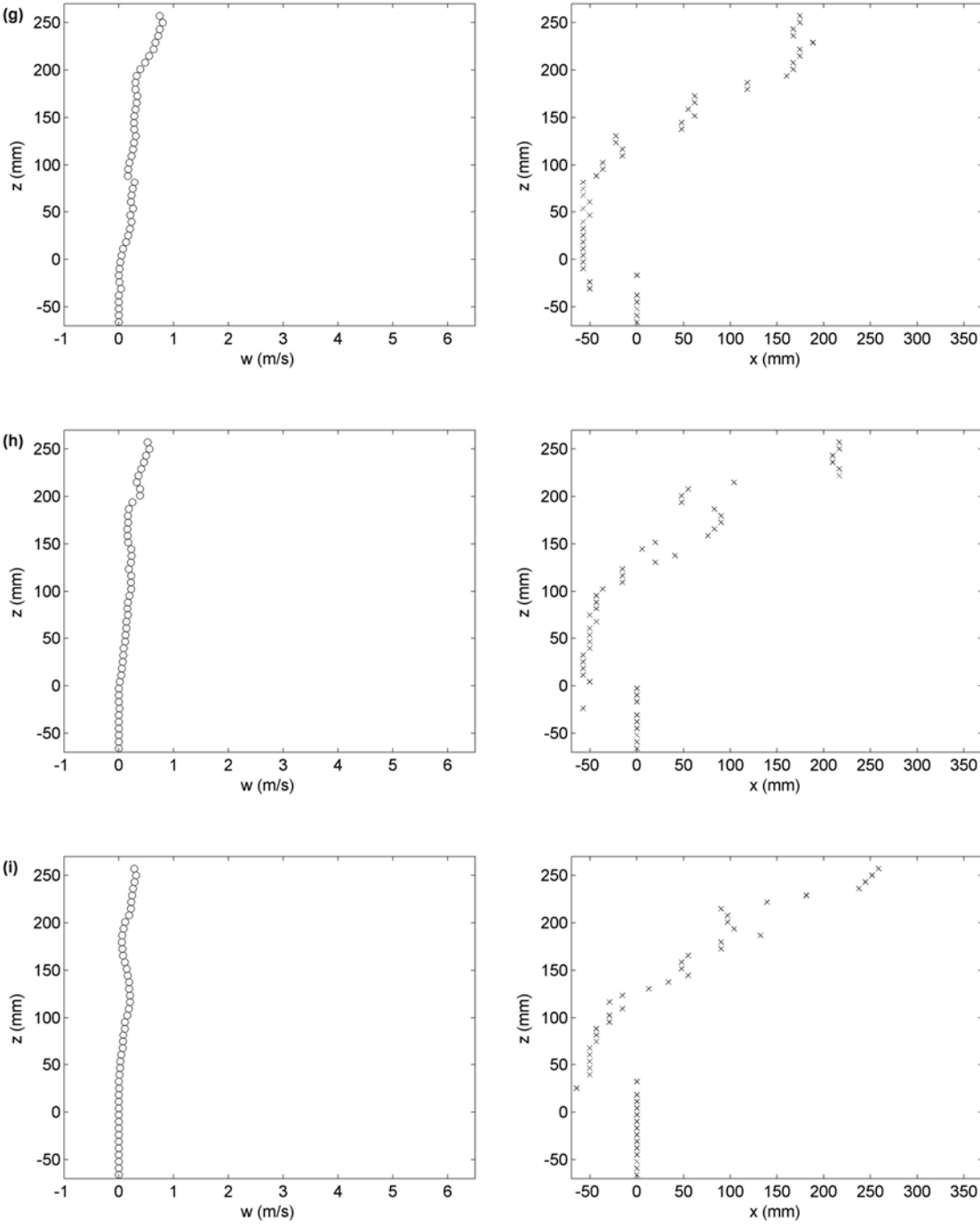


Fig. 4.9 (continued)

The magnitude reached almost 3 m/s ($\approx 1.5C$) at the very beginning of the green water process in Fig. 4.9 (d). The magnitude reduced while the location shifted downstream as the green water was on the deck and moving downstream. However, the vertical velocity can not be ignored because it posts a large upward vertical load to equipment and facility on the deck and close to the frontal edge of the deck. The corresponding velocity field in Fig. 4.6 will help visualizing the effect.

In Fig. 4.9, the maximum magnitude of the vertical runup velocity occurred at $t = -0.04$ s when the runup process starts. Based on the results in Fig. 4.9, we can not say the maximum is the largest vertical velocity of the process even for regions in the FOV in this study since the distribution starts from the maximum in the figure. In order to clarify the point, there is a need to analyze more detailed time steps which means earlier time steps and smaller time difference other than the distribution of Fig. 4.9. The present study analyzed extra velocity fields from earlier time step of $t = -0.058$ s with smaller time difference of 0.002 s between two consecutive velocity maps. Fig. 4.10 shows the distribution of vertical velocities along the wall from $t = -0.058$ to -0.04 s including the instants of Figs. 4.9 (a) and (b). Note that the velocity field is of phase averaged velocity using 10 instantaneous velocity measurements. Since the analysis for the turbulence will not be performed in the chapter, smaller number of instantaneous velocities was used for the phase average. The time difference between two successive plots in the figure is 0.002 s. The distribution of vertical velocities from $t = -0.058$ to -0.04 s verifies that the maximum velocity occurs between $t = -0.05$ and -0.04 s. From the distributions, $t = -0.06$ s seems to be around the instant when the plunging breaker

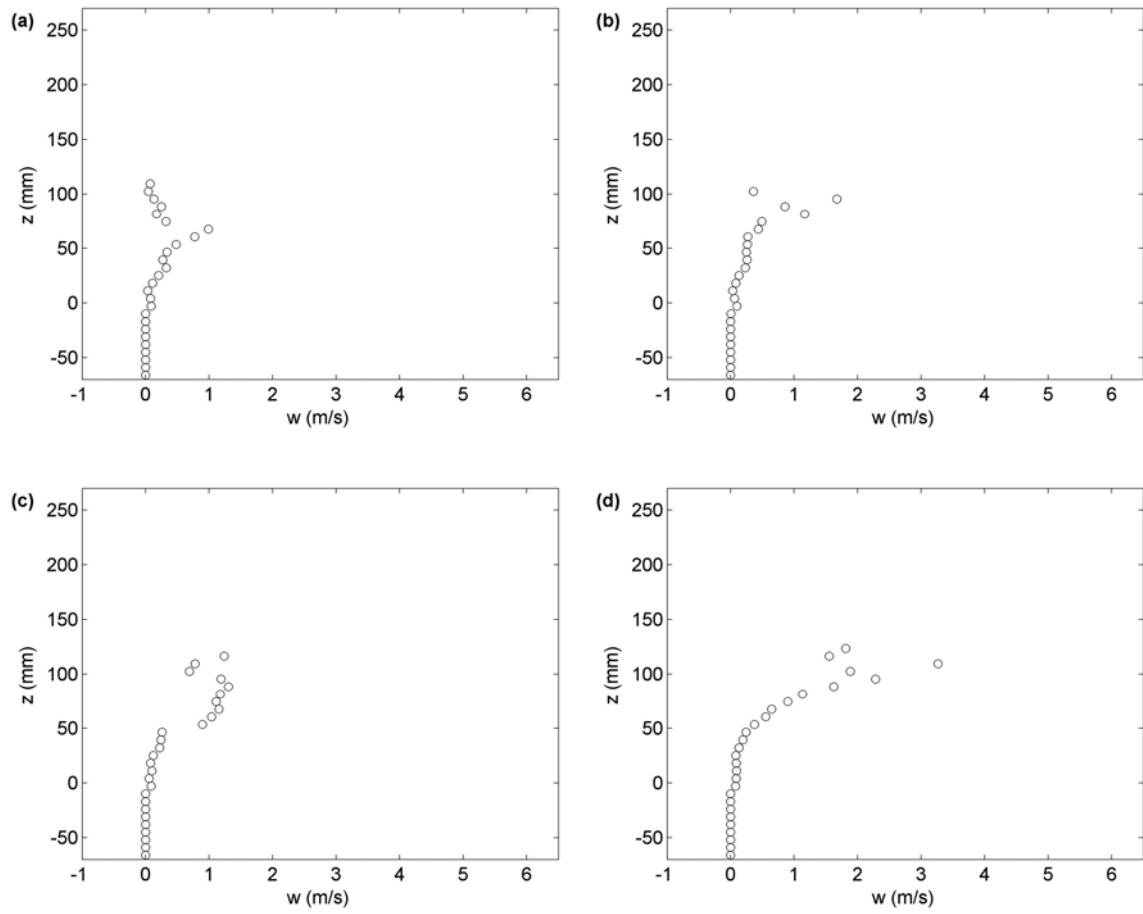


Fig. 4.10. Maximum vertical velocities along the z axis near impingement at $t =$ (a) - 0.058 s, (b) -0.056 s, (c) -0.054 s, (d) -0.052 s, (e) -0.050 s, (f) -0.048 s, (g) -0.046 s, (h)- 0.044 s, (i) -0.042 s, and (j) -0.040 s.

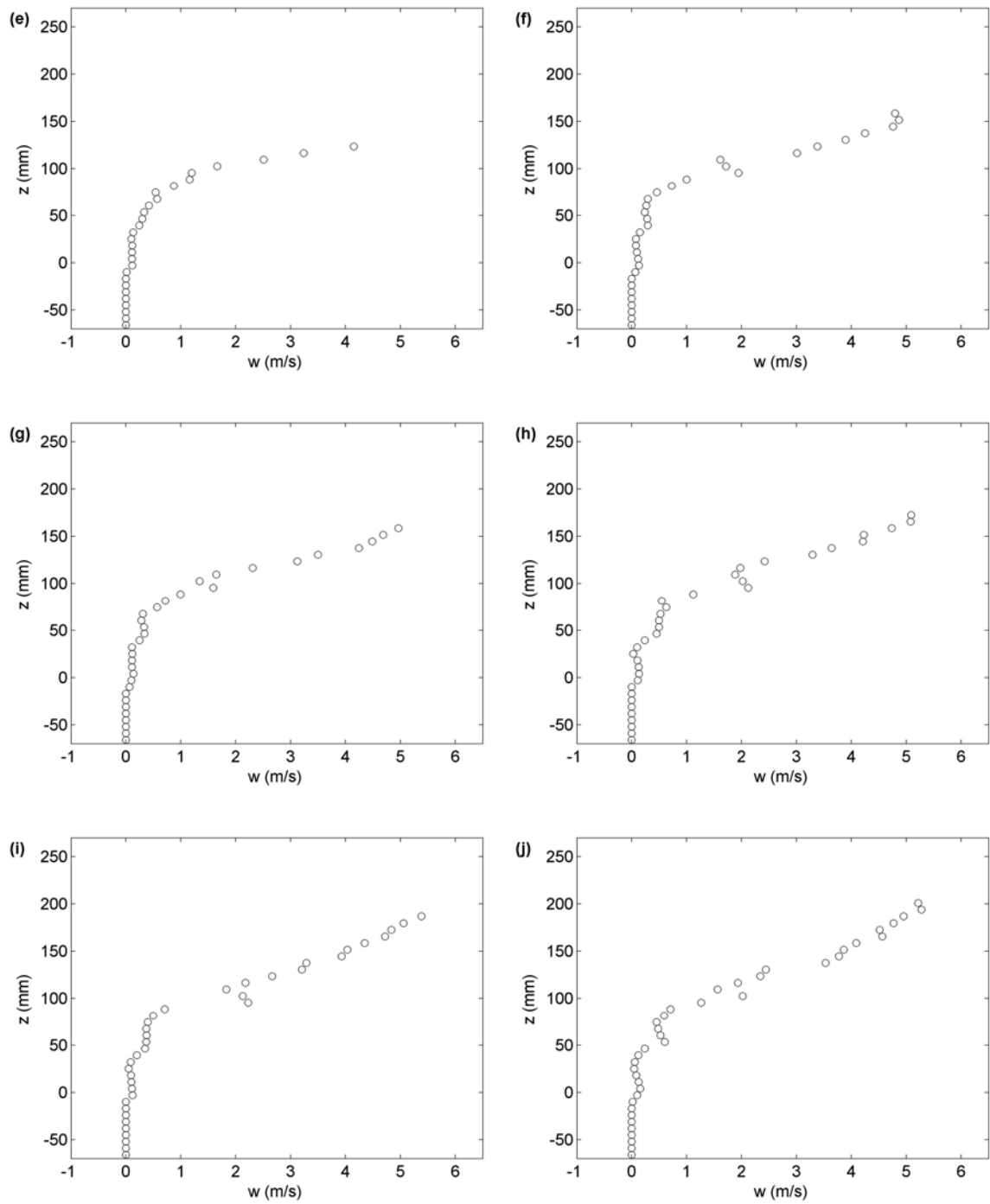


Fig. 4.10 (continued)

impinges because the magnitude is very small and after the moment, vertical velocity increases at a very fast rate.

4.7 Green water velocity distribution and dimensional analysis: cross-sectional velocity

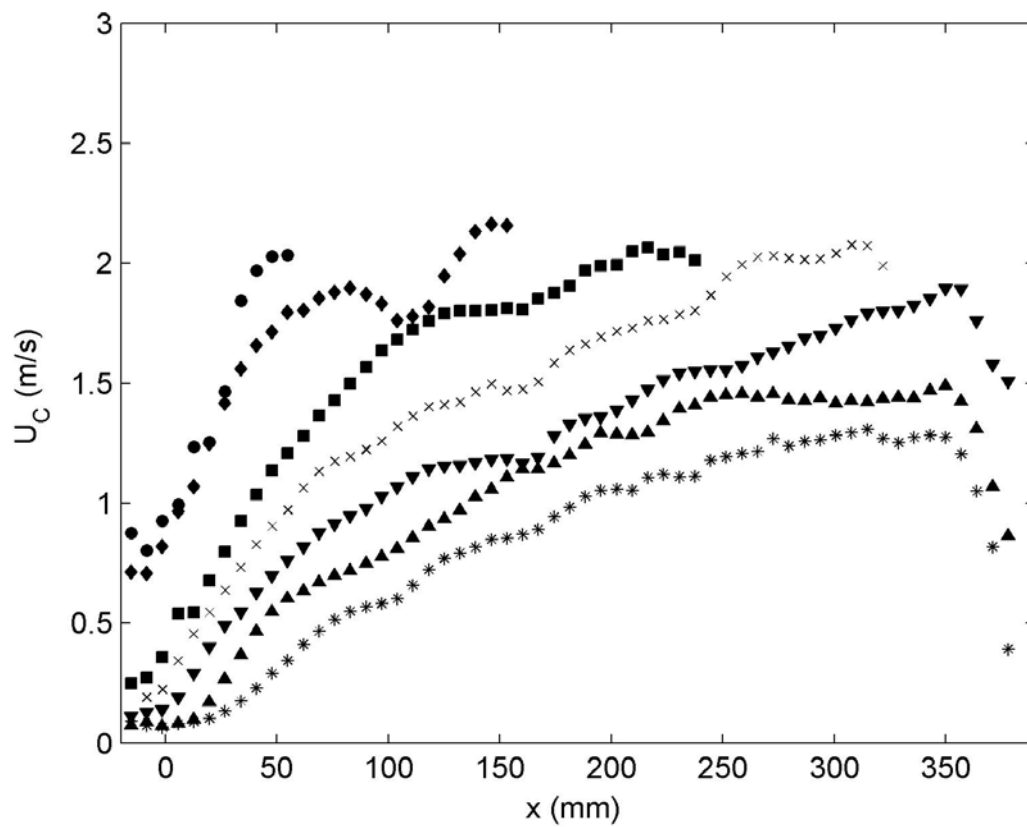


Fig. 4.11. Cross-sectional velocity at time; $t = 0.02$ s (\bullet), 0.06 s (\blacklozenge), 0.10 s (\blacksquare), 0.14 s (\times), 0.18 s (\blacktriangledown), 0.22 s (\blacktriangle), and 0.26 s ($*$).

The profiles of cross sectional velocity of green water corresponding to Fig. 4.6 are shown in Fig. 4.11. Velocity profile after $t = 0.02$ s is plotted since horizontal momentum of green water became dominant after this instant, whereas the horizontal velocity before this moment was relatively small. Cross sectional velocity, U_C , is defined as the maximum horizontal velocity at a cross section (a vertical column) on the deck. The figure includes seven velocity profiles with a time separation of 40 ms between the adjacent lines. The velocity profiles along the deck show a non-linear distribution. It also gives the speed of the front of the green water. As time increases, an asymptotic pattern started to show. At each time step, the largest velocity typically occurred near the front of the green wave while the smallest velocity at the leading edge of the deck, as shown in Fig. 4.11. Therefore, the front of the rushing green water is expected to exert a significant impact force to any facility and equipment on the deck as it slams to them.

The maximum horizontal velocity at each time step in Fig. 4.11 was almost constant until the wave front passed the end of the deck at $t = 0.16$ s. This indicates the front speed of green water is nearly constant. After the front of green water passed the end of the deck (i.e. at $t = 0.16$ s), the maximum horizontal velocity decreased at a rapid rate while the maximum velocity on the deck occurred at almost a fixed location about 2 cm to 3 cm from the end of the deck (the length of the deck is 37 cm). This is because when the front of green water moved downward after passing the end of the deck the momentum becomes vertical, as shown in the velocity fields in Fig. 4.6. However, as pointed out earlier in the case with a short deck, it is difficult to extract physical

meanings of green water after $t = 0.16$ s when the front moved out of the deck. An extended deck length as the case studied here is therefore needed to analyze the green water effect.

In order to understand the physical process in the proposed problem using the measurements, dimensional analysis is performed. The variables of interest are

$$U_C = f(x, t, h, U_M, C, g, T) \quad (4.4)$$

where x is the downstream distance from the deck leading edge, t time, h the water level on the deck, U_C the cross-sectional horizontal velocity, U_M the maximum horizontal velocity at a given time t , C the phase speed, g the gravitational acceleration, and T the wave period. By dimensional analysis, the obtained non-dimensional parameters are

$$\frac{U_C}{U_M} = \phi \left(\frac{x}{Ct}, \frac{h}{x}, \frac{t}{T}, \frac{U_M}{C}, \frac{U_C}{\sqrt{gh}} \right) \quad (4.5)$$

Note that the fluid viscosity is neglected because of a large Reynolds number in the experiments.

Fig. 4.12 shows the similarity profile among the three non-dimensional parameters, U_C/U_M , x/Ct , and t/T , that are the cross sectional horizontal velocity, downstream distance on the deck, and time. If directly plotting U_C/U_M versus x/Ct , the normalized velocity profile against the non-dimensional distance decayed at a fast rate. Based on the fact that the relationship between U_C/U_M and x/Ct could also depend on time, the non-dimensional time t/T with a constant b , was added to U_C/U_M to seek possible similarity. The constant b is to adjust the change rate of t/T . The velocity profiles along the deck plotted in Fig. 4.12 are from the instant the wave ran up onto the

deck with a significant horizontal momentum until the instant the front of green water reached the end of the deck, i.e., from $t = 0.02$ s to 0.15 s. During this period, the cross-sectional velocity, U_C , is normalized by the largest velocity measured at each time step, U_M . After $t > 0.15$ s, we apply the same approach by normalizing with the largest velocity on the deck, even though the front of green water has passed the deck.

In Fig. 4.13, the maximum velocity U_M is plotted against time t . It is clear that U_M decreased rapidly after the front of green water passed the end of the deck at $t = 0.15$ s. However, it is very interesting to see that U_M is nearly constant during the entire period when the front of green water is on the deck, from $t = 0.02$ s to 0.15 s. The maximum velocity indeed fluctuates and tend to decreases slightly as time increases before $t = 0.15$ s. After that moment, the maximum velocity decreases rapidly. The value of U_M can be fitted linearly with a nearly zero slope as

$$U_M = -0.23t + 2.20 \quad \text{for } t < 0.15 \text{ s} \quad (4.6)$$

in which the unit of U_M is m/s and the unit of t is seconds. Since the dependence of the maximum horizontal velocity on time is insignificant, we can treat it as constant. Therefore, the value of U_M is close to 2.20 m/s, that is, approximately $1.13C$, i.e., $U_M \approx 1.13C$. In Fig. 4.12, the results display a good similarity over that period. Using least square regression to fit the curve $U_C/U_M + b(t/T) = a(x/Ct)^n$ to the data, we obtained the following coefficients: $a = 1.02$, $b = 1.20$, and $n = 0.34$. The similarity

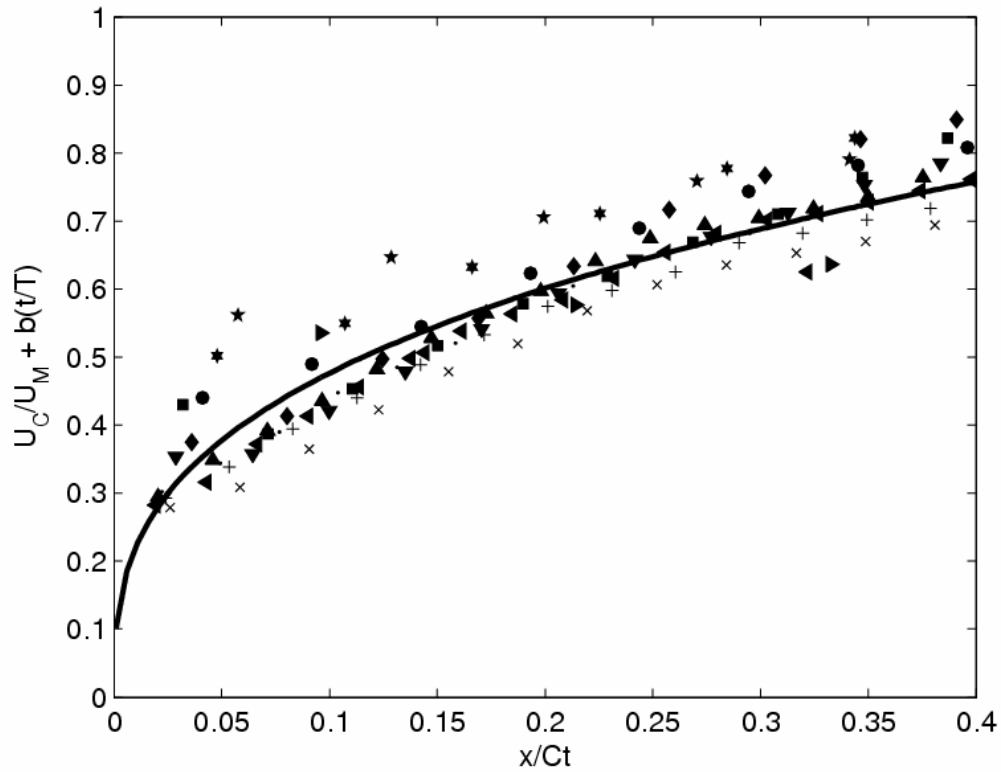


Fig. 4.12. Similarity profile obtained using the non-dimensional velocity, time and distance at $t = 0.02(\bullet)$, $0.03(\blacklozenge)$, $0.04(\blacksquare)$, $0.05(*)$, $0.06(\star)$, $0.07(\blackstar)$, $0.08(\blacktriangledown)$, $0.09(\times)$, $0.10(+)$, $0.11(\circ)$, $0.12(\blacktriangle)$, $0.13(\blacktriangleleft)$, $0.14(*)$, and $0.15(\blacktriangleright)$ s. Solid line is the fitting curve using least square regression.

curve in Fig. 4.12 can therefore be expressed as:

$$\frac{U_C}{U_M} + 1.20 \frac{t}{T} = 1.02 \left(\frac{x}{Ct} \right)^{0.34} \quad (4.7)$$

The R^2 value of the fit is 0.94.

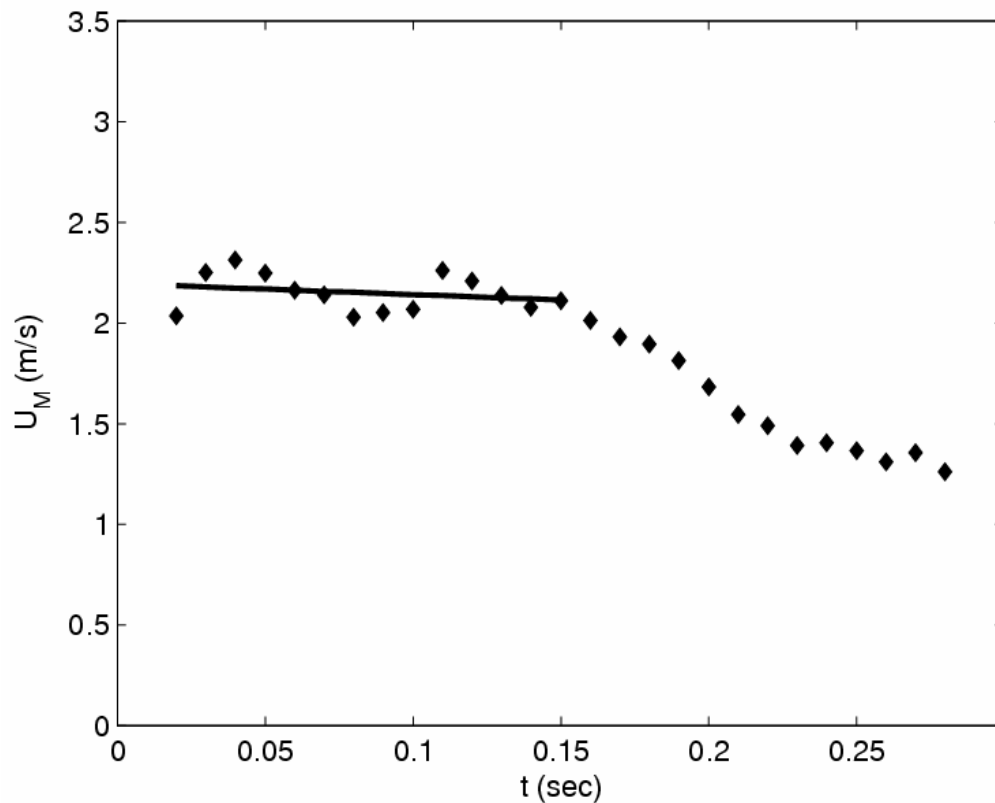


Fig. 4.13. Maximum horizontal velocity U_M against time t . Solid line: linear fit using data at $t \leq 0.15$ s.

Fig. 4.14 shows the location of the front of green water and the location of the maximum horizontal velocity, U_M , during the period when the front of the green water was on the deck. The figure shows U_M occurred very close to the front of green water. The locations of U_M and the front of green water are almost identical except that U_M was slightly behind when the front was approaching the end of the deck and the horizontal momentum was about to change to vertical. The location of the wave front as a function of time demonstrates a very linear behavior. Using linear regression a slope of

2.27 m/s was obtained. That means the front velocity of green water is constant as 2.27 m/s (1.16C), which is in agreement with the value of $U_M = 2.20$ m/s (1.13C) before $t = 0.15$ s.

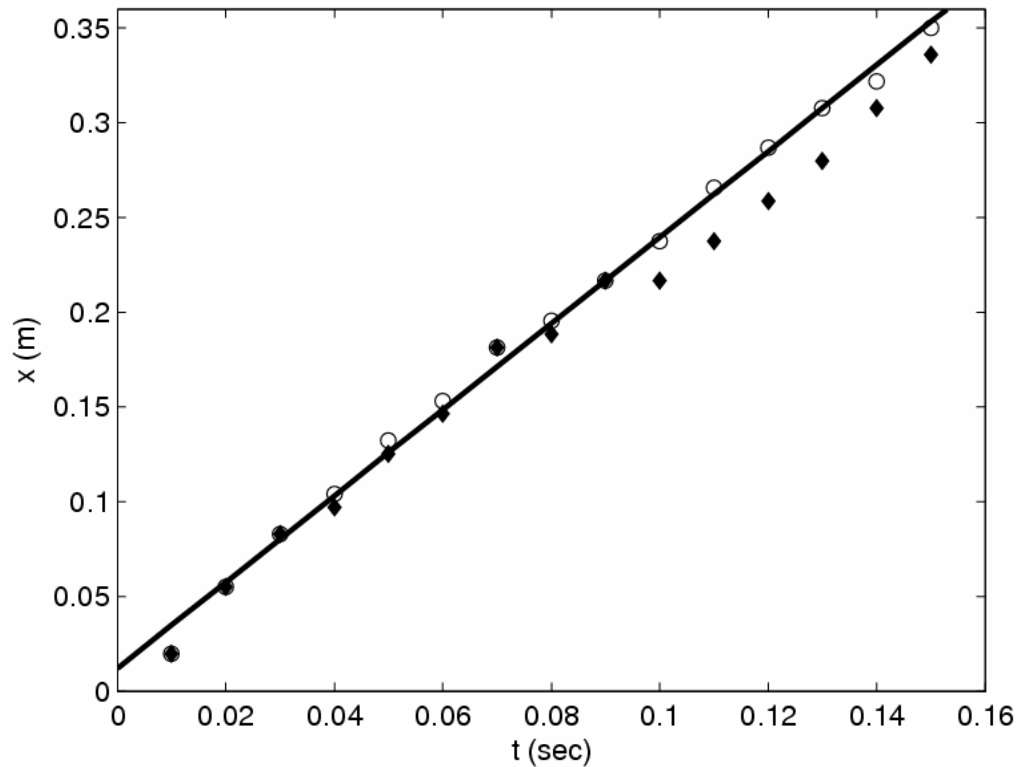


Fig. 4.14. Locations of wave front and maximum horizontal velocity (U_M). “o”, wave front; “◆”, U_M ; solid line, curve fitting of wave front.

From Fig. 4.11 we could see the velocity on the deck varied as a function of the location and time. A prediction equation is thus proposed to model the velocity profile on top of the deck as a function of time and space. From Eq. (4.6) and Fig. 4.13, the maximum velocity U_M at each time step is approximately constant and close to the front

velocity of green water. We hereafter use the average value of the front velocity and the maximum horizontal velocity to represent U_M to simplify the prediction equation, i.e., $U_M = 1.15C$. Based on a constant U_M and following the similarity profile represented by Fig. 4.12 and Eq. (4.7), a prediction equation for the cross-sectional green water velocity, U_C , along the deck is

$$U_C = U_M \left[1.02 \left(\frac{x}{Ct} \right)^{0.34} - 1.20 \frac{t}{T} \right] \quad \text{for } U_C \leq U_M \quad (4.8)$$

$$U_M = 1.15C$$

Eq. (4.8) is the prediction equation for green water on the deck. Note that this equation based on the similarity profile found from the experimental data (shown in Fig. 4.12). Eq. (4.8) is valid from the moment when water rushes onto the deck and momentum changes from primarily vertical to primarily horizontal to the moment when the front of green water falls back to the ocean at the end of the deck. The period is the one covered by the fitted lines in Figs. 4.13 and 4.14. After that period, U_C decreases rapidly, as implied in Fig. 4.13. However, we later found that Eq. (4.8) may be applied beyond the time when the front of green water reaches the trailing edge of the deck, i.e., $t > 0.15$ s, even though the equation was obtained from the similarity curve using the data when the front of the green water is on the deck (i.e. for $0.02 \text{ s} \leq t \leq 0.15 \text{ s}$). In this case it is assumed that after $t = 0.15$ s the same maximum velocity U_M is applicable as when the front of the green water is on the deck.

4.8 Depth averaged velocity of green water

We have analyzed the green water in terms of the cross-sectional velocity which is a largest velocity at a cross-section because a maximum magnitude is of importance in design. In this chapter, depth averaged velocity is presented to investigate a property representing a cross-section. Depth averaged horizontal velocity, U_D , along the deck can be obtained by integrating velocities vertically and dividing by water height on the deck as follows:

$$U_D = \frac{1}{h} \int_{h_l}^h U dz_d . \quad (4.9)$$

where h is the water height on the deck, h_l the lower free surface of the green water, and z_d the vertical coordinate with $z_d = 0$ being the elevation of the deck..

Fig. 4.15 shows the distribution of calculated depth averaged velocities before the green water passes the end of the deck. While depth averaged velocities show slightly smaller magnitude compared to the cross-sectional velocities, the distribution shows asymptotic pattern similar to that of cross-sectional velocities. As expected from the vertical profiles of green water velocities showing no significant gradient of the velocities against vertical direction, it is shown that there is slight difference in magnitude between those two velocity properties.

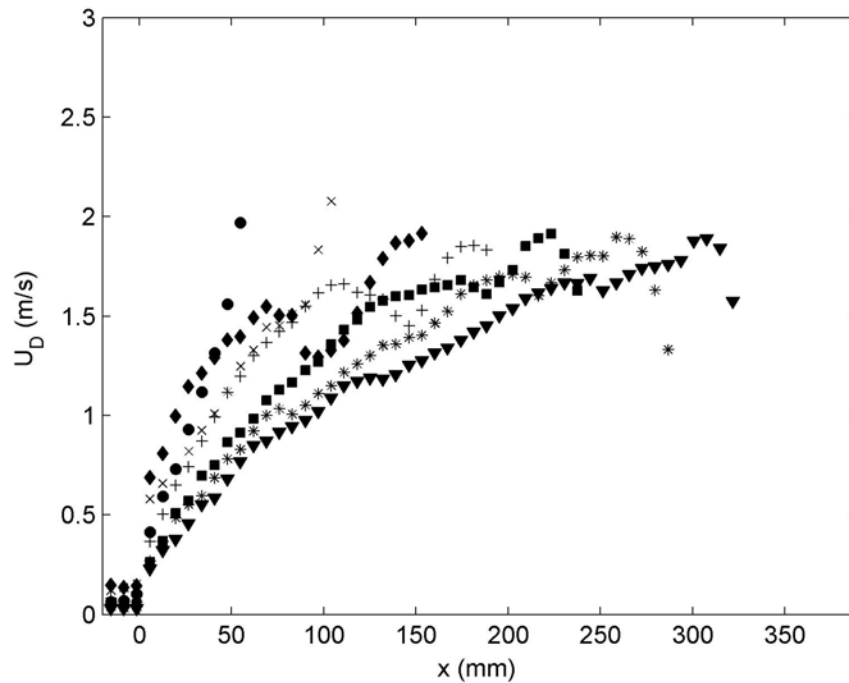


Fig. 4.15. Distribution of depth averaged green water velocity at $t = 0.02$ s (●), 0.04 s (◆), 0.06 s (×), 0.08 s (+), 0.10 s (■), 0.12 s (*), and 0.14 s (▼).

Fig. 4.16 shows maximum depth averaged velocities at a time. The maximum velocities of the green water were near 2.20 m/s as shown in the previous sections. Depth averaged velocities show a largest magnitude at a time near 1.9 m/s, which is close to the phase speed, 1.95 m/s. Maxima of the depth averaged velocities fluctuate right after the green water processed about $t = 0.05$ s and then show constant values until the green water passed the deck end ($t = 0.15$ s).

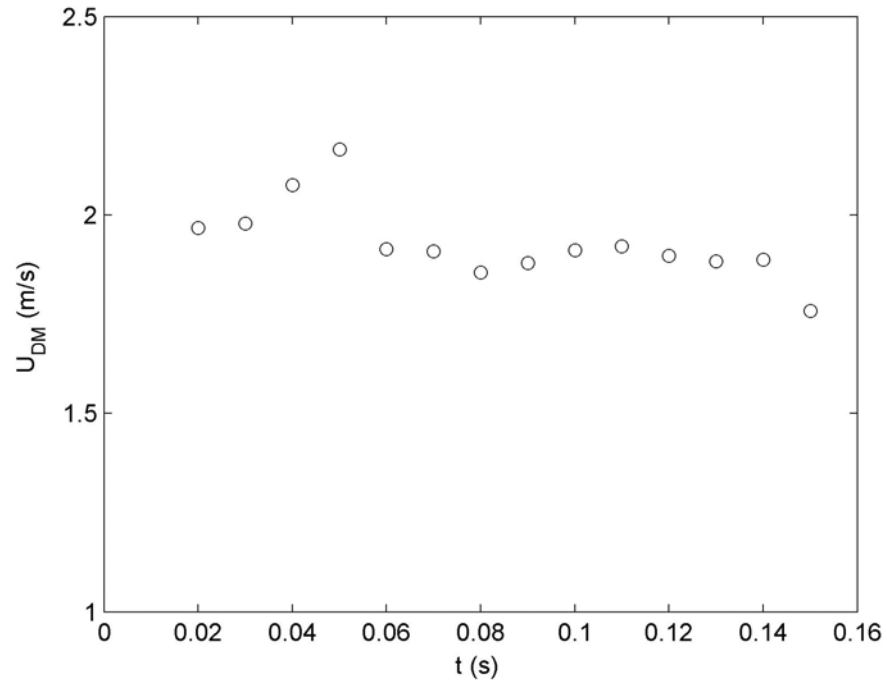


Fig. 4.16. Maximum depth averaged velocity at a time.

The same way as the non-dimensional analysis done for the cross-sectional velocities, the depth averaged velocities are also analyzed with the same non dimensional parameters except that the non dimensional cross-sectional velocity, U_C/U_M is replaced with the depth averaged velocity, U_D/U_{DM} . Fig. 4.17 shows relation between the non-dimensional parameters with switching the two non-dimensional velocities. The fitting curve is the plotting of modified Eq. (4.7) with replacing U_C/U_M with U_D/U_{DM} as follows:

$$\frac{U_D}{U_{DM}} + 1.20 \frac{t}{T} = 1.02 \left(\frac{x}{Ct} \right)^{0.34} \quad (4.10)$$

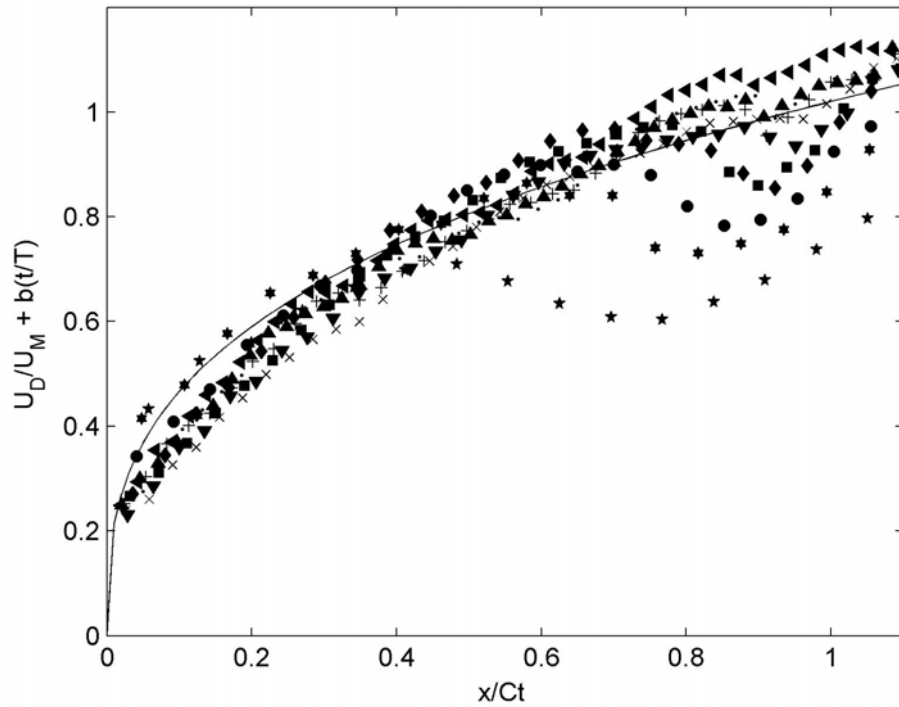


Fig. 4.17. Similarity profile of non-dimensional depth average velocity from $t = 0.02$ to 0.15 s. Solid line is a fitting curve.

The same coefficients in Eq. (4.7) were used in Eq. (4.10) to check resemblance in non dimensional distributions between two kinds of velocities. The fitting worked well as shown Fig. 4.17. Because U_{DM} is different from maximum velocity U_M in magnitude, the final equation for U_D will be different from Eq. (4.8). However, it is interesting that the cross sectional velocity and the depth averaged velocity distribute along the deck similarly showing difference of only 10 ~ 20% in magnitude ($U_M \approx 1.15U_{DM}$).

4.9 Extreme wave and green water in hurricane

The empirical model for green water velocity, Eq. (4.8), was used to predict the

characteristic green water velocity due to extreme waves in a severe hurricane. In September 2004, Hurricane Ivan, a category 5 hurricane, passed several wave gauges and buoys deployed by the Naval Research Laboratory (NRL) and National Data Buoy Center (NDBC) in the Gulf of Mexico. The maximum wave height, H_{max} , measured by a NDBC buoy reached 27.7 m (Wang et al., 2005). The model structure used in the present study is a 1:168 scale representation of a TLP with an extension deck (so it could be used to mimic a FPSO). The laboratory generated breaking wave had a height $H = 17.1$ cm, period $T = 1.30$ s, and phase speed $C = 1.95$ m/s in 0.80 m water depth. By Froude scaling, the 1:168 scale laboratory generated wave is equivalent to a maximum individual full scale wave height of 28.6 m, which is close to the H_{max} of 27.7 m measured by the NDBC buoy. The full scale equivalent wave period is 16.8 s and phase speed is 91 km/hour. Note that the equivalent wave period is close to the measured and hindcast wave spectra, which showed T_p in the 16+ s range.

Applying the empirical model, on the deck the measured maximum horizontal velocity is near the front of the green water. This maximum horizontal velocity has a magnitude close to $1.15C$, equivalent to 104 km/hour in the field. In addition, the vertical velocity right before the green water rushed onto the deck reaches $2.90C$. This velocity is surprisingly large, equivalent to 264 km/hour in the field (comparable to a Category 5 hurricane wind speed). The magnitudes of the maximum horizontal and vertical velocities help to explain why objects mounted on the deck or on the vertical face of the column are susceptible to damage under green water loading. Although there is no field data available on green water velocity to validate our prediction, the

prediction may be useful to shed some light on what may have happened on some platforms during the hurricane.

4.10 Conclusion

Measurements of the velocity field of a plunging breaking wave impinging on a model structure and associated green water on top of the structure were performed using two modern image based techniques – particle image velocimetry (PIV) and bubble image velocimetry (BIV). Before the wave impinged on the structure, the flow was horizontally dominant with a maximum horizontal velocity of $1.5C$, where C is the peak frequency related wave phase speed. The result is consistent with many other experimental studies on kinematics of breaking waves. Immediately after the impingement of the breaking wave on the front wall but prior to flowing onto the deck, the vertical velocity of the run-up was extremely large, reaching a maximum value of $2.9C$. After the wave passed the leading edge of the structure, the water momentum became horizontally dominant with a maximum horizontal velocity between $1.1C$ and $1.2C$ along the deck. This maximum velocity occurred near the front of the green water as it propagated over the deck until reaching the rear end of the deck. The dominant velocity and flow pattern at each phase is summarized in Fig. 4.18. The turbulence level of green water flow was between 40% and 50% of the maximum velocity at each given moment during the entire process starting with the initial vertical run-up.

A prediction equation (Eq. (4.8)) for the horizontal velocity distribution of green water along the deck was obtained by applying dimensional analysis to the measurement

data. This equation is valid during the entire green water process, from the front of the green water rushing onto the deck to the front of green water falling into the ocean at the rear end of the deck. Using the prediction equation to estimate green water impact during an extreme hurricane, such as Hurricane Ivan, indicates the maximum vertical water velocity in front of an offshore structure could reach 260 km/hour, while the maximum horizontal water velocity on the structure deck could reach 100 km/hour. With a turbulence level of 40% to 50%, these velocities could be much higher.

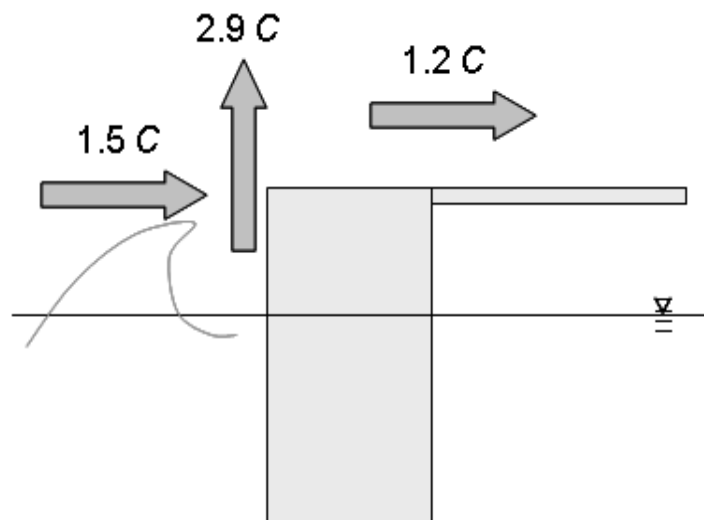


Fig. 4.18. Dominant velocities at different phases.

CHAPTER V

APPLICATION OF DAM-BREAK FLOW FOR GREEN WATER PREDICTION

5.1 Introduction

It has been known that the phenomenon of overtopping water on top of a structure may be similar to dam-break flows. Buchner (1995a) showed the resemblance of green water to a dam-break flow and commented that the application would be limited due to the shallow water assumption. Due to the possible similarity between green water and a dam-break flow, there have been many studies that applied the dam-break theory to green water studies. Fekken et al. (1999) simulated green water incidents using a Navier-Stokes solver with a volume-of-fluid method for free surface modeling. They modeled a dam-break flow to mimic the water flow on the deck without considering the ship-wave interaction and ship motion. Shoenberg and Rainey (2002) modeled the green water flow by simulating a moving shelf submerged into a pool of water using a potential flow theory and a boundary integral equation method. They compared their results with an analytical solution of dam-break flow and found a reduction in damage if using the moving shelf model. Yilmaz et al. (2003) developed a semi-analytical solution for a dam-break flow to simulate green water on a deck. They obtained the solution using the Fourier series analysis and Fourier transformation technique to describe the nonlinear dam-break problem.

In the typical design procedure for the green water load, the standard approach

to estimate the velocity from a green water incident is to use the dam-break solutions (Shoenberg and Rainey, 2002). The dam-break flow is a classic problem that has been investigated by numerous researchers. Many solutions were proposed in various cases of dam-break flow. Among the solutions, an analytical solution that has been widely used for a dry frictionless flat bed and considered as the simplest one is Ritter's solution (Lauber and Hager, 1997; Vischer and Hager, 1998; Zoppou and Roberts, 2003). That solution has been used for green water predictions (Buchner, 1995a, b; Shoenberg and Rainey, 2002). However, Lauber and Hager's (1997) experimental study indicated that the front velocity of a real dam-break flow reduces as a function of time, which disagrees with Ritter's solution of a constant front velocity. Even though many green water studies use the dam-break flow for velocity estimation, validation on the relation between the dam-break flow and green water flow has not yet been carefully proved.

In this chapter, a simple but widely used solution for a dam-break flow was examined with the determination of the initial water depth, which is considered the most important input for the solution. The initial water depth was determined using information obtained in the measurements. Since the dam-break solution gives one-dimensional velocity along downstream, the solution was compared with the measured cross-sectional velocity and vertical distributions of the horizontal velocities of the green water. Comparisons of the widely used linear dam-break solution are made with not only the measured green water velocity but also the prediction model suggested in the previous chapter.

5.2 Vertical distribution of horizontal velocity

The vertical distributions of horizontal velocities on the deck are shown in Fig. 5.1. At the instant of $t = 0.00$ s, the horizontal velocities are very small. That is because the vertical upward momentum of the runup is dominant at the moment. Note that z_d in the figure is another vertical coordinate with $z_d = 0$ being the elevation of the deck surface. After the instant, the momentum of overtopping wave starts to become horizontal. Once the green water is formed, the frontal area of the green water shows a relatively large magnitude of velocity at each time step. From the recorded images, it was seen that the green water impinges on the deck near $x = 200$ mm after the upward overtopping water changes its direction to horizontal. According to the vertical velocity distributions, before the impingement of the green water onto the deck surface, the maximum horizontal velocity occurs high above the deck surface. After the impingement, the green water near the deck surface (but not on the deck surface) shows a relatively larger magnitude of horizontal velocity. The green water progresses and moves downstream without changing its flow pattern. The vertical velocity distributions of green water do not show a significant gradient after the impingement. It indicates that the difference between the maximum velocity and the depth averaged velocity is insignificant.

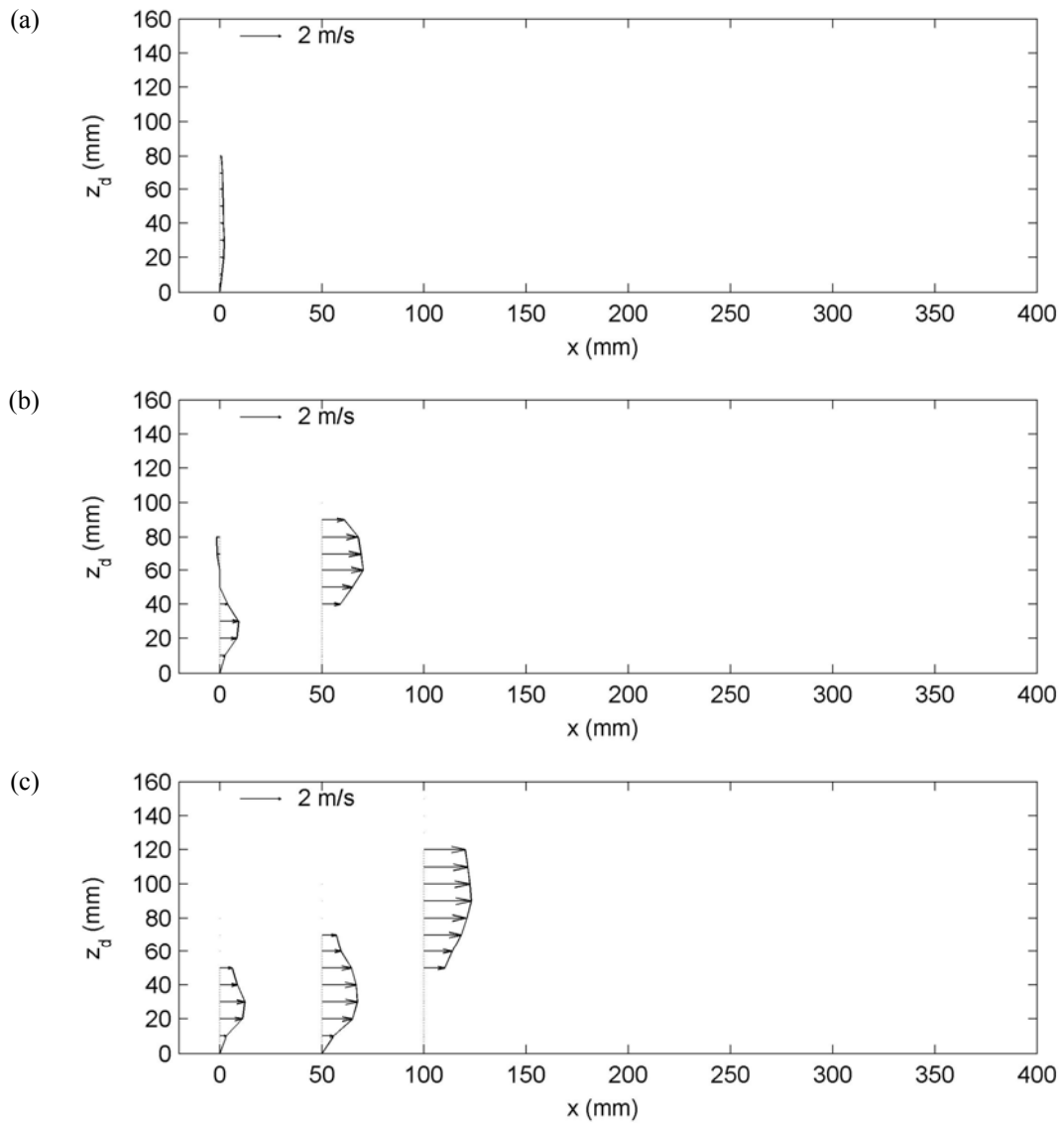


Fig. 5.1. Distributions of horizontal velocity of green water at $t =$ (a) 0.00 s, (b) 0.02 s, (c) 0.04 s, (d) 0.06 s, (e) 0.08 s, (f) 0.10 s, (g) 0.12 s, (h) 0.14 s, (i) 0.16 s, (j) 0.18 s, (k) 0.20 s, (l) 0.22 s, (m) 0.24 s, (n) 0.26 s, and (o) 0.28 s.

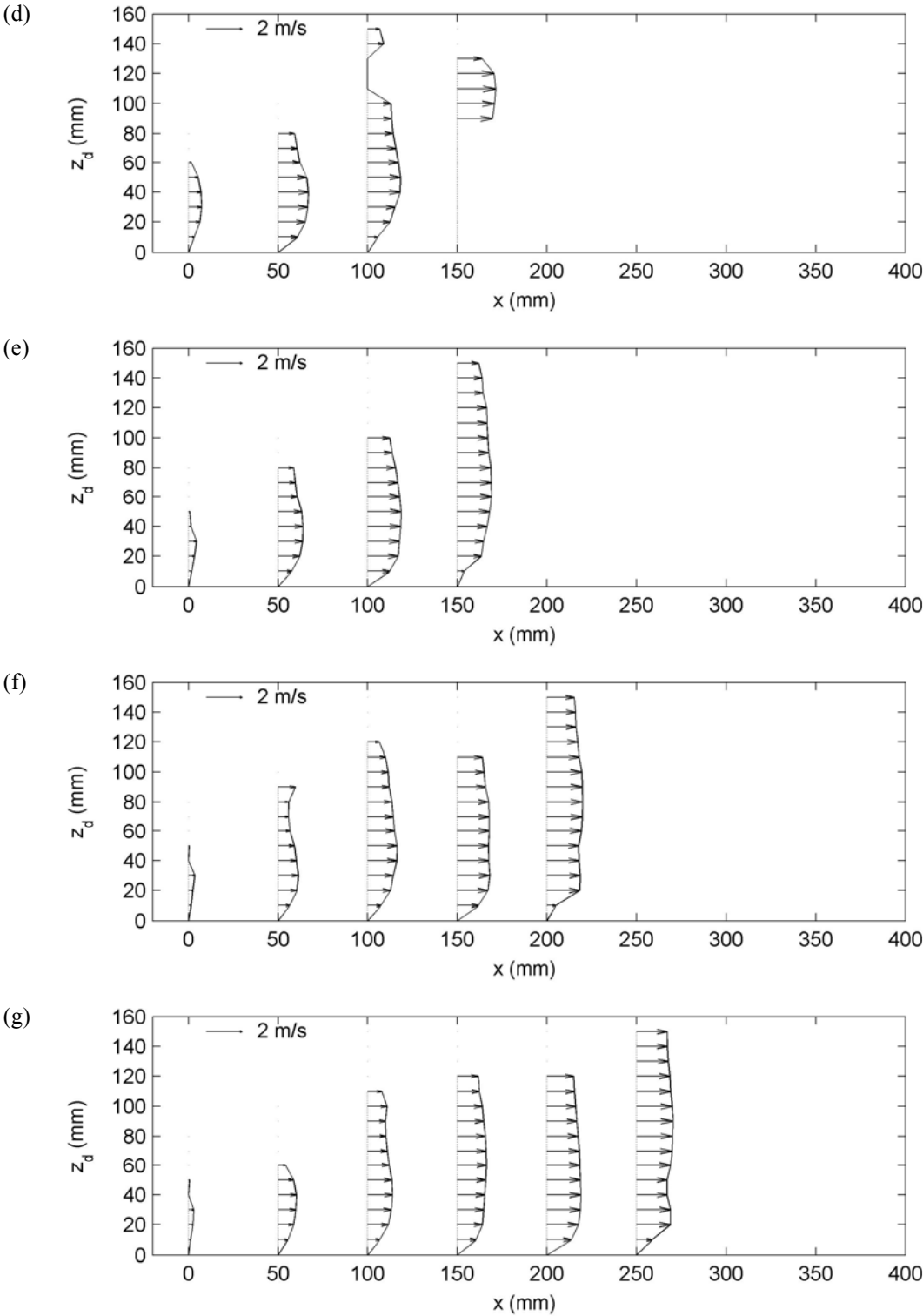


Fig. 5.1. (continued)

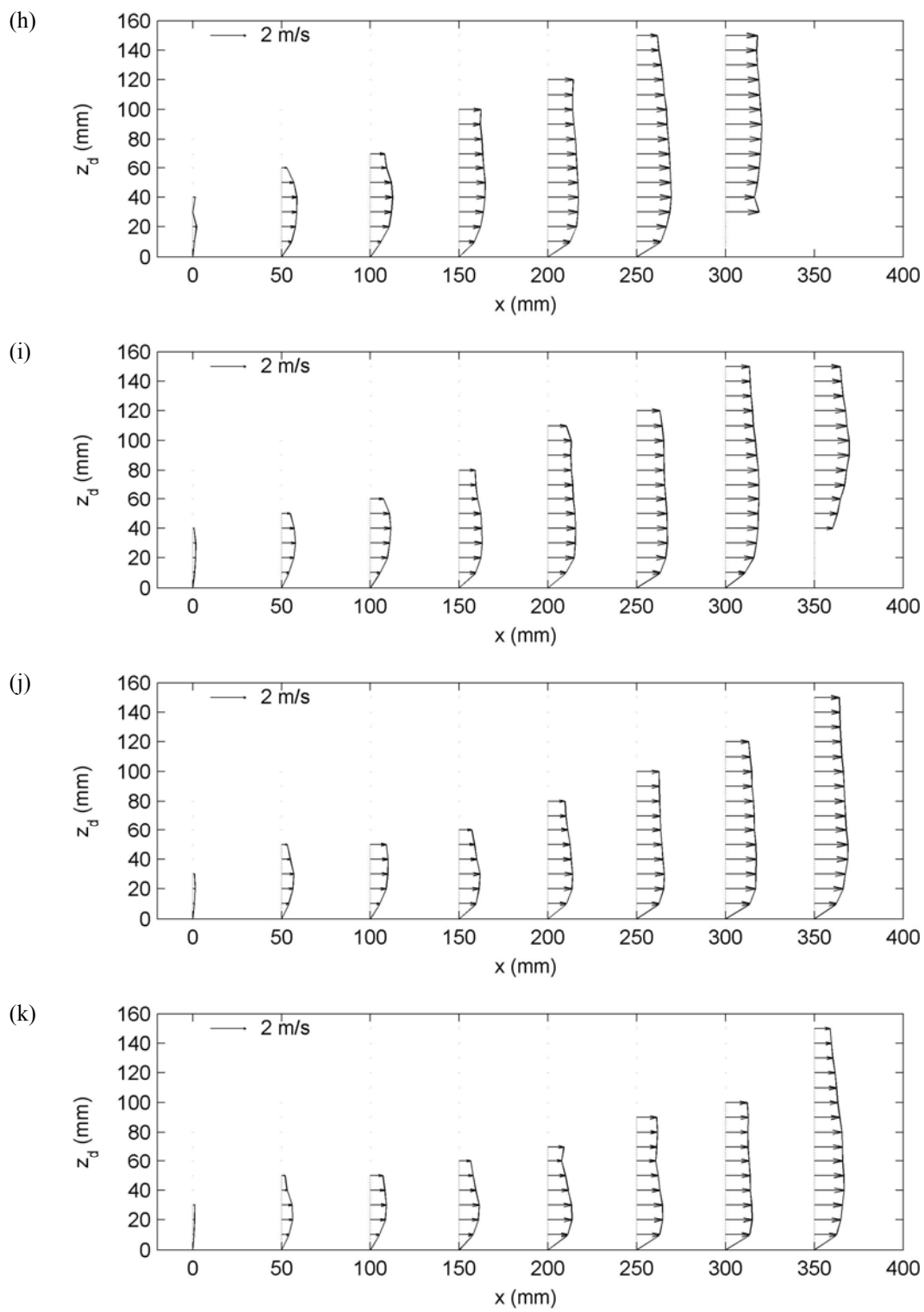


Fig. 5.1. (continued)

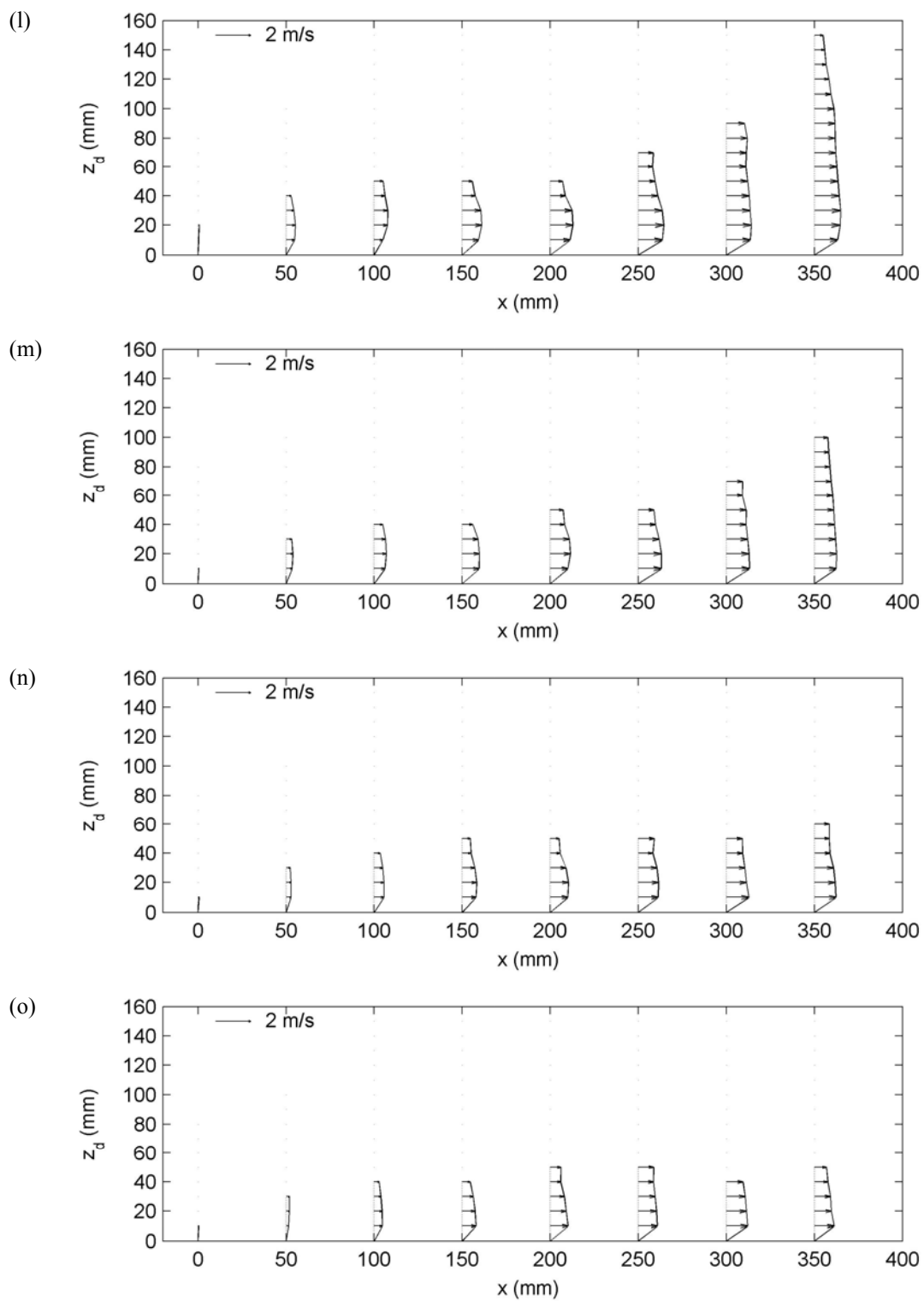


Fig. 5.1. (continued)

5.3 Dam-break model for green water prediction

The standard approach to estimate the velocity for a green water incident in a typical design in industry is to use the dam-break solutions (Shoenberg and Rainey, 2002). A dam-break flow is typically governed by the Saint Venant equations;

$$\begin{aligned} \frac{\partial h}{\partial t} + \frac{\partial(uh)}{\partial x} &= 0 \\ \frac{1}{g} \frac{\partial u}{\partial t} + \frac{\partial}{\partial x} \left(h + \frac{u^2}{2g} \right) &= S_0 - S_f \end{aligned} \quad (5.1)$$

where, h is the flow depth, u the horizontal velocity, g the gravitational acceleration, S_0 the bottom slope, and S_f the friction slope. The classic and widely used analytical solution of dam-break flow is Ritter's solution with the assumptions of the flow being one-dimensional with a uniform velocity distribution over the depth and hydraulic static pressure. Ritter's solution consists of two equations; one is for a water elevation and the other is for a horizontal velocity as follows;

$$\sqrt{\frac{g}{h}} = \frac{1}{3} \left(2\sqrt{gh_0} - \frac{x}{t} \right) \quad \text{for } -\sqrt{gh_0} < \frac{x}{t} < 2\sqrt{gh_0} \quad (5.2)$$

$$u = \frac{2}{3} \left(\sqrt{gh_0} + \frac{x}{t} \right) \quad \text{for } -\sqrt{gh_0} < \frac{x}{t} < 2\sqrt{gh_0} \quad (5.3)$$

where h_0 is the initial water depth of the reservoir. Velocity profile by Ritter's solution can be expressed by Eq. (5.3). The boundaries for x/t indicate the front velocity upstream (negative) and downstream (positive), respectively. By examining Eq. (5.3), it is seen that the velocity is strongly depend on h_0 , and the velocity is singular at $t \rightarrow 0$

(except at $x = 0$). The velocity along the downstream location increases linearly from the negative front to the positive front. In this study, the one-dimensional velocity obtained from the solution of the dam-break flow will be compared with the cross-sectional velocity.

5.4 Determination of initial water depth

Since the green water flow does not have a well-defined h_0 in Eq. (5.3) if the dam-break solution is to be applied, we need to estimate this crucial value. Two different approaches were used in the estimations. In the first approach, we assume perfect wave reflection at the deck to estimate the height of water above the free board of the deck. Under linear wave assumption, the free surface elevation of a perfectly reflected wave at the structure equals to the wave height of the incoming wave. The initial water depth can therefore be express as

$$h_0 = H - z_{deck} \quad (5.4)$$

in which H is the incoming wave height in deep water and z_{deck} is the free board elevation from the still water surface. The tested wave has a wave height of 17.0 cm in deep water, as shown in Fig. 2.3, and a free board of 11.0 cm. We therefore estimate the first initial depth $h_0 = 6.0$ cm.

In the second approach, we apply the finding in the previous chapter that the front velocity of the dam-break flow matches the front velocity of green water. With this we can back calculate h_0 using the measured front velocity of green water. The front velocity of green water is nearly constant and approximately equal to $1.16C$, which

was showed in Fig. 4.15. Since the front velocity of dam-break flow in Ritter's solution is $2\sqrt{gh_0}$, we let a relation of

$$V_{FG} = 2\sqrt{gh_0} \quad (5.5)$$

where V_{FG} is the front velocity of green water. The initial depth can thus be back calculated as

$$h_0 = \frac{V_{FG}^2}{4g} \quad (5.6)$$

Since $V_{FG} \approx 1.2C$ from the laboratory measurements, the initial depth can be rewritten as

$$h_0 = 0.36 \frac{C^2}{g} \quad (5.7)$$

in which C is the wave phase speed. Using Eq. (5.7) and the wave phase speed of 1.95 m/s in the experiments, h_0 is calculated as 14.0 cm. Note that this value is more than twice that obtained using Eq. (5.4).

5.5 Comparison of dam-break flow and green water flow

The comparison of cross-sectional velocities among the experimental data and Ritter's solution (Eq. (5.3)) with different h_0 is shown in Fig. 5.2. The prediction model (Eq. (4.8)) suggested in Chapter IV was also compared. Note that the end of the data and lines (with the maximum x value) in the figure indicates the location of the front of green water. Both h_0 values from Eqs. (5.4) and (5.7) are plotted for Ritter's solution in the figure. In addition to the determination of the initial water depth h_0 in

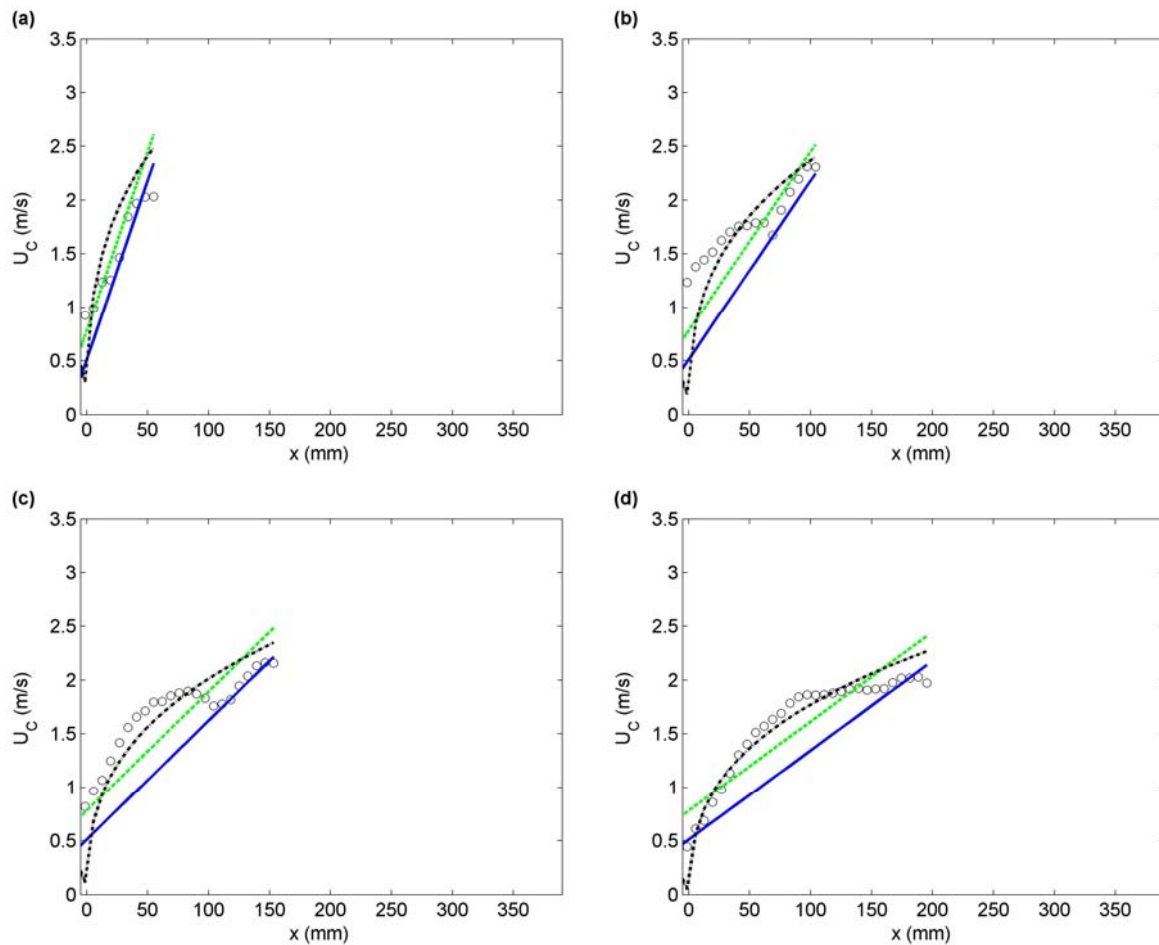


Fig. 5.2. Comparisons of cross-sectional horizontal velocity U_C along the deck among the experimental data (velocity measured using BIV and shown in Fig. 4.12), the prediction equation (Eq. (4.8)), and the analytical solution of dam break flow (Ritter's solution in Eq. (5.3)) at $t =$ (a) 0.02 s, (b) 0.04 s, (c) 0.06 s, (d) 0.08 s, (e) 0.10 s, (f) 0.12 s, (g) 0.14 s, (h) 0.16 s, (i) 0.18 s, (j) 0.20 s, (k) 0.22 s, and (l) 0.24 s. Solid line, Ritter's solution with $h_0 = 6.0$ cm (obtained using Eq. (5.4)); dashed line, Ritter's solution with $h_0 = 14.0$ cm (obtained using Eq. (5.7)); dashed-dotted line, prediction equation.

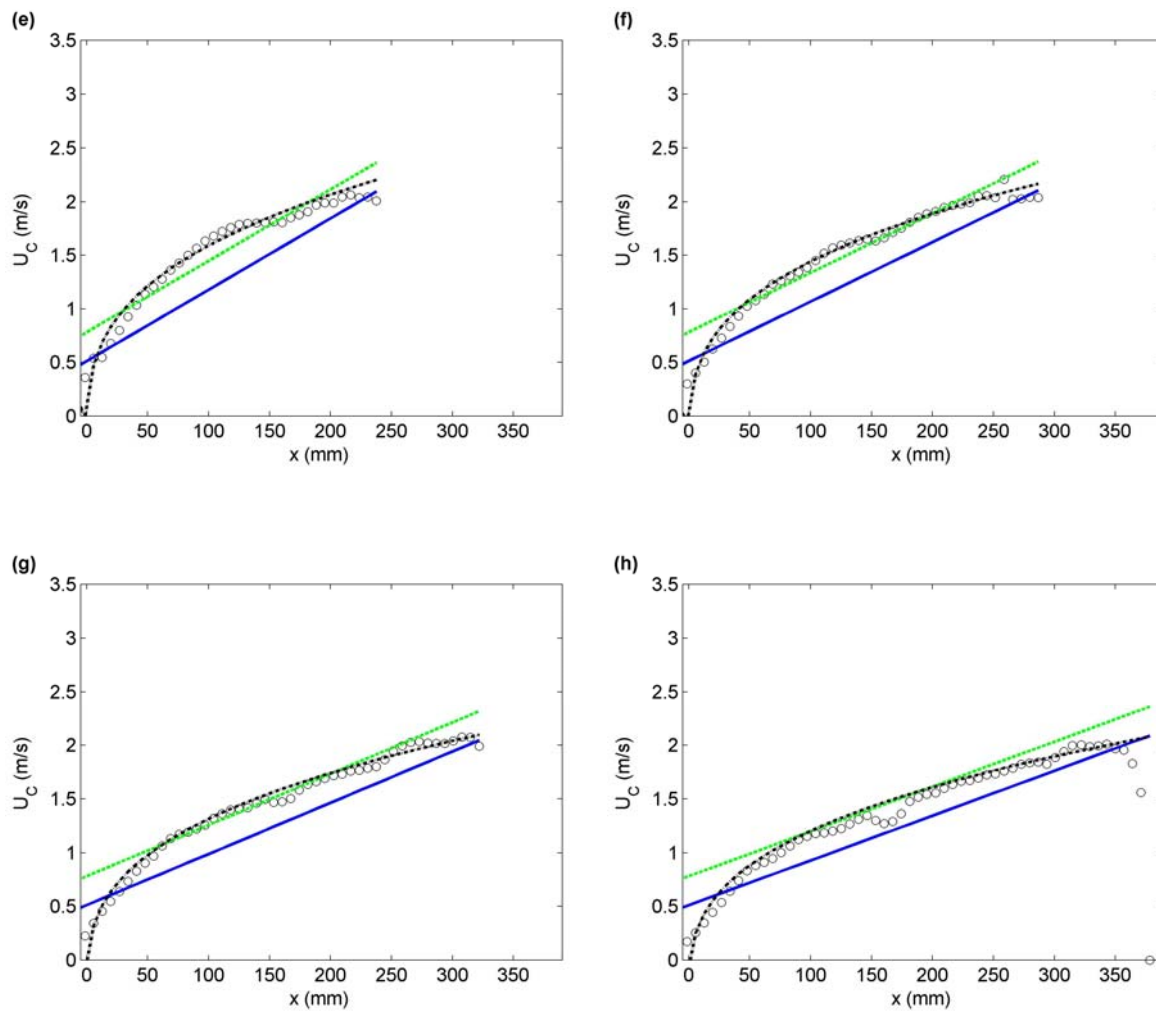


Fig. 5.2 (Continued)

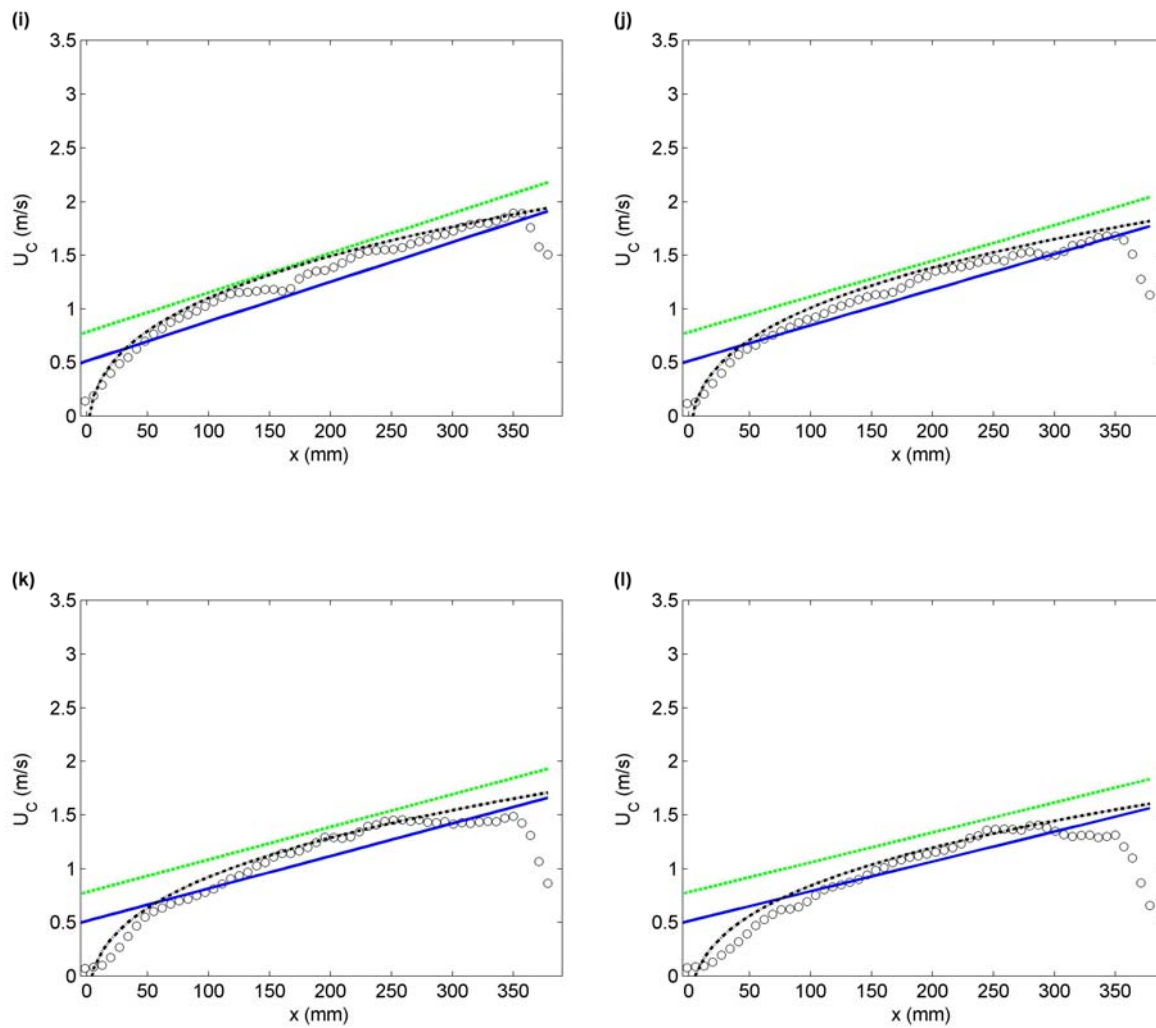


Fig. 5.2 (Continued)

Ritter's solution, it is also necessary to determine the instant when the green water process starts, corresponding to the instant of dam removal for the dam-break flow (i.e., $t = 0$). As explained earlier, $t = 0$ for the green water process throughout the present study represents the instant when the free surface of the wave overtopping the structure and across the leading edge of the structure (Figs. 4.5 (c) and 4.7 (c)). After $t = 0$, the wave momentum pushed the wave front to move forward onto the deck and momentum started to change to horizontal as shown in Figs. 4.5 (d) and 4.7 (d). In the present study, the dam-break solution uses the same time step as the green water process and was compared with the measurements.

From the comparison, we found that the result from the prediction model (Eq. (4.8)) agrees with the measured green water velocities very well at all the instants and locations except near the end of the deck where the water falling back into the ocean. On the other hand, Ritter's solution results in a linear line for the velocity prediction while the measurement data show otherwise. It seems that Ritter's solution under-predicts the green water velocity from the beginning until around $t = 0.14$ s (corresponding to Figs. 5.2 (a) to (g)), regardless which method was used for the h_0 determination. However, it does predict the front velocity of the green water reasonably well, especially the one using Eq. (5.7) for h_0 . Note that $t = 0.15$ s was the instant when the front of green water reached the end of the deck. This means the Ritter's solution under-predicts the green water velocity until the moment the front of the water reached the end of the deck. The comparison also shows that using Eq. (5.7) for h_0 estimation may give a better prediction of green water velocity if Ritter's solution is to be used.

After the front of green water passed the end of the deck (corresponding to Figs. 5.2 (h) to (l)), the result from the prediction model (Eq. (4.8)) again agrees very well with the measured data. Ritter's solution, however, either over-predicts the velocity, if Eq. (5.7) is used for h_0 , or under-predicts if Eq. (5.4) is used.

Overall, all three predictions result in a reasonable "engineering accuracy" in practical applications, while the present prediction model gives the best agreement, followed by Ritter's solution with Eq. (5.7) for h_0 . Although there are some discrepancies at certain time periods and regions and weakness in describing the non-linear behavior of the green water velocity, the prediction using Ritter's solution can be considered as competitive - giving the advantage of its simple form and universal recognition. Interestingly, Ritter's solution does not agree well with the experimental measurement of real dam-break flows in terms of velocity (Lauber, 1997). The main reason is that while the solution has a constant front velocity, the real flow does not. The measured front velocity in Lauber's study reaches the same constant front velocity as in the Ritter's solution only after a certain period after the dam is removed and the velocity decreases. On the contrary, the green water experiments did show that the front velocity is nearly constant with only an insignificant variation along the deck. This would be the reason for the agreement between Ritter's solution and the green water measurements even if the real dam-break flow is not well-predicted by the solution.

Fig. 5.3 shows the time history of the green water velocity at different locations on the deck. All the results in Fig. 5.2 are presented in Fig. 5.3, including the BIV measurements, results from the prediction model (Eq. (4.8)), and results from Ritter's

solution (Eqs. (5.3), (5.4), and (5.7)). Note that the first panel (Fig. 5.3 (a)) represents the location close to the leading edge of the deck while the last one (Fig. 5.3 (l)) locates right outside of the deck (the deck length is 370 mm). Therefore Fig. 5.3 (k) represents the last point on the deck. Similar to the results in Fig. 5.2, the prediction model shows very good agreements for all locations except at the locations very close to the end of the deck (Figs. 5.3 (j) and (k)) and outside of the deck (Fig. 5.3 (l)). On the other hand, Ritter's solution does a poor job in the prediction at the locations close to the leading edge of the deck, gradually improves downstream, and becomes reasonable at locations closer to the end of the deck. It is perhaps due to the linear nature of the solution. Ritter's solution gives a distinct shape in comparison with the measurements in Fig. 5.3, especially at the locations close to the leading edge of the deck. For the locations away from the leading edge, Ritter's solution with h_0 obtained from Eq. (5.7) over predicts the velocity, while the solution with h_0 obtained from Eq. (5.4) under predicts. However, the predictions for the magnitude of the front velocity of green water are quite close to the measurement. Since the front velocity may cause most damage, this again implies Ritter solution does provide "engineering accuracy" with reasonably good prediction for practical applications. The same conclusions were found when analyzing Fig. 5.2.

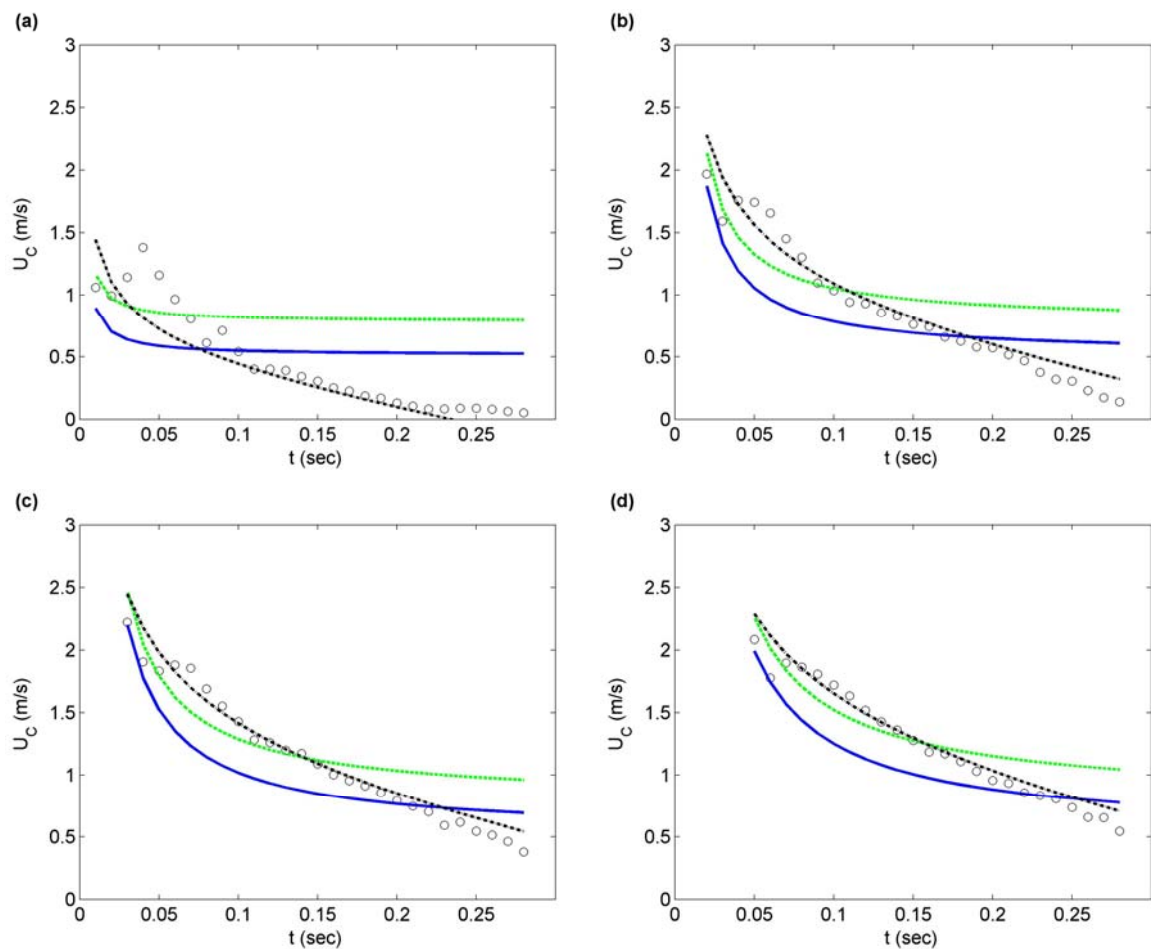


Fig. 5.3. Time history of horizontal velocity of green water at $x =$ (a) 5.7 mm, (b) 40.8 mm, (c) 75.9 mm, (d) 111.1 mm, (e) 146.2 mm, (f) 181.3 mm, (g) 216.5 mm, (h) 251.6 mm, (i) 286.7 mm, (j) 321.8 mm, (k) 356.9 mm, and (l) 378.0 mm. “o”, BIV measurements; solid line, Ritter’s solution with $h_0 = 6.0$ cm (obtained using Eq. (5.4)); dashed line, Ritter’s solution with $h_0 = 14.0$ cm (obtained using Eq. (5.7)); dashed-dotted line, prediction model (Eq. (4.8)).

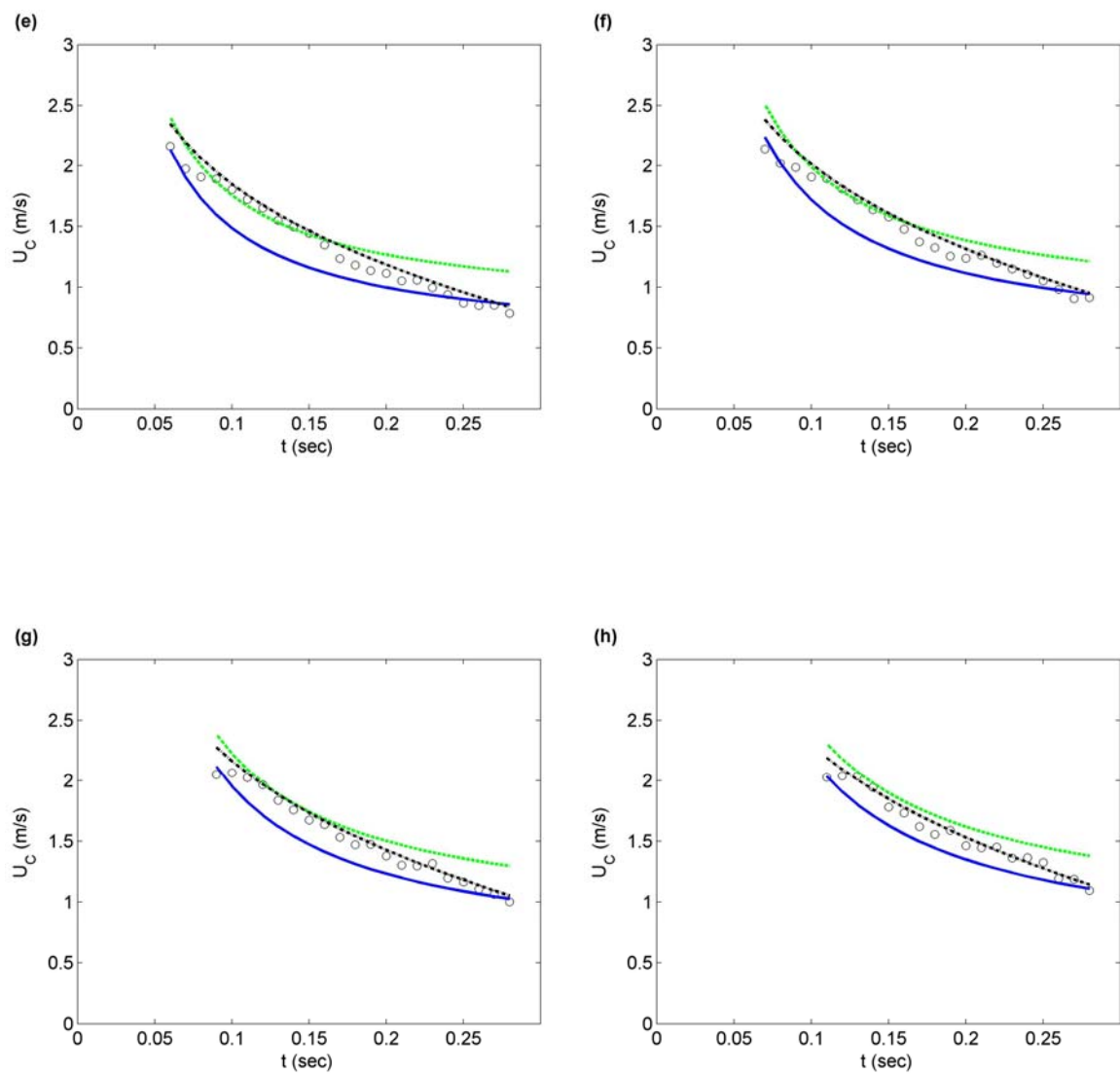


Fig. 5.3. (Continued)

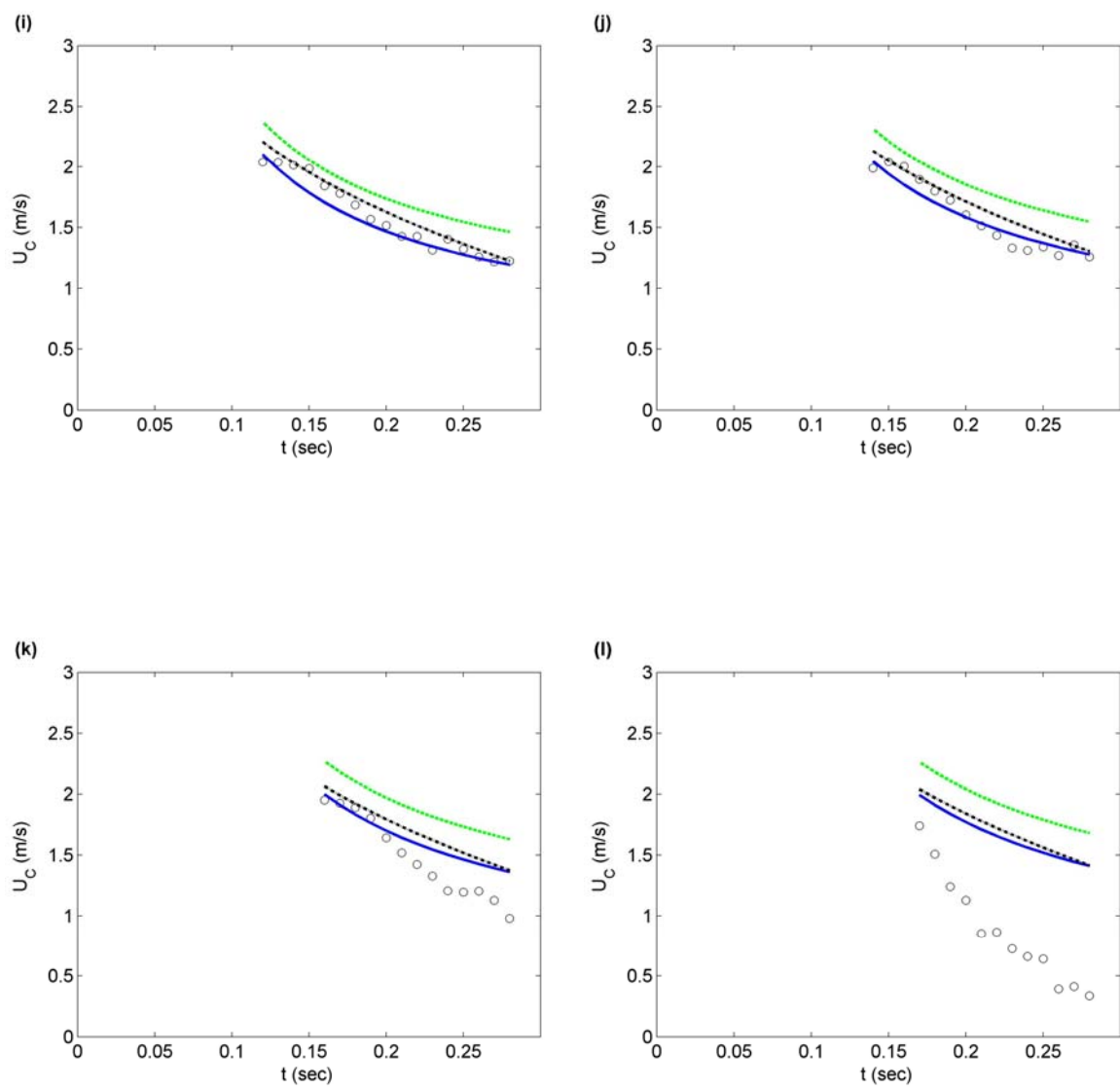


Fig. 5.3. (Continued)

5.6 Conclusion

In this chapter, the solution of dam-break flow was compared with the measured cross-sectional velocity of overtopping water on top of the simplified two-dimensional structure. The vertical distributions of measured horizontal velocities show that the cross-sectional velocity, maximum velocity at a cross-section, is not different significantly from the depth averaged velocity. The widely used dam-break solution for green water prediction works reasonably well if the initial water depth h_0 is carefully selected. This study suggests two equations for the determination of h_0 : Eqs. (5.4) and (5.7). The first one is estimated from the difference between the perfectly reflected deep water wave height and the free board above still water level while the second is one induced from the measured water front speed. The solution fails to predict the shape of the velocity distribution of green water but gives a reasonable prediction on the maximum velocity of the flow. This study suggests the use of $h_0 = (0.6C)^2 / g$ may give a better prediction if the solution of dam-break flow is to be used for green water prediction.

CHAPTER VI

VOID FRACTION OF OVERTOPPING WATER

6.1 Introduction

Breaking waves and any associated flows show two phase nature of air-water mixture. If breaking wave events occur near structures, aeration in the flow may be more prevalent. Thus, the aeration of breaking waves and induced flows is one of important properties in the wave breaking process. For example, if using only the velocity information in the prediction of forces exerted by a breaking wave, it would lead to overestimation because the flow is aerated and the aeration changes the density of the flow.

The study of void fractions in breaking waves has been carried out by many researchers. Lamarre and Melville (1992) developed an impedance probe to measure the void fraction in breaking waves in deep water and recorded the space-time evolution of the void fraction. Deane (1997) used both optical and acoustical methods for void fraction measurements of air entrainment in breaking waves. He found that the total void fractions were between 30% and 40%. Vagle and Farmer (1998) compared acoustical and electrical conductivity methods for bubble size and void fraction measurements. Chanson et al. (2002) studied unsteady air entrainment under a pseudo-plunging breaker and modeled the air entrainment produced by wave breaking. A vertical jet free falling into a stagnant fluid and the detrainment process were used in his study. Cox and Shin (2003) used an impedance void fraction meter (VFM) for

instantaneous void fraction measurements. They modeled the temporal variation of the normalized void fraction above the still water level by linear growth followed by exponential decay. They also showed that the distribution of void fraction above the still water normalized by the wave period and average void fraction is self-similar. While many studies like those mentioned above focus on the void fraction of breaking waves, there have been rare for studies focusing on the void fraction of breaking waves interacting with a structure.

In this chapter, void fraction measurements using the fiber optic reflectometer (FOR) technique were presented as a complement of the velocity measurements of the extreme wave impinging and overtopping. Void fraction was obtained over a fixed time duration to observe the temporal variation. The time-averaged void fraction at a given measurement point was then calculated. The void fraction measurements were presented with the velocity measured using BIV to examine the relation between these two. Using dimensional analysis, an empirical equation for the depth averaged void fraction was established. In addition, using the temporal and spatial distributions of void fractions and velocities, the flow rate and overtopping water volume were calculated.

6.2. Experimental setup and technique

The present study measured void fraction of green water using the fiber optic reflectometer (FOR) technique. The FOR technique was detailed in Chapter II. The void fraction measurements were performed only for the case with the extended deck. The void fraction was measured at 7 different downstream cross sections from $x = 0$ mm

(the leading edge of the deck) to $x = 300$ mm with a separation of 50 mm. Note that the deck of the model is 370 mm long. At each cross section, every 10 mm level from $z_d = 10$ to 150 mm was measured except the section of the leading edge where void fraction was measured up to $z_d = 80$ mm. Note that z_d is another vertical coordinate with $z_d = 0$ being at the deck surface while z is the vertical axis with $z = 0$ being at the stationary free surface (i.e., $z_d = z - 110$ mm). Since green water above $z_d = 100$ mm at the sections from $x = 50$ to 300 mm has a very short passing duration, less than 0.02 ms, and the void fraction close to 1 (i.e., 100% air), the regions up to $z_d = 100$ mm were analyzed in the present study.

The fiber tip of FOR was attached along very thin but rigid stainless steel circular needle with diameter less than 1 mm since the fiber tip is vulnerable. The probe was installed facing the wavemaker. Fig. 6.1 shows the FOR probe and setup. Since only void fraction was measured using the FOR system, the sampling rate of FOR measurements was kept as only 10 kHz throughout the experiments. The FOR system used in the present study is sketched in Fig. 2.6 and the measurement points of FOR on top of the model structure are shown in Fig. 6.2.

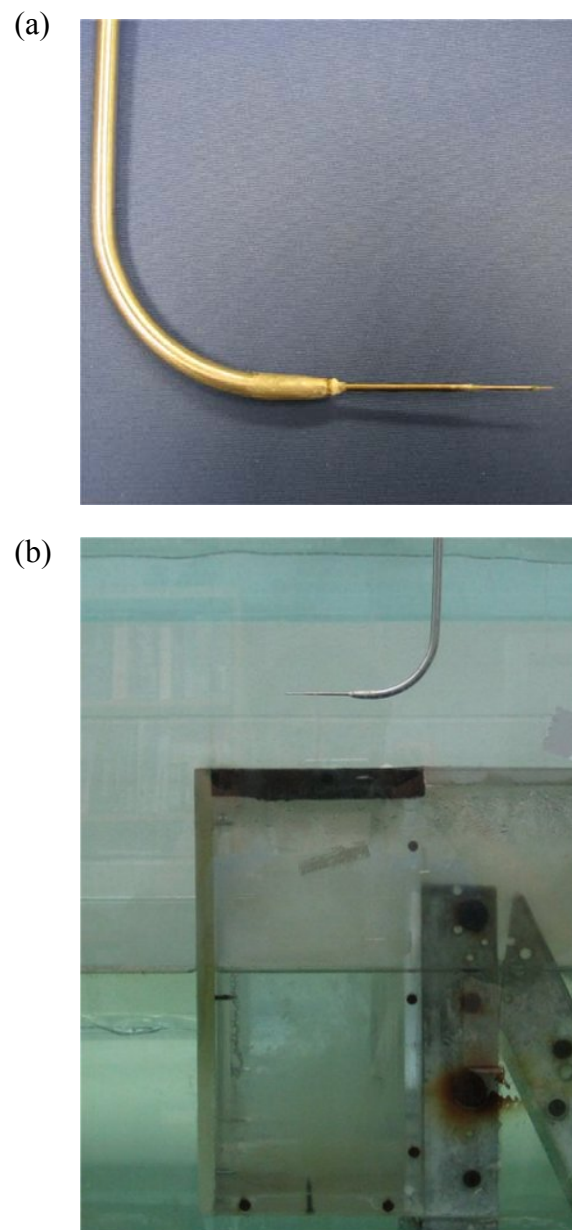


Fig. 6.1. (a) FOR probe; (b) setup of FOR in the experiments.

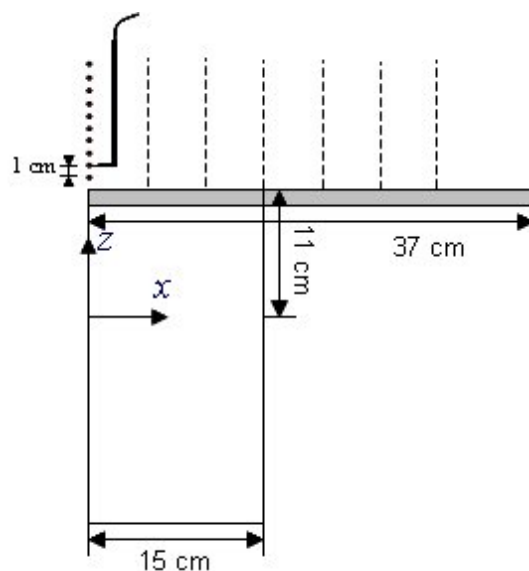


Fig. 6.2. Measurement points using FOR.

6.3 Void fraction and time history

The phase of green water flow at a measurement point is determined based on the signal acquired from the FOR system. From the obtained time history using FOR, void fraction is defined as the ratio of time duration of air (T_{air}) to that of the air-water mixture (T_{dur}) at a point of interest. In order to obtain the temporal variation of void fraction, the time history of measurements was binned every 0.01 ms for void fraction determination. The expression is as follows:

$$\alpha_i = \frac{T_{air,i}}{T_{dur,i}} \quad (6.1)$$

where α_i is the instantaneous void fraction, $T_{air,j}$ the duration of air phase, $T_{dur,j}$ the duration of flow of interest, which is set at 0.01 s in the present study. Thus, $\alpha_i = 1$ indicates air while $\alpha_i = 0$ indicates water.

Since the sampling rate of FOR measurements in the present study was kept as 10 kHz, 100 samples of FOR signals were used to determine one void fraction over the time duration of 0.01 s. If void fraction is measured with a void fraction meter (VFM) at a sampling rate of 100 Hz, results would be close to each other. Based on the void fraction determination, a time series of void fractions with time difference of 10 ms was obtained. Since the green water flow is very turbulent, as shown in Chapter IV with the turbulence intensity measurement, phase average is used to obtain the mean property of void fraction for further analysis, expressed as follows:

$$\alpha = \frac{\sum \alpha_i}{ns} \quad (6.2)$$

where α is the phase averaged void fraction and ns the number of repeated samples. In this study, 20 instantaneous void fractions were used to calculate the ensemble-averaged void fraction.

Fig. 6.3 shows the time series of void fraction. Time histories of void fractions at 10 different vertical positions are plotted for every 50 mm downstream in the figure. From the time histories, it is seen that the green water generated by the plunging breaker is highly aerated in its frontal region. As the front of the green water passed a measurement point and moves downstream, the green water became less aerated. The evidence is the downward slope of void fraction against time in the figure. After green water reached the lowest void fraction, it either immediately passed the measurement point or continued with the low void fraction until it passed the point. From this observation, we conclude that the green water is more aerated near the front and less aerated near the rear free surface.

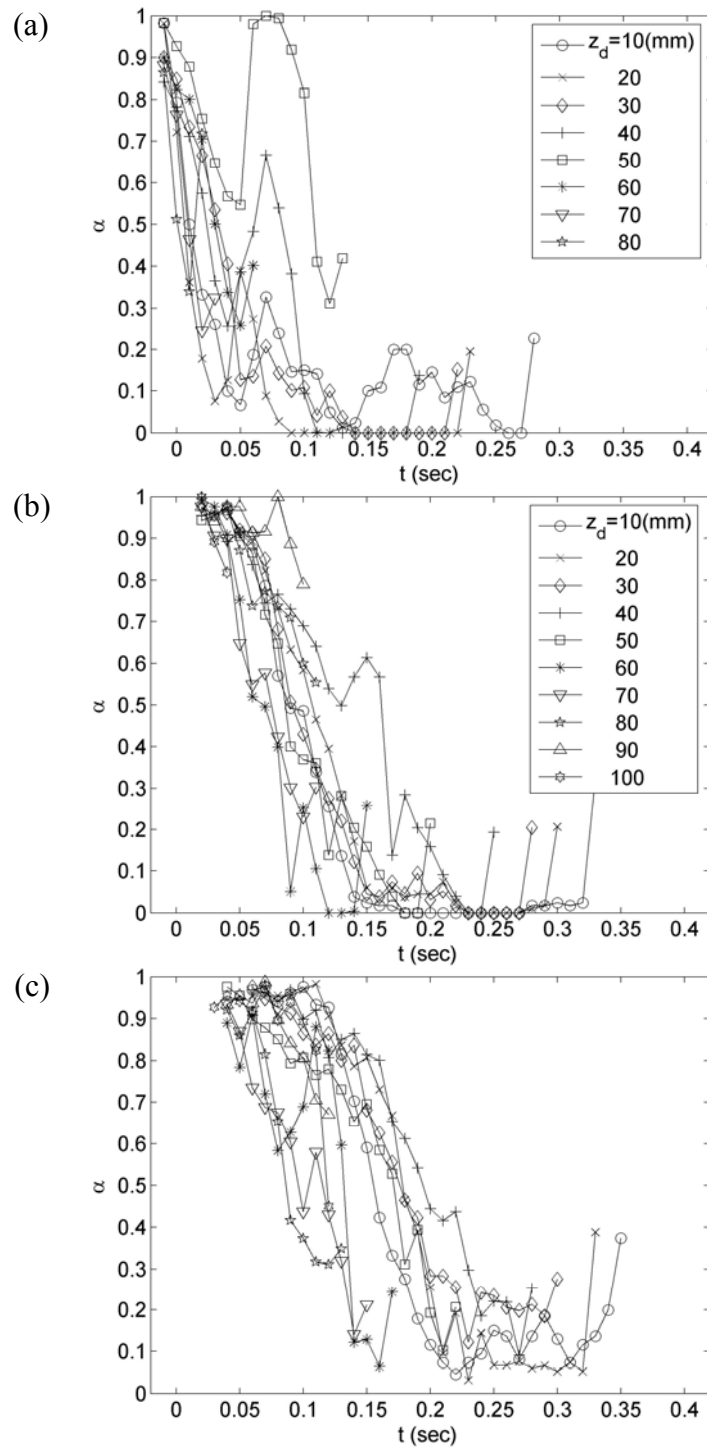


Fig. 6.3. Time series of the void fractions at $x =$ (a) 0 mm, (b) 50 mm, (c) 100 mm, (d) 150 mm, (e) 200 mm, (f) 250 mm, and (g) 300 mm. Measurements at 10 vertical locations were measured and shown in the legend in (a) and (b).

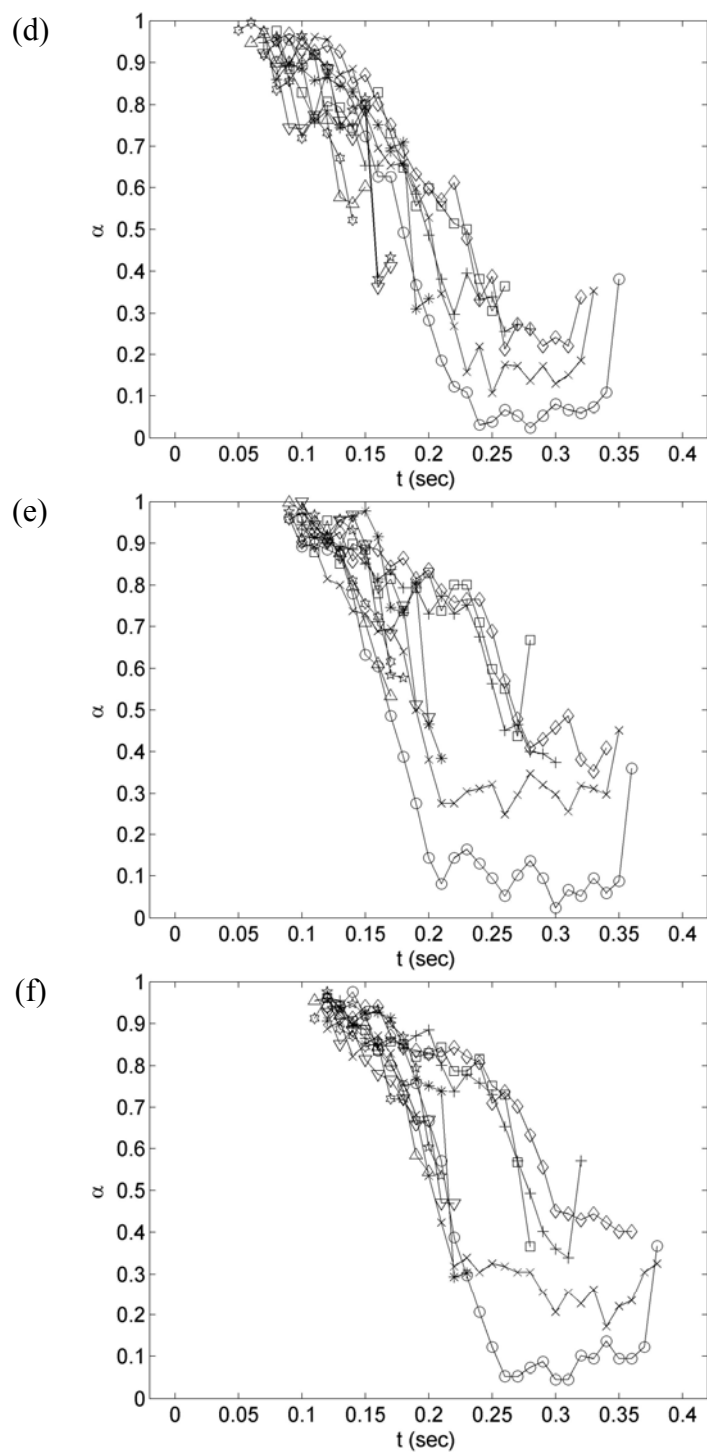


Fig. 6.3. (continued)

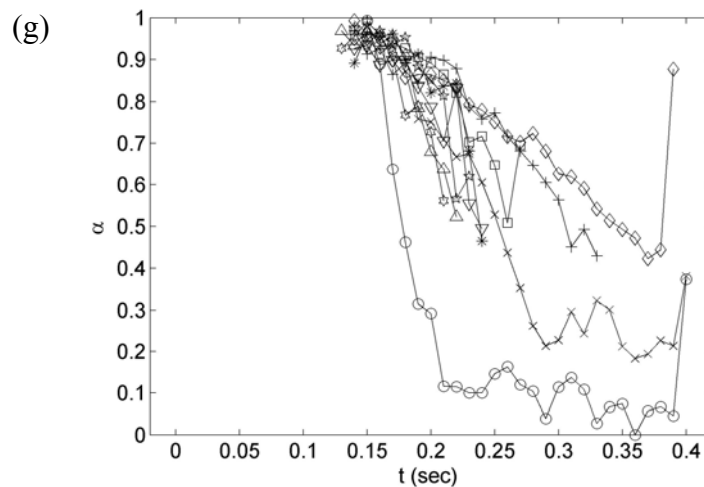


Fig. 6.3. (continued)

From the leading edge of the deck at $x = 0$ mm to the section at $x = 100$ mm shown in Figs. 6.3 (a) to (c), the region of green water closer to the deck surface (below $z_d = 50$ mm) had a duration of weak aeration with a range of $\alpha = 0$ to 0.3. On the contrary, the void fraction kept decreasing above $z_d = 50$ mm at the leading edge until the green water completely passed. Beyond $x = 100$ mm (Figs. 6.3 (c) to (g)), there was no region with $\alpha = 0$, unlike the cross-sections at $x < 100$ mm. From $x = 0$ mm to 150 mm, the duration of low aeration decreased as x increases and as z increases. This means the magnitude of the void fraction tended to increase at downstream locations or higher vertical levels. From $x = 200$ mm to 300 mm, however, the duration of the low aeration in the region below $z_d = 20$ mm increased. The temporal distributions display a similar pattern at cross sections beyond $x = 200$ mm as shown in Figs. 6.3 (e-g). We would like to point out that the green water impinged on the deck between $x = 150$ mm and 200 mm after running up in experiment. It is found that the distributions in the region beyond the impinging point are similar.

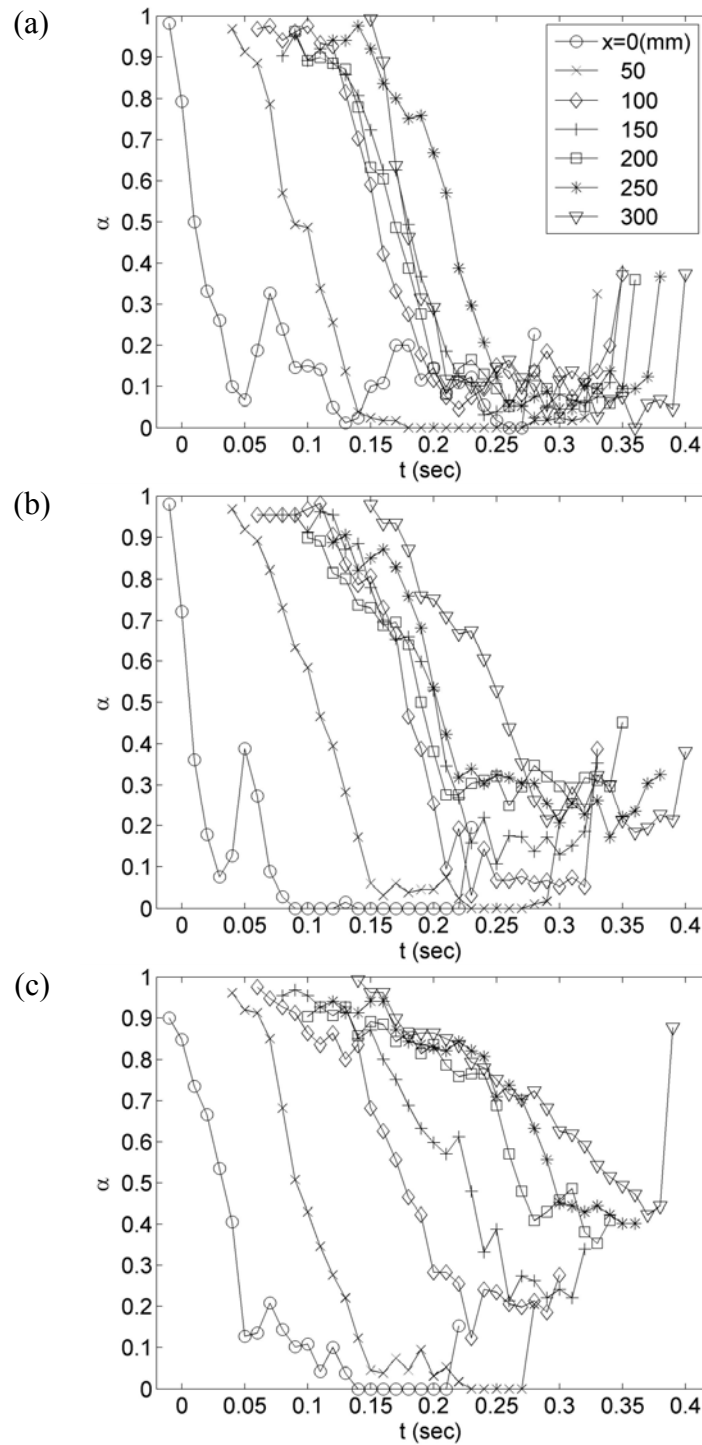


Fig. 6.4. Time series of the void fractions at vertical locations. $z_d =$ (a) 10 mm, (b) 20 mm, (c) 30 mm, (d) 40 mm, (e) 50 mm, (f) 60 mm, (g) 70 mm, (h) 80 mm, (i) 90 mm, and (j) 100 mm.

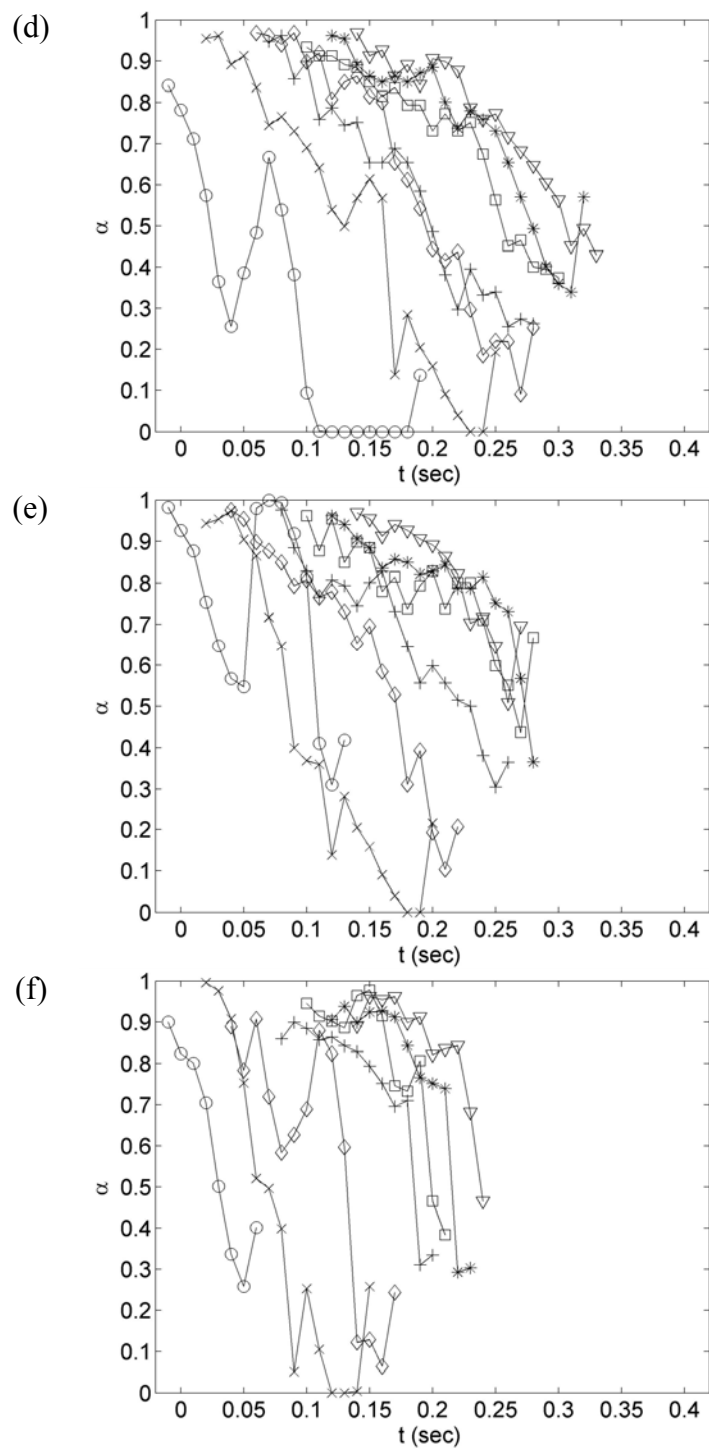


Fig. 6.4. (continued)

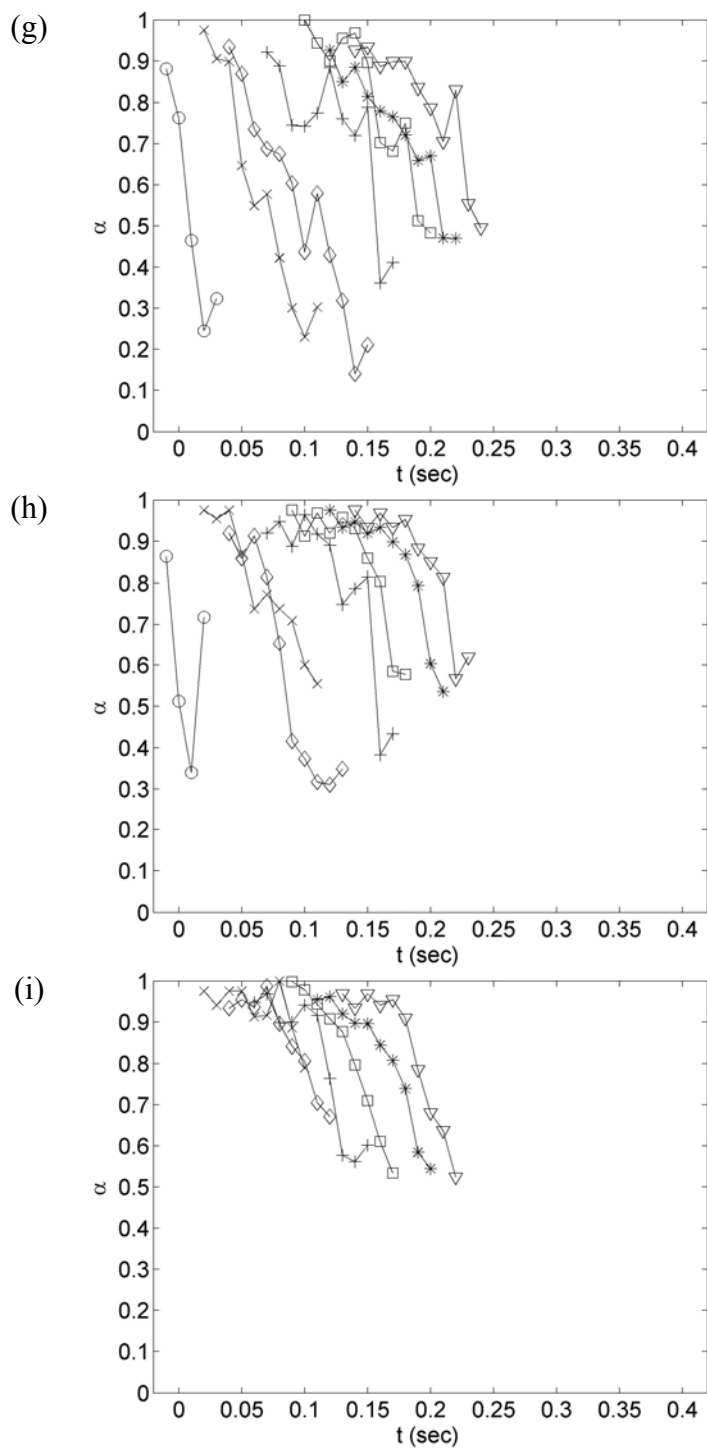


Fig. 6.4. (continued)

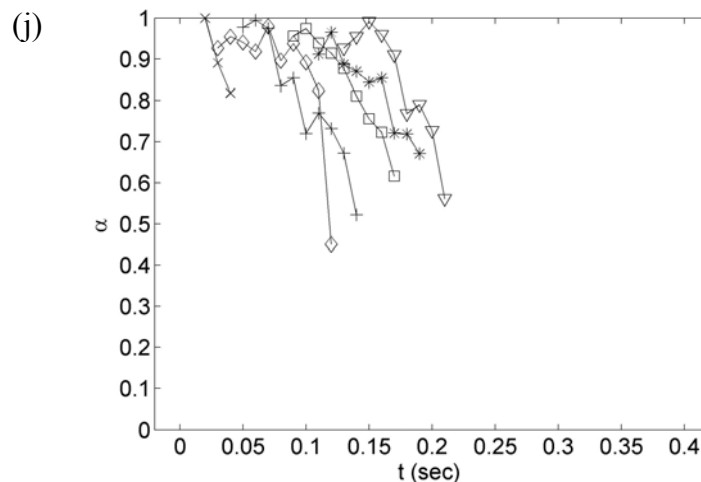


Fig. 6.4. (continued)

Fig. 6.4 plots the time history of void fractions along the deck at each vertical level to examine the variations. The plotting clarifies the patterns found in the previous figures at several locations along the deck. From the slope of the void fraction against time, it shows a rapid decrease of aeration after the passage of the water front. Since the aeration is related with the density of the air-water mixture, the dropping time or slope of void fraction may be an important factor in estimating wave forces. The decrease of void fraction was fitted linearly, even though it fluctuated at certain period. At $z_d = 10$ mm, the region near the deck (Fig. 6.4 (a)), all distributions along the deck showed a similar slope. At the higher vertical locations, the slope of the distributions became less steep for farther downstream locations from the leading edge. This pattern started at $z_d = 20$ mm (Fig. 6.4 (b)) and became clear at $z_d = 30$ mm to 80 mm (Figs. 6.4 (b-h)). The decrease of the slope indicates the slow decrease of void fraction from about unity to near zero or a very low value. This consequently results in higher aeration at a point of interest. From the figure, it is seen that the magnitude of most

void fractions tended to increase as x increases and z_d increases. From Figs. 6.3 and 6.4, we conclude that the void fraction drops slowly at the downstream cross-sections and higher levels before the impingement point on the deck. After the impingement point, the vertical distributions of void fraction became similar.

As mentioned above, some temporal distributions between $x = 0$ mm and 100 mm during the decrease of void fraction fluctuated significantly (Figs. 6.3 and 6.4). The fluctuating distributions display a second peak before reaching the lowest void fraction. Such distributions might be caused by the behavior of green water induced by the plunging breaker. A plunging breaker generates air pockets when it impinged on a structure. Since the plunging breaker generated a relatively large air pocket in front of the structure in this study, distinct aeration patterns occurred due to two different causes. When the wave impinged on the structure, the water front broke and became aerated due to the impingement of the breaking wave. At the same time, an air pocket was formed by the plunging breaker. The aerated region due to the air pocket ran up along the front wall of the structure and overtopped the structure. It is expected that there is a time difference between the first aeration by the impingement and the second aeration by the air pocket. The time difference would lead to green water with two relatively strongly aerated regions. In the figures, the beginning void fraction of green water (close to 1) indicates the aeration of the water front. Moreover, the second peak in the distribution might be due to the aeration by the air pocket following the frontal aeration. The second peak was observed in more vertical locations (i.e., wider region) as x increases up to $x = 100$ mm. This also means that the aeration tends to extend vertically.

6.4 Vertical distribution of void fraction along the deck

Fig. 6.5 shows a series of vertical distributions of void fractions along the deck from $t = 0.00$ s to 0.28 s. Void fractions were plotted at each vertical cross section along the deck in order to see the spatial variation at different time steps. In the figure, horizontal velocities were also plotted along with the void fractions. This is to see if there is any correlation between these two.

The measurements of void fractions and velocities were performed separately in this study. Thus, time steps of the two properties were matched based on the instant when the rear free surface of green water was passing the leading edge of the deck (at $x = 0$). It is because the rear surface is less fluctuating and turbulent. This was verified by phase averaging raw image. The phase averaged image was obtained as follows: (1) superimpose instantaneous images based on $t = 0$ s, and (2) divide the superimposed image by the number of the images. In the obtained phase averaged images, the frontal area was blurry while the rear free surface looked like a clear solid line with thin thickness. This means that there is no significant difference in the rear free surface elevations along instantaneous images and so as in the phase matching. Fig. 6.4 clearly shows the propagation and surfaces of green water on the deck. As shown in the temporal distributions (Figs. 6.3 and 6.4), the frontal region of green water was air dominant ($\alpha \approx 1$) while the region near the rear free surface was water dominant ($\alpha \approx 0$).

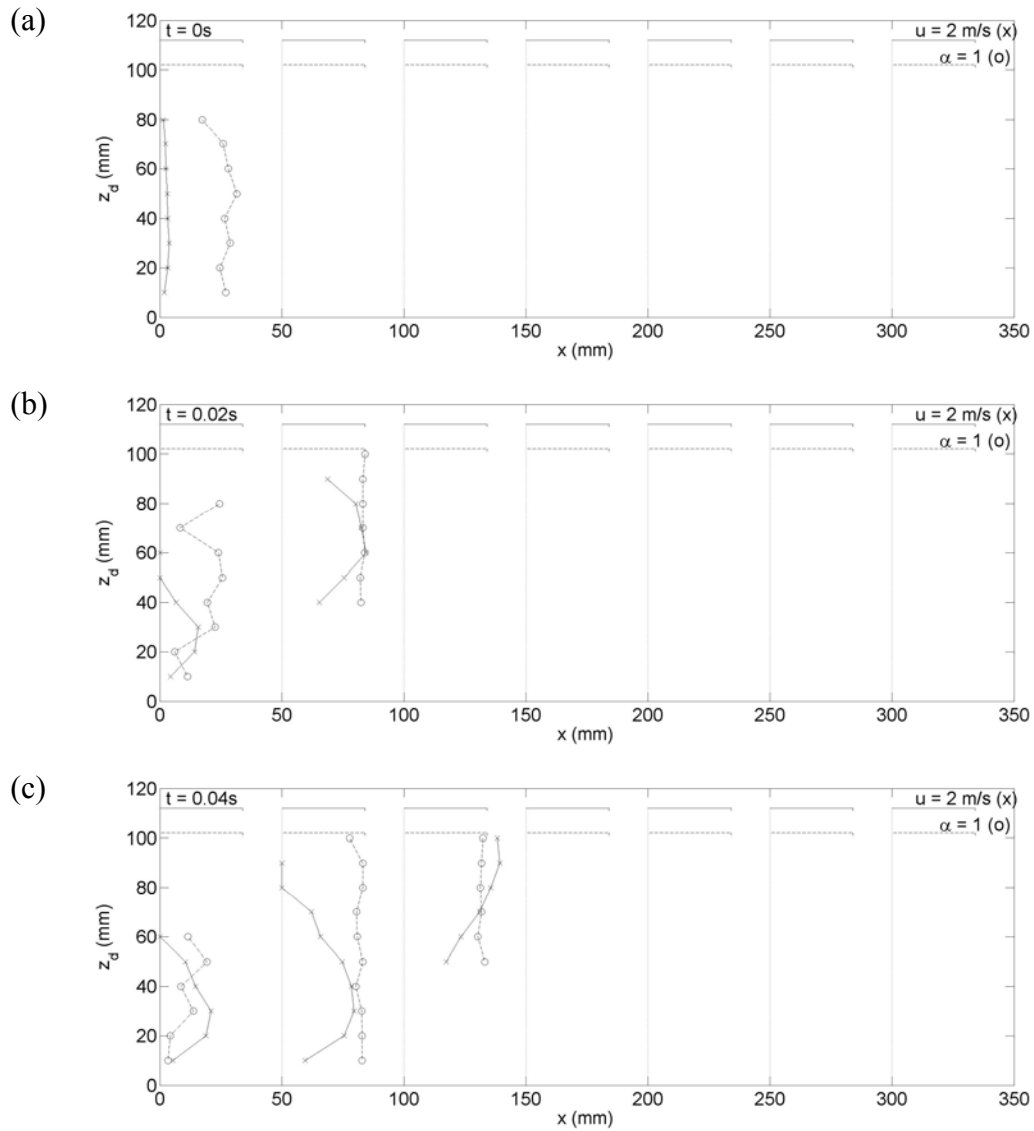


Fig. 6.5. Vertical distribution of void fractions and horizontal velocities of green water along the deck at $t =$ (a) 0.00 s, (b) 0.02 s, (c) 0.04 s, (d) 0.06 s, (e) 0.08 s, (f) 0.10 s, (g) 0.12 s, (h) 0.14 s, (i) 0.16 s, (j) 0.18 s, (k) 0.20 s, (l) 0.22 s, (m) 0.24 s, (n) 0.26 s, and (o) 0.28 s. -o-, void fraction; -x-, velocity.

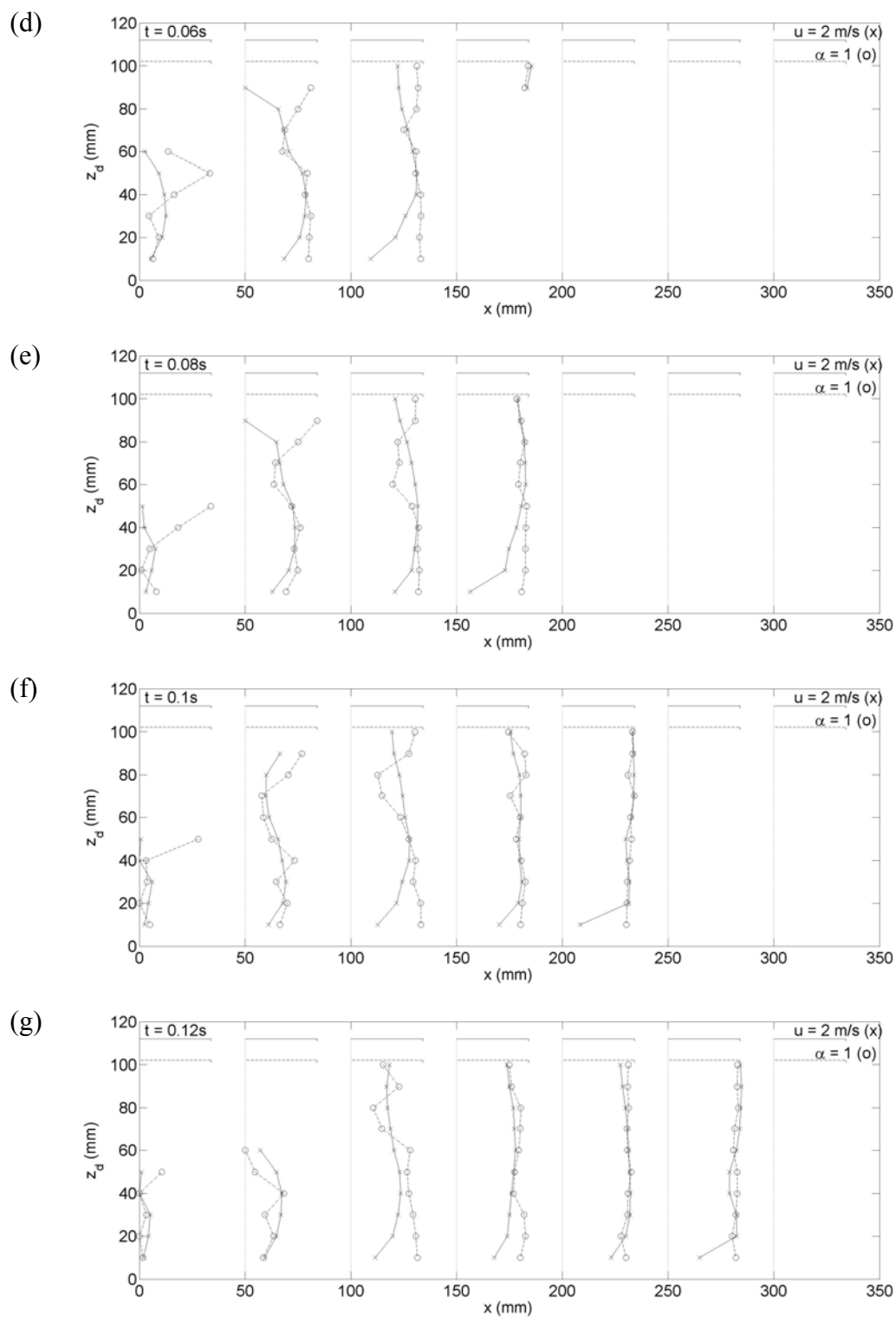


Fig. 6.5. (continued)

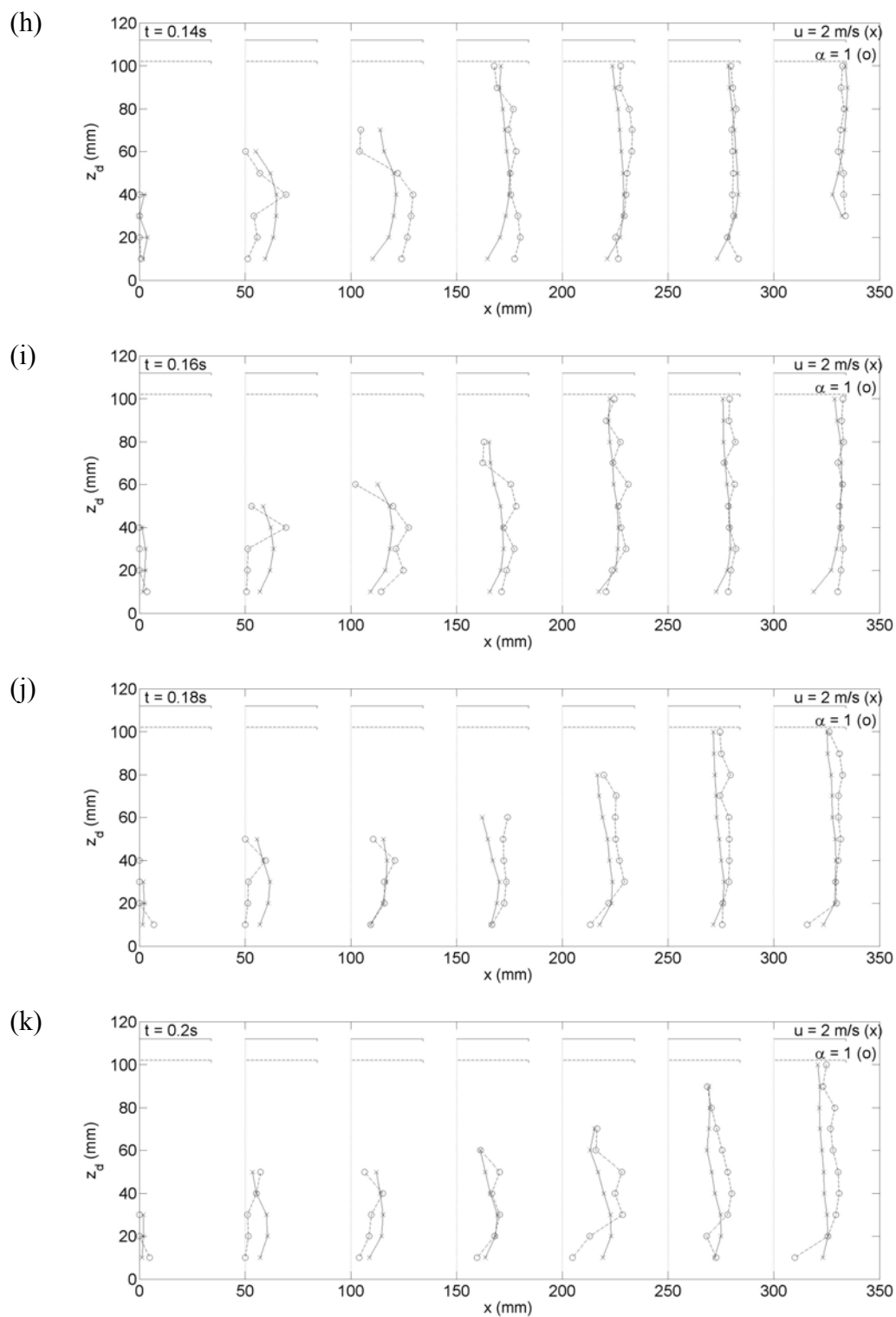


Fig. 6.5. (continued)

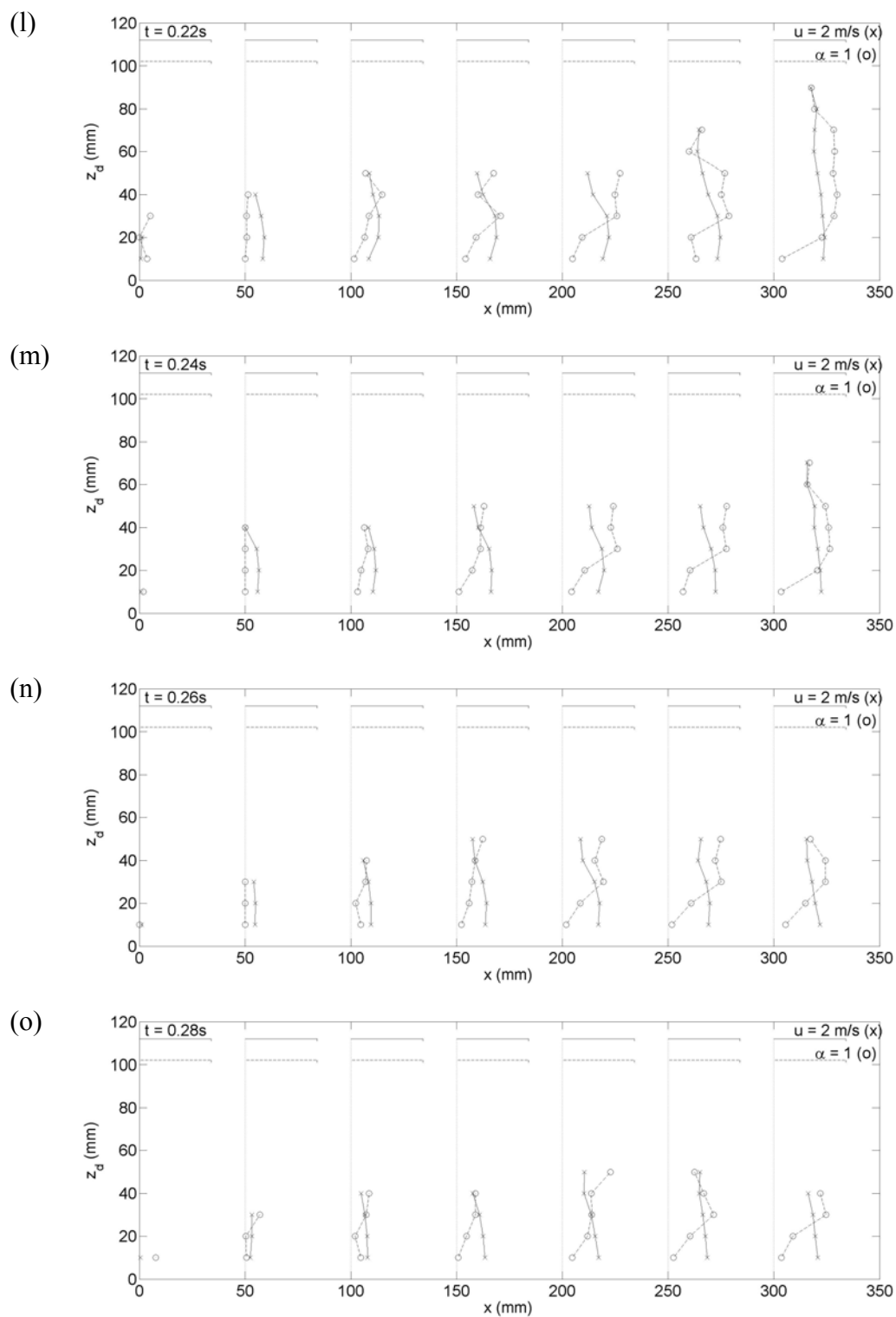


Fig. 6.5. (continued)

When the green water running onto the deck, impinging on the deck surface and passing the end of the deck, the front of the green water was highly aerated. The void fraction near the front was close to 1. From $t = 0.00$ s to 0.06 s (Figs. 6.5 (a-d)), the void fraction near the leading edge fluctuated along the vertical axis after the green water front passed. After $t = 0.12$ s (Fig. 6.5 (g)), interestingly, the distribution of the void fraction was similar to that of the velocity. Even though there are some discrepancies between the distributions, the patterns are similar. Strong aeration (high void fraction) occurred in the region where relatively large velocities were shown. Moreover, the region of weak aeration (low void fraction) showed smaller velocities. The general pattern that the weak aeration occurred near the deck and free surface is also clearly seen in the figure. After $t = 0.22$ s (Fig. 6.5 (l)), the patterns between void fraction and velocity are no longer similar. Void fractions tended to increase as velocities decreased. At $t = 0.22$ s, depth averaged velocities were about one half of the phase speed in that regions ($x = 100$ mm to 250 mm). After that instant, the distributions show that the region near the free surface was more aerated than that near the deck surface.

Void fraction discussed in the present study was obtained for binning the measurement over every 0.01 s. I further define the “total void fraction” to represent the time-averaged aeration at a measurement point. The total void fraction is defined as the void fraction over the entire period of green water at a given point. Therefore in the present study the time-averaged void fraction is indeed the same as the total void fraction defined here. The obtained time-averaged void fraction is shown in Fig. 6.6. It shows that the distributions change gradually along downstream cross-sections.

Depending on the pattern of the vertical distribution, the time averaged void fractions in Fig. 6.6 were divided into three categorizations and shown in Fig. 6.7. In the region from $x = 0$ mm to 50 mm, the time-averaged void fraction exhibits a nearly linear distribution against the vertical positions (Fig. 6.7 (a)). In the region from $x = 100$ to 150 mm in Fig. 6.7 (b), the distribution does not display a unique pattern and does not overlap. Instead, the two profiles appear to be transient from the linear distribution at the upstream locations (Fig. 6.7 (a)) to the boundary-layer like distribution at the downstream locations (Fig. 6.7 (c)). The distributions in the region after $x = 200$ mm are like the typical boundary-layer velocity profile. Even though the maximum void fraction occurs around $z_d = 40$ mm, the variation above this level is insignificant.

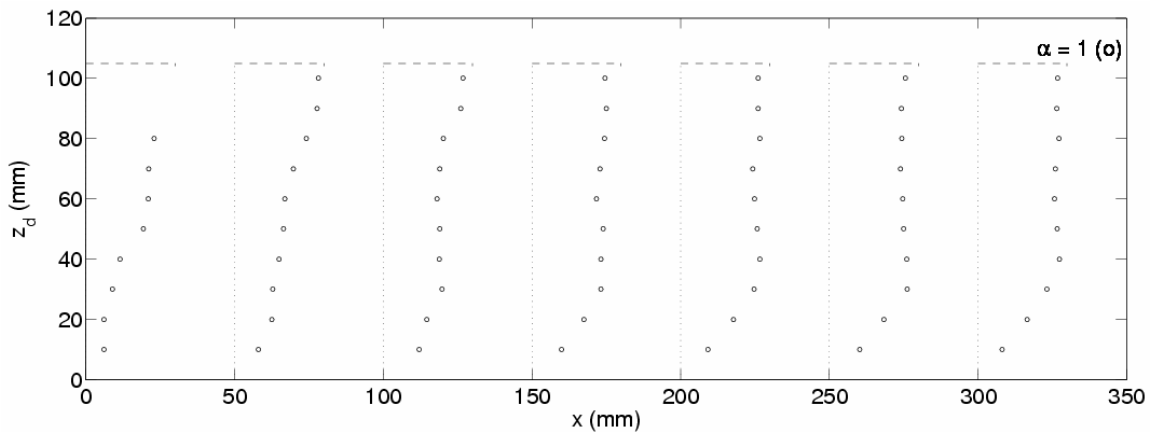


Fig. 6.6. Vertical distribution of time-averaged void fraction.

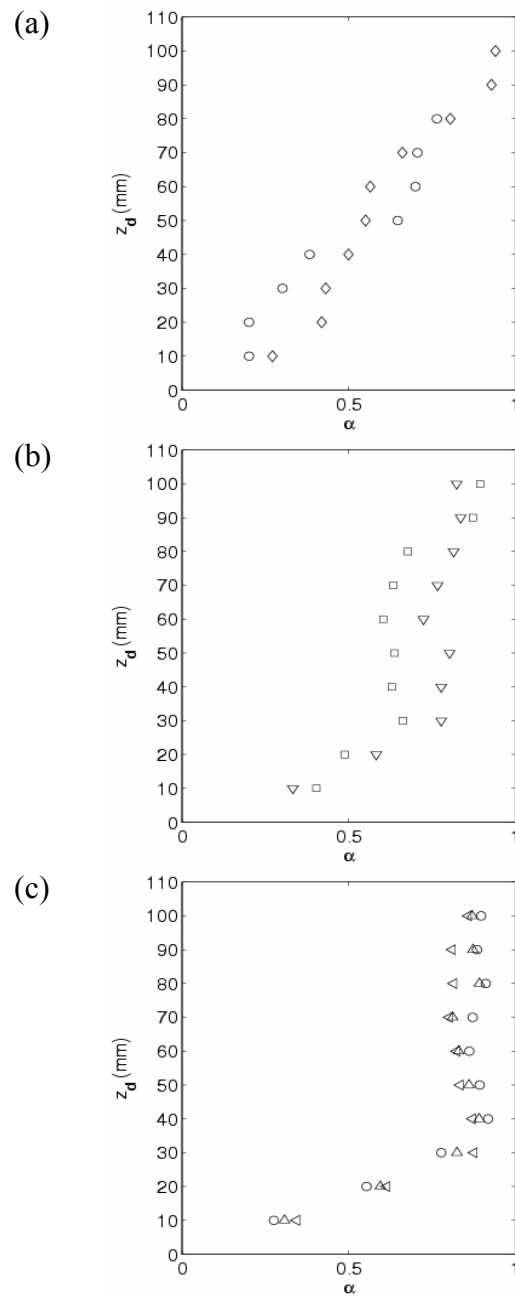


Fig. 6.7. Distribution of time averaged void fraction in three regions. (a) $x = 0$ mm (\circ) and 50 (\diamond) mm; (b) $x = 100$ mm (\square) and 150 (∇) mm; (c) $x = 200$ mm (\circ), 250 (Δ), and 300 (\triangleleft) mm.

6.5 Dimensional analysis

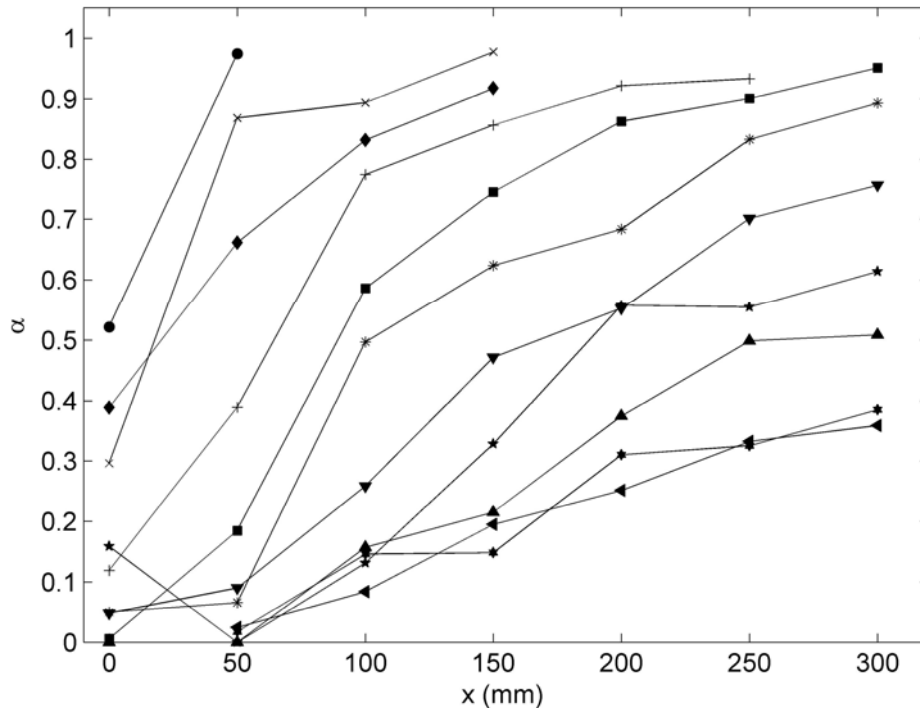


Fig. 6.8. Distribution of depth averaged void fraction; $t = 0.02$ s (●), 0.05 s (×), 0.08 s (◆), 0.11 s (+), 0.14 s (■), 0.17 s (*), 0.20 s (▼), 0.23 s (★), 0.26 s (▲), 0.29 s (★), and 0.32 s (◄).

Fig. 6.8 shows the depth averaged void fraction along the deck from $t = 0.02$ s to 0.32 s. The distribution looks similar to that of the cross-sectional velocity and depth averaged velocity. The maximum occurred at the water front and while the magnitude gradually decreased as time increased.

In order to obtain an equation describing the distribution of the depth averaged void fraction along the deck, the similarity analysis method was used. Since the pattern of the void fraction distribution is similar to that of the velocity distribution, we used the

same non-dimensional parameters in the similarity analysis except replacing the dimensionless velocity by the void fraction. The result from the similarity analysis is shown in Fig. 6.9. Interestingly and expected, the void fraction is also self-similar. The solid line in the figure is the regression result. The regression equation is obtained by least-square curve-fitting the relation between $a+b(t/T)$ and x/Ct and can be expressed as:

$$\alpha + 1.40 \frac{t}{T} = 1.10 \left(\frac{x}{Ct} \right)^{0.50} \quad (6.3)$$

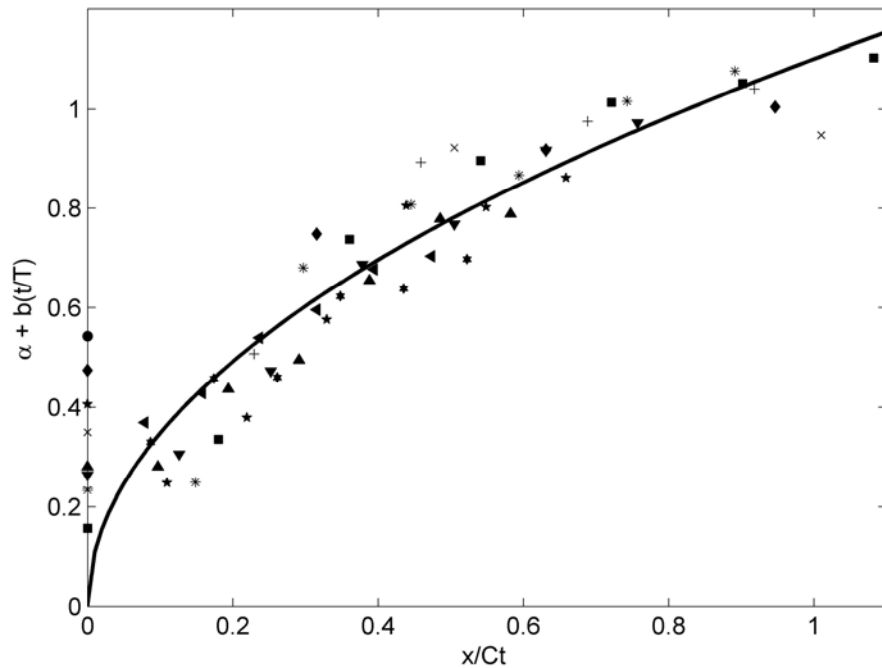


Fig. 6.9. Similarity plot of void fraction and regression. Filled symbols, data taken from $t = 0.02$ s to 0.24 s; solid line, regression Eq. (6.3).

The correlation coefficient, r^2 , is 0.80. The regression equation is compared with the

void fraction measurements and shown in Fig. 6.10. Although the equation tends to underpredict void fraction near the leading edge, it shows good agreement for the rest sections on the deck.

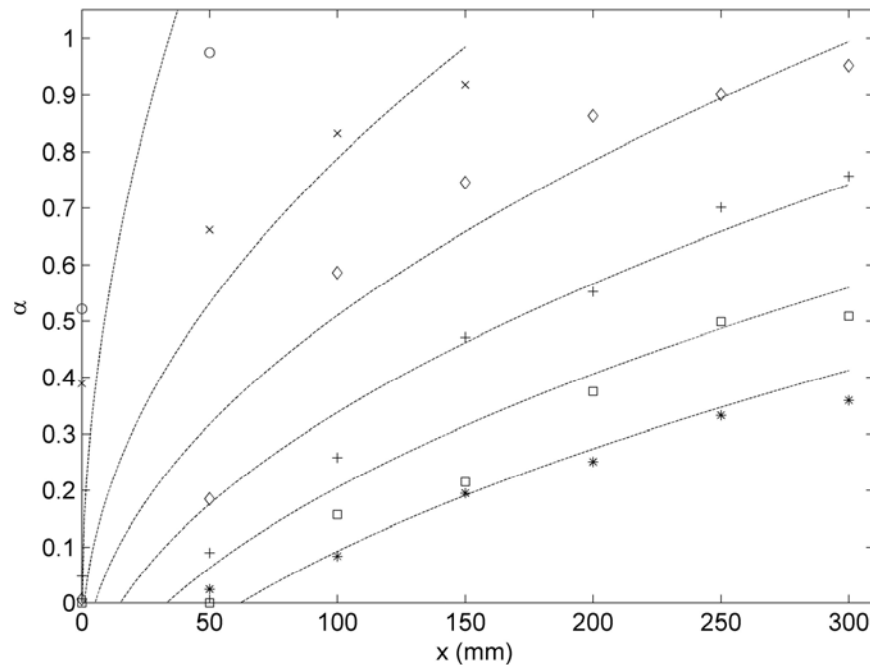


Fig. 6.10. Comparison of void fraction between measurements and regression equation at $t = 0.02$ s (\circ), 0.08 s (\times), 0.14 s (\diamond), 0.20 s ($+$), 0.26 s (\square), 0.29 s ($*$). Dotted lines, regression equation.

6.6 Flow rate and overtopping water volume

Using the measured velocities and void fractions, flow rate was calculated at six different measurement sections ($x = 50 \sim 300$ mm) on the deck. Since the velocity measured in the present study was indeed the velocity of the air-water mixture, void

fraction is necessary for flow rate estimate. The flow rate of the leading edge was not estimated in this study. The velocities of the air-water mixture at the leading edge were relatively smaller than other sections. If velocities of bubbles are small, it is expected there is difference in velocity between the bubbles and ambient fluid. Consequently, this would lead to erroneous estimation. The flow rate, Q was calculated as follows:

$$Q = \int_{h_l}^h (1 - \alpha) U dz_d \quad (6.4)$$

where h is the upper water surface of the green water on the deck and h_l is the lower water surface.

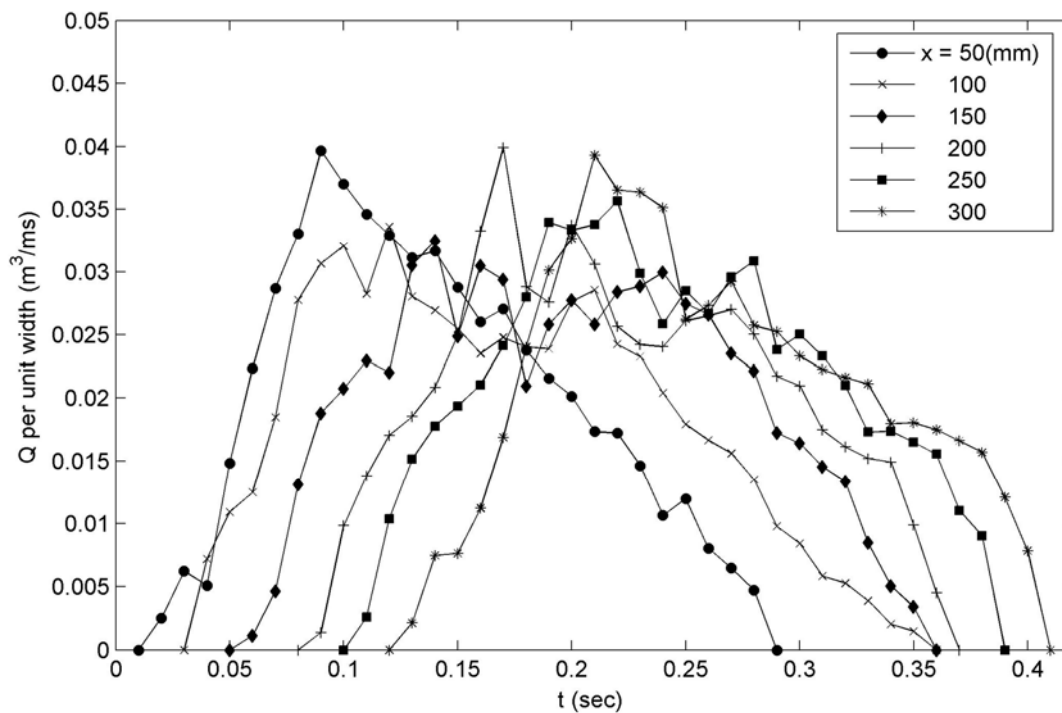


Fig. 6.11. Flow rate at downstream locations.

Fig. 6.11 shows the calculated flow rate at several locations along the deck. At each section, the flow rate increased linearly, reached the maximum, and then decreased

linearly. The slope of the flow rate is nearly constant at each section. The maximum flow rate occurred at about 0.10 s after the water front reached a specific measurement section. The flow rate calculated in this study does not cover the whole green water flow field as mentioned in the section of experimental setup. The flow rate was obtained by integrating vertically from 0 mm to 100 mm above the deck. Although the measurements were performed above $z_d = 100$ mm, green water at those points are very highly aerated (mostly over than 0.95) with a very short duration with a negligible contribution.

The total water volume, V , was calculated from the flow rate by integrating Q with respect to time as follows:

$$V = \int_{T_s}^{T_e} Q dt = \int_{T_s}^{T_e} \int_{h_i}^h (1 - \alpha) U dz_d dt \quad (6.5)$$

where T_s is the starting time of the green water flow and T_e is the ending time. Fig. 6.12 shows the volume of overtopping water over the structure. The calculated volume is quite constant with only small fluctuations. The volume was also compared with the measurements of overtopping water volume in the figure. The overtopping water was collected behind the structure using a large container. The section of wave tank behind the model structure was screened and sealed with vinyl for the collection of the overtopping water. The volume of the collected overtopping water in the container through small slots was measured. The directly measured mean volume was $5.60 \times 10^{-3} \text{ m}^3$. The mean water volume per unit width can be estimated by dividing the width of the wave flume as $6.33 \times 10^{-3} \text{ m}^3$. Very good agreement was obtained between the

calculated volume and the directly measured volume expect at $x = 50$ mm. The comparison shows mass is conserved so the experiments for void fraction determination in the present study are reliable.

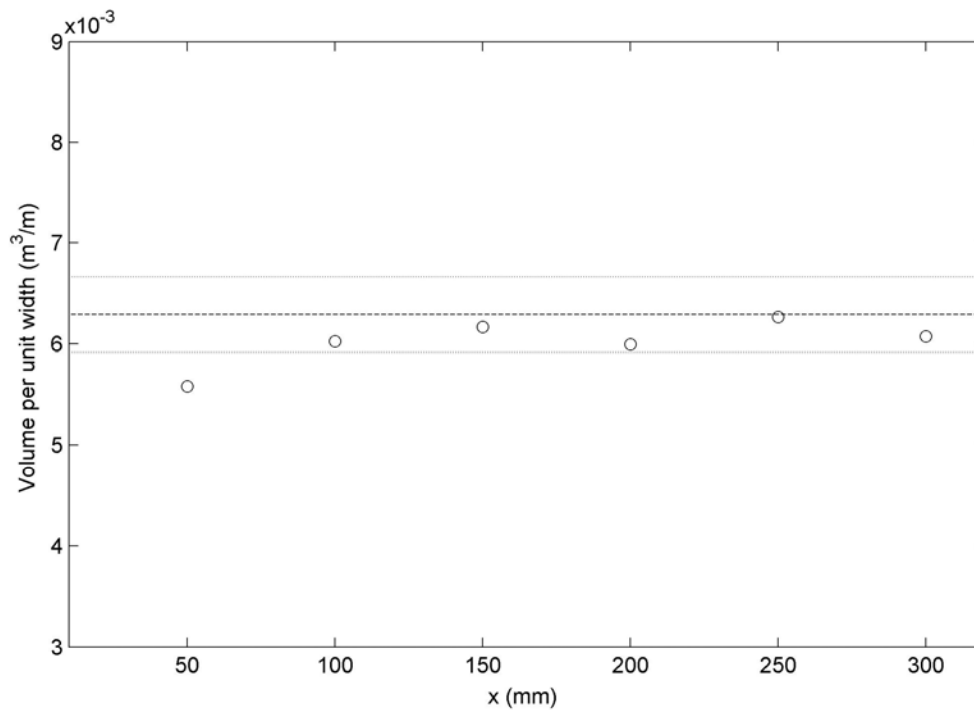


Fig. 6.12. Comparison of water volume. Temporal integration of flow rate, \circ ; direct measurement using collection tank, thick dashed line (mean) and thin solid line (standard deviation).

6.7 Conclusion

The measurements of void ratio were carried out using fiber optic reflectometer (FOR) to investigate the aeration of green water. The temporal and spatial distributions of the void fraction show that the frontal area of green water was highly aerated and the

region near the rear free surface was relatively less aerated. After the water front passed the end of the deck, the region near the deck became less aerated than the free surface area. The total void fraction was distributed linearly near the leading edge showing high aeration near the free surface and low aeration near the deck. As downstream locations, the area of high aeration was expanded. The region beyond $x = 200$ mm showed similar distribution of void fraction. We also would like to point out that the impingement of green water on the deck occurred between $x = 150$ mm and 200 mm. Void fractions and velocities were used to estimate flow rate and water volume at a cross-section. Due to the strong aeration of the frontal region of green water, the flow rate at each cross-section gradually increased from 0. After about 0.1 seconds, it reached the maximum, and then decreased until the green water completely passed a section. The water volume was estimated by integrating the flow rate with respect to time. The estimated water volume was quite constant, which shows mass is conserved. The water volume estimation was also compared with the directly measured overtopping water volume behind the structure. The comparison was in a good agreement and proved that the void fraction experiments of the present study were reliable.

CHAPTER VII

SUMMARY AND RECOMMENDATIONS FOR FUTURE STUDY

7.1 Summary

For experimental approach, the measurements of velocity field of a plunging breaking wave impinging on a model structure and associated green water on top of the structure were successfully performed using two modern image based techniques – particle image velocimetry (PIV) and bubble image velocimetry (BIV). The latter technique was developed primarily for the velocity measurements in the multiphase bubbly flows. The velocity measurements were performed for the structure with short deck and extended deck. By analyzing the measurements, a prediction equation was resulted in for the horizontal green water velocity distribution along the deck. The prediction equation was compared, along with the measured data, with the widely used dam break solution for green water prediction. As a complement of the velocity measurements in the present study, the measurements of void fraction of green water were also carried out employing fiber optic reflectometer (FOR). The important findings are as follows:

- The maximum horizontal velocity reached $1.5C$ with C being the wave phase speed before the overturning jet of the breaking wave impinging on the structure. This velocity is consistent with that measured in many other studies on breaking waves (without interactions with structures).

- The front velocity of green water on the deck was approximately constant and equal to $1.1C$ to $1.2C$ along the deck. The maximum horizontal velocity during the period when the front of green water was on the deck is consistent with the front velocity of the green water. The location of the maximum horizontal velocity was also close to that of the front of green water during that period. The maximum horizontal velocity gradually decreased after the front of green water fallen back into the “ocean” after it passed the end of the deck.
- The vertical velocity of the upward moving splashing water right after the impinging of the breaking wave on the structure but before the wave becomes horizontal and moves onto the deck is huge – reached a maximum value of $2.8C$. This velocity occurred on the front wall of the structure. It could result in significant damages to a deck or structure and equipment protruding from the wall when they are hit by this fast moving water from below.
- The turbulence level of green water was between 40% and 50% of the maximum velocity at the particular given moment during the entire period when the front of green water was on the deck.
- A prediction equation for the horizontal velocity distribution of green water along the deck was obtained applying dimensional analysis and the measurement data. The equation was present in Eq. (4.8), and repeated here as

$$U_C = U_M \left[1.02 \left(\frac{x}{Ct} \right)^{0.34} - 1.20 \frac{t}{T} \right] \quad \text{for } U_C \leq U_M$$

$$U_M = 1.15C$$

in which U_C is the horizontal velocity of green water on the deck, C the phase speed of the breaking wave, T the wave period, x the horizontal coordinate with $x = 0$ at the leading edge of the deck, t the time. Note that this equation is valid during the entire period when the front of the green water was on the deck, and after the front fallen into the ocean - meaning it is valid during the entire green water process. Comparisons show this prediction equation perform better if compared with the solution of dam break flow.

- The widely used dam break solution for green water prediction also works reasonable well, if the initial water depth h_0 is carefully selected. However, it fails to predict the shape of the velocity distribution of green water but gives a reasonable prediction on the maximum velocity of the flow. The Ritter's solution for dam break flows was written in Eq. (5.3) and repeated here as

$$u = \frac{2}{3} \left(\sqrt{gh_0} + \frac{x}{t} \right)$$

in which u is the horizontal velocity of the dam break flow, g the gravitational acceleration, x and t are the coordinate system and the time (the same as that in the prediction equation above) and h_0 the initial water depth in the dam. This study suggests the following two equations for the determine of h_0 (details are in Eqs. (5.4) and (5.7))

$$h_0 = H - z_{deck} \quad \text{and} \quad h_0 = \frac{(0.6C)^2}{g}$$

in which H is the breaking water height in deep water (before hitting the structure) and z_{deck} is height of the free board above the still water surface. This study also suggests that $h_0 = (0.6C)^2 / g$ may give a better prediction if the dam break flow is to be used for green water prediction.

- Relatively large aeration in the green water on the deck occurred in the frontal region and higher location. Void fraction showed nearly linear vertical distribution at cross-sections around the leading deck edge. As the green water moved downstream, strong aeration was observed in larger regions except a near-deck region. The distribution is like the typical boundary-layer velocity profile.
- The flow rate at a cross-section estimated from the velocity and void fraction increased gradually from when the water front reached. After reaching the maximum, it gradually decreased. The estimation of overtopping water volume shows mass conservation.

7.2 Recommendations for future study

The present study has tested a plunging breaker as an extreme wave to investigate flow fields of extreme waves and associated overtopping waves in the vicinity of a structure in a 2D wave tank. For future works for this topic, a various kinds of waves are to be tested. It is known that impact pressures on a structure are related with breaking shape of breaking waves. It can be extracted from the point that there would be a relation between the kind of breaking waves and subsequent overtopping water. Thus, more tests with various extreme waves would clarify how overtopping water changes depending on an incoming wave. Moreover, it is necessary to figure out difference in overtopping water generated by between a breaking wave and a non-breaking wave because overtopping water is from both kinds. The present study showed that the green water is highly aerated especially as it moves downstream. Even if a plunging breaker is shown to generate a huge incoming wave and an associated tremendous runup and green water, force exerted on the deck by the green water will be reduced by the aeration. Investigations with non breaking steep waves with large wave height will be needed in progress to figure out causes for most hazardous damage on a structure. The tests in the present study were performed in a 2D wave tank although the model structure was scaled from the 3D proto type. Thus, the study is recommended to be compared with a test with a three dimensional model in a 3D wave tank to see a 3D effect.

REFERENCES

- Buchner, B. (1995a). "The impact of green water on FPSO design." *Offshore Technology Conference, OTC*, Houston, 7698, 45–57.
- Buchner, B. (1995b). "On the impact of green water loading on ship and offshore unit design." *The 6th International Symposium on Practical Design of Ships and Mobile Units (PRADS '95)*, 1430-1443.
- Buchner, B. (1996). "The influence of the bow shape of FPSOs on drift forces and Green Water." *Offshore Technology Conference, OTC*, Houston, 8073, 389-400.
- Chang, K. -A., and Liu, P. L. -F. (1998). "Velocity, acceleration and vorticity under a breaking wave." *Physics of Fluids*, 10, 327-329.
- Chang, K. -A., and Liu, P. L. -F. (1999). "Experimental investigation of turbulence generated by breaking waves in water of intermediate depth." *Physics of Fluids*, 11, 3390-3400.
- Chang, K. -A., and Liu, P. L. -F. (2000). "Pseudo turbulence in PIV breaking-wave measurements." *Experiments in Fluids*, 29, 331-338.
- Chang, K. -A., Lim, H.-J., and Su, C. B. (2003). "Fiber optic reflectometer for velocity and fraction ratio measurements in multiphase flows." *Review of Scientific Instruments*, 74, 3559-3565.

- Chanson, H., Aoki, S., and Maruyama, M. (2002). "Unsteady air bubble entrainment and detrainment at a plunging breaker: Dominant time scale and similarity of water level variation." *Coastal Engineering*, 46, 139-157.
- Christensen, E. D., and Deigaard, R. (2001). "Large eddy simulation of breaking waves." *Coastal Engineering*, 42, 53-86.
- Cox, D.T. and Shin, S. (2003). "Laboratory measurements of void fraction and turbulence in the bore region of surf zone waves." *Journal of Engineering Mechanics*, 129(10) 1197-1205.
- Deane, G. B. (1997). "Sound generation and air entrainment by breaking waves in the surf zone." *J. Acoust. Soc. Am.*, 102(5), 2671-2689.
- Fekken, G., Veldman, A. E. P., and Buchner, B. (1999). "Simulation of green water loadings using the Navier-Stokes equations." *7th International Conference on Numerical Ship Hydrodynamics*, Nantes, France, 6.3.1-12.
- Govender, K., Mocke, G. P., and Alport, M. J. (2002). "Video-imaged surf zone wave and roller structures and flow fields." *Journal of Geophysical Research*, 107(3072), 9.1-21.
- Greated, C. A., and Emarat, N. (2000). "Optical studies of wave kinematics." *Advances in Coastal and Ocean Engineering*, vol. 6, ed. Liu, P. L. -F., World Scientific, Singapore, 185-223.

- Hassan, Y. A., Schmidl, W. D., and Ortiz-Villafuerte, J. (1998). "Investigation of three-dimensional two-phase flow structure in a bubbly pipe." *Measurement Science and Technology*, 9, 309-326.
- Hamoudi, B., and Varyani, K. S. (1998). "Significant load and green water on deck of offshore units/vessels." *Ocean Engineering*, 25, 715–731.
- Hattori, M., Arami, A., and Yui, T. (1994). "Wave impact pressure on vertical walls under breaking waves of various types." *Coastal Engineering*, 22, 79–114.
- Hull, P., and Müller, G. (2002). "An investigation of breaker heights, shapes and pressures." *Ocean Engineering*, 29, 59-79.
- Jansen, P. C. M. (1986). "Laboratory observations of the kinematics in the aerated region of breaking waves." *Coastal Engineering*, 9, 453–477.
- Lamarre, E., and Melville, W. K. (1992). "Instrumentation for the measurement of void-fraction in breaking waves: Laboratory and field results." *IEEE Journal of Oceanic Engineering*, 17, 204–215.
- Lauber, G., and Hager, W. H. (1997). "Experiments to dambreak wave: Horizontal channel." *Journal of Hydraulic Research*, 36, 291-307.
- Lin, C., Hsieh, S. –C., Lin, W. –J., and Chang, K. –A. (2006). "Measurement of velocity field in the aerated region of a hydraulic jump using bubble image velocimetry." *The 17th International Symposium on Transport Phenomena*, Toyama, Japan, in press.

- Lin, P., and Liu, P. -F. (1998a). "A numerical study of breaking waves in the surf zone." *Journal of Fluid Mechanics*, 359, 239-264.
- Lin, P., and Liu, P. -F. (1998b). "Turbulence transport, vorticity dynamics, and solute mixing under plunging breaking waves in surf zone." *Journal of Geophysical Research*, 103, 15677-15694.
- Lindken, R., and Merzkirch, W. (2001). "A novel PIV technique for measurements in multi-phase flows and its application to two-phase bubbly flows." *4th International Symposium on Particle Image Velocimetry*, paper A231.1-12.
- Maruo, H., and Song, W. (1994). "Nonlinear analysis of bow wave breaking and deck wetness of a high speedship by the parabolic approximation." *Proceedings of the 20th Symposium on Naval Hydrodynamics*, National Academy Press, Washington, DC, 59-73.
- Melville, W. K., Veron, F., and White, C. J. (2002). "The velocity field under breaking waves: coherent structures and turbulence." *Journal of Fluid Mechanics*, 454, 203-233.
- Nielsen, K. B., and Mayer, S. (2004). "Numerical prediction of green water incidents." *Ocean Engineering*, 31, 363-399.
- Nishino, K., Kato, H., and Torii, K. (2000). "Stereo imaging for simultaneous measurement of size and velocity of particles in dispersed two-phase flow." *Measurement Science and Technology*, 11, 633-645.

- Oumeraci, H., Klammer, P., and Partenscky, H. W. (1993). "Classification of breaking wave loads on vertical structures." *Journal of Waterway, Port, Coastal and Ocean Engineering*, 119(4), 381–397.
- Oumeraci, H., Bruce, T., Klammer, P., and Easson, W. J. (1995). "PIV-measurements of breaking wave kinematics and impact loading of caisson breakwaters." *Proc. 4th Int. Conf. Port Engng Dev. Countries*, 3, 2394–2410.
- Perlin, M., He, J., and Bernal, L. P. (1996). "An experimental study of deep water plunging breakers." *Physics of Fluids*, 8, 2365-2374.
- Raffel, M., Willert, C., and Kompenbans, J. (2001). *Particle Image Velocimetry; A Practical Guide*, Springer-Verlag, Göttingen, Germany.
- Ray, S. D. (2002). *Applied Photographic Optics*, Focal Press, Oxford, U.K, 215-233.
- Ryu, Y., Chang, K. –A., and Lim, H. –J. (2005). "Use of bubble image velocimetry for measurement of plunging wave impinging on structure and associated greenwater." *Measurement Science and Technology*, 16, 1945-1953.
- Schoenberg, T., and Rainey, R. C. T. (2002). "A hydrodynamic model of green water incidents." *Applied Ocean Research*, 24, 299–307.
- Skyner, D. J., Gray, C., and Greated, C. A. (1990). "A comparison of the time-stepping numerical predictions with whole-field flow measurement in breaking waves." *Water Wave Kinematics*, ed. Torum, A. and Gudmestad, O. T., Kluwer Academic

Publishers, Boston, 491-508.

Ting, F. C. K., and Kirby, J. T. (1994). "Observation of undertow and turbulence in a laboratory surf zone." *Coastal Engineering*, 24, 51– 80.

Ting, F. C. K. and Kirby, J. T. (1995). "Dynamics of surf-zone turbulence in a strong plunging breaker." *Coastal Engineering*, 24, 177– 204.

Vagle, S., and Farmer, D. M. (1998). "A comparison of four methods for bubble size and void fraction measurements." *IEEE Journal of Oceanic Engineering*, 23(3), 211–222.

Vischer, D. L. and Hager, W. H. (1998). *Dam Hydraulics*, John Wiley and Sons, New York.

Wang, D. W., Mitchell, D. A., Teague, W. J., Jarosz, E., and Hulbert, M. S. (2005). "Extreme waves under Hurricane Ivan." *Science*, 309, 896.

Watanabe, Y., and Saeki, H. (1999). "Three-dimensional large eddy simulation of breaking waves." *Coastal Engineering Journal*, 41, 281-301.

Yilmaz, O., Incecik, A., and Han, J. C. (2003). "Simulation of green water flow on deck using non-linear dam breaking theory." *Ocean Engineering*, 30, 601-610.

Zhang, S. G., Yue, D. K. P., and Tanizawa, K. (1996). "Simulation of plunging wave impact on a vertical wall." *Journal of Fluid Mechanics*, 327, 221-254.

Zoppou, C. and Roberts, S. (2003). "Explicit schemes for dam-break simulations."

Journal of Hydraulic Engineering, 129, 11-34.

VITA

Yong Uk Ryu was born in 1974 in Gwang-ju, South Korea. He entered the Department of Civil Engineering at Chonnam National University, Gwang-ju, Korea in 1992. After finishing his military service in the Korean Army for two and a half years, he graduated in February 1999 with the degree of B.S. in civil engineering. He enrolled in the Department of Civil Engineering at Texas A&M University in August 2000 as a graduate student. He received his Master of Science degree from Texas A&M in August 2002 and continued his Ph.D study at the same school, receiving his degree in August 2006.

Permanent address: 207-304 Kumho Apt., Bong-Sun Dong, Nam Gu,
Gwang-Ju 503-062
South Korea.

Email address: ryu00600@hotmail.com